THE UNIVERSITY *of* EDINBURGH

Developments in Reaction Monitoring by NMR

by

Ariana Jones

A thesis presented for the degree of

Doctor of Philosophy

Department of Chemistry

University of Edinburgh

Scotland

28th February 2019

Declaration

I declare that this thesis has been composed solely by myself, carried out with the regulations of the University of Edinburgh. This work is original, except where indicated by reference in the text, and no part has been submitted for any other academic award.

Signed:

Date:

Chapter 4 contains information published in the article:

A. B. Jones, G. C. Lloyd-Jones, D. Uhrin, *Anal. Chem.*, 2017, **89**, 10013-10021

Abstract

NMR is a highly informative non-destructive technique which is why it is so commonly used. However, for the purposes of reaction kinetics there are limitations of the rate at which data can be obtained. There are two main limitations to obtaining NMR kinetic data: the time taken to prepare the sample and begin obtaining data, and the speed at which successive scans can be performed. As each of the two problems are very different there are two themes to this project. The preparation time has been improved using hardware, specifically stopped flow equipment (*InsightXpress*) that has been developed. This novel stopped flow NMR system allows 95% pre-magnetisation via coils held at close proximity to the bore of the magnet, which can be rapidly injected at speeds up to 2ml/s, for three separate solutions.

Whilst the rate at which successive scans can be obtain is improved via NMR pulse programming, with schemes such as frequency-shifted spatially-selective NMR.[1] Another factor limiting the rate at which NMR data can be obtained is sensitivity, this can be significantly improved by pure-shift techniques. A pure-shift method referred to as SHARPER has been developed for reaction monitoring - increasing sensitivity whilst minimising the loss of absolute integration.

Another break-through in NMR spectroscopy is parallel-receiver technology, allowing up to twice the amount of data per time, this has also been developed and employed whilst studying reactions.

Lay Summary

When monitoring fast chemical reactions by NMR (Nuclear Magnetic Resonance) two things need to be considered: how fast reactant solutions can be mixed, and how rapid we can preform repeat measurements. To allow effective rapid mixing we have developed a special apparatus for reaction monitoring by NMR. This consists of a mixing cell that can mix chemicals from three separate reservoirs and sits inside of the magnet of an NMR spectrometer. The reservoir positions mean that we can start reaction monitoring without a long delay, this is usually needed to build up an NMR signal for samples mixed outside of the magnet. The second advantage of this apparatus is that once mixed, the reaction mixture had a very short path to reach the measuring coils. This apparatus has been tested on a variety of reactions to optimise its performance with regard to speed and reliability. With this novel method at hand, reactions with half-lives of 2.2 seconds have been monitored, not previously possible with standard NMR hardware.

NMR is not a very sensitive technique, and sometimes multiple scans are needed to increase the signal intensity; this takes time and is not compatible with studying fast reactions. One way to overcome the need to repeat scans is to remove some of the chemical information contained in NMR signals that are split into multiple lines, decreasing the sensitivity of the measurements. We have developed a new method called SHARPER that yields a single narrow tall and sharp line increasing the sensitivity of NMR measurements multiple times. Another method for speeding up NMR acquisitions is based on not exciting the whole sample but limiting this to a narrow horizontal slice. This means that the consecutive time points of a reaction can be monitored in different slices without the need to wait for NMR signal to build up. Removing the need to wait between scans speeds up the acquisition con-

siderably. This approach can be combined with the SHARPER method producing a vital boost in sensitivity boost to this method, which inevitably is very insensitive as it utilises only a fraction of the sample to measure the signal at each time point.

The final development in this project was a modification of techniques that allow simultaneous acquisition of signals from two nuclei. This so called "multiple receiver techniques" were modified to enable the SHARPER approach to be implemented.

Acknowledgements

Firstly I would like to thank myself, well done for finishing your PhD., Aqua - Doctor Jones, can forever be your ring tone now. Mum and Dad thanks for giving me love, support and making me confident enough that I believe I can do anything I want, you two are my favourite people, always.

More professionally I would like to thank both Prof. Dusan Uhrin and Prof. Guy Lloyd-Jones FRS for the opportunity to take on this project and their continuing support throughout. As well as Bruker for sponsoring and supporting me throughout. A big thanks to Ted King, Ruth Dooley and Anna Codina for their help developing the stopped flow NMR kit. Pete Gierth, the NMR genius, has been unbelievably helpful throughout my PhD, I hope to one day know half as much as you do. Matteo Pennestri, who continuously spells my name wrong, but always makes the best food while I'm at Bruker.

A big thanks to all past and present members of both the BioNMR and Lloyd-Jones research groups. Apologies for all the times I've undoubtedly came into the office and distracted you all from working because I wanted a chat, and thank you for all the good times.

An infinitely huge thank you to Lorna, who has been there for me every day of my PhD. You're everything a girl needs in a best friend, and I love you always. I'm not sure I would have managed the last few years without you.

Another special shout out to Matt, Will, Alan for their continuing support in my apparent attempt to damage my liver during my time in Edinburgh. You guys never fail to make me laugh, and I have the most amazing memories with all of you.

Abbreviations and Acronyms

ASAP	Acceleration by Sharing Adjacent Polarization
BIRD	Bilinear rotation decoupling
BS	Band-selective
COSY	Correlation spectroscopy
CPMG	Carr-Purcell-Meiboom-Gill
CSA	Chemical shift anisotropy
d_1	Relaxation delay
EXACT	EXtended ACquisition Time
exp	Exponential
FB	Fluorobenzene
HSQC	Heteronuclear Single Quantum Coherence
Hz	Hertz
KOH	Potassium hydroxide
MeOH	Methanol
NMR	Nuclear magnetic reasonance
NUS	Non-uniform Sampling
PANSY	Parallel Acquisition NMR Spectroscopy
PFG	Pulsed field gradient
ppm	Parts per million
PS	Pure shift
RF	Radio frequency
RQF	Rapid Quench Flow
rt	Room temperature
S/N	Signal-to-noise
SF	Stopped flow
SFIR	Stopped slow Infra-Red
SFNMR	Stopped flow Nuclear Magnetic Reasonance
SOFAST	band-Selective Optimized Flip-Angle Short-Transient
SPFGSE	Single Pulse Field Gradient Spin Echo
SPOFFS	Shaped Pulse Offset
TFA	Trifluoroacetic acid
TFE	Trifluoroethanol
TFT	Trifluorotoluene
THF	Tetrahydrofuran

T_1	Spin-lattice relaxation
T_2	Spin-spin relaxation
δ	Chemical shift
°C	Degrees Celsius
ZS	Zangger-Sterk

Contents

Chapter 1

Introduction

1.1 Reaction monitoring

Reaction monitoring is an integral part of chemical research. But why? As chemicals become more scarce it is beneficial to find the most efficient way to synthesis useful compounds and materials. Reaction monitoring allows insight into the mechanism of forming such products, and therefore allows better control, process development and industrial scale monitoring. Ideally the scientific technique employed to monitor reactions should allow the user to acquire information on all the species present, be under real reaction conditions, have high sensitivity and temporal resolution.[3]

1.1.1 Considerations

When monitoring reactions, the analytical technique used needs to be appropriate for both the species being studied and the time scale of the reaction. The dead time of the method also needs to be as short as possible, especially for fast reactions. Improving the dead-time and methods for improving the data acquisition are a theme throughout this thesis.

1.1.2 Protodeboronation of Boronic Acids

Boronic acids have been extensively used in organic chemistry.[4] Notably, they have been used in transition-metal-catalysed cross-coupling reactions,[5–7] most famously perhaps in the

Suzuki-Miyaura cross-coupling (SMC) reaction.[8]

Protodeboronation is a well-known undesirable side reaction of the SMC reaction. SMC is an efficient method to create a new carbon-carbon bond. It is performed by reacting an organoboron species with a halide species in the presence of a palladium catalyst, usually under basic conditions. The basic conditions aid in the break down of the aryl boronic acid to boric acid and the associated phenyl species.

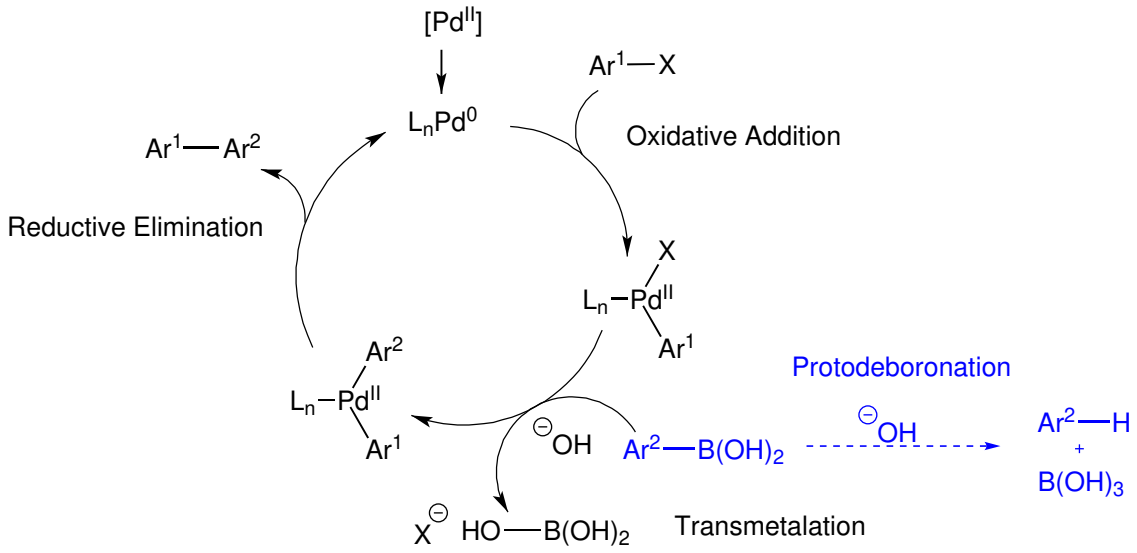

Figure 1.1: General scheme of the SMC reaction, with the protodeboronation pathway highlighted in blue.

The most commonly used organoboron species are boronic acids, they are often commercially available, inexpensive, readily prepared, and are highly reactive towards transmetalation.[9] The downside to aryl boronic acids is that they are highly susceptible to undergo protodeboronation.[9,10] Boronic acids have a vacant p-orbital, due to this they have a high affinity to water, and have an equilibrium between boronic acid and boronate, shown in Figure 1.2.

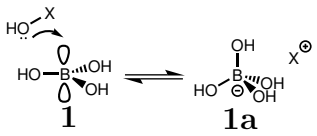

Figure 1.2: Boronic acid/boronate equilibrium

Due to the practical implications of the undesirable protodeboronation reaction, decreasing the yield and purification issues, it has been extensively studied under SMC experimental conditions. It has been found that the rate of protodeboronation of aryl boronic acids is greatly dependent on the substitution of the phenyl ring.[11,12]

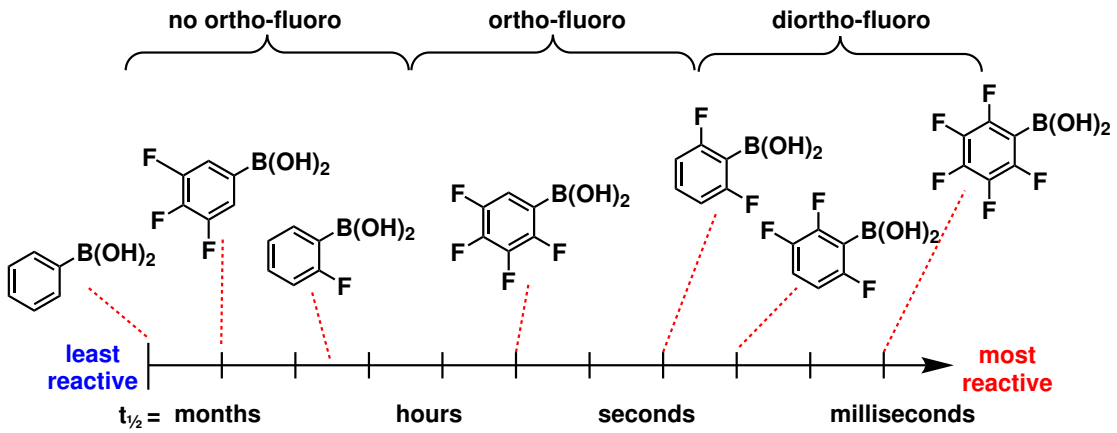

Figure 1.3: Scale showing protodeboronation rates of fluoro-substituted aryl boronic acids

This rate dependency of protodeboronation of fluorinated aryl boronic acids greatly depends on the position of the fluorine atom(s). As can be seen in Figure 1.3, ortho-fluorination greatly increased rate of protodeboronation. This tunable rate of protodeboronation presented a series of reactions, allowing different time scales to be studied, each bringing different challenges. In addition, the large chemical shift dispersion and sensitivity of ^{19}F make monitoring this reaction by NMR very convenient.

Another unwanted side reaction in the SMC cross coupling reaction is the oxidation of organoboron species. When oxygen is incorporated into the catalytic cycle, shown in Figure 1.4, a cross coupling product and a phenol derivative are formed.[13]

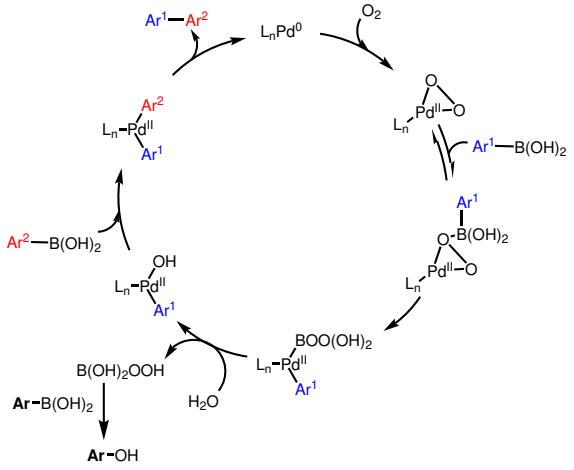

Figure 1.4: Suzuki-Miyaura oxidation reaction cycle

Boronic acids can also be oxidised without the presence of palladium, if peroxides are formed.[14] Solvents commonly used in SMC such as THF and dioxane, can readily form peroxides in the presence of oxygen and light.

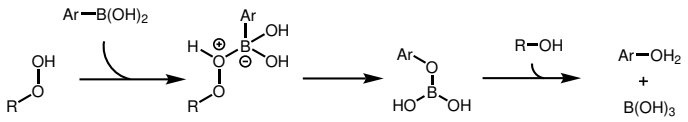

Figure 1.5: Boronic acid oxidisation in the presence of a peroxide

For oxidation of boronic acids, the reaction needs to either have oxygen present, or have an unstablised solvent which has peroxides present. The mechanism formation of peroxides in organic solvents is thought to be due to trace metals present, and therefore varies between solvent batches.

1.1.3 Phosphine oxidation

Oxidation of phosphines readily occurs, sometimes accidentally, to organophosphines. Phosphorous has a high affinity for oxygen, and is readily oxidised under atmospheric conditions. The driving force for this reaction is the empty p-orbitals, much like with boronic acids. Oxidation of diphenylphosphine (DPP), shown in Figure 1.6, was studied with pulse program SHARPER, described in Chapter 4.

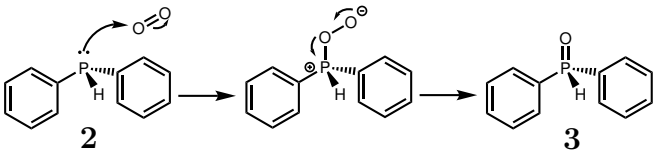

Figure 1.6: Scheme of oxidation of Diphenylphosphine

1.2 NMR

Nuclear magnetic resonance (NMR) is a spectroscopic technique which observes the behaviour of nuclei in a magnetic field. Like all spectroscopic techniques the information arises from absorption (and emission) of electromagnetic radiation, specifically radio-frequency. It provides information about the environment of all NMR active nuclei.

NMR was first observed in 1945/6 by two independent groups; Purcell in Harvard (^{1}H in parafin at 30MHz)[15] and Bloch in Stanford (^{1}H in water at 8MHz).[16,17] Both Purcell and Bloch shared the Nobel Prize for physics in 1952 due to their discoveries. NMR has come

a long way since then, with new techniques and improved data manipulation making it a common tool for every chemist.

1.2.1 Basic theory

Nuclei possess an internal property called spin, defined by a quantum number denoted I, where $I = n/2$ and n is an integer. Nuclei are made up of protons and neutrons, the ratio of these dictate the quantum number, *I*. Nuclei with $I = 0$, which have no nuclear spin, are known as "NMR silent". Every nuclei with $I \geqslant 1/2$ have multiple spin states denoted by a quantum number m_l ranging between I to $-I$, in integer steps. Nuclei have a magnetic moment μ which is proportional to the spin angular momentum, **I**

$$\mu = \frac{\gamma h \mathbf{I}}{2\pi} = \gamma \hbar \mathbf{I} \tag{1.1}$$

Where γ is the gyromagnetic ratio, specific to a given nucleus, and h is Planck's constant. These quantum states are normally degenerate, however when placed in a magnetic field the energy levels split. From an organic chemistry point of view, the most important nuclei are those with spin quantum number $\frac{1}{2}$ (^{1}H, ^{13}C, ^{19}F, ^{15}N, ^{31}P) and will be used as an example throughout.

The splitting of the energy levels leads to a Boltzmann distribution (Eqn. 1.3) of energy states with different populations, dependent on both the nucleus (γ) and magnetic field strength (B_0), Equation 1.2.

$$\Delta E = \frac{h \gamma B_0}{2\pi} \tag{1.2}$$

Where E is the energy and B_0 is the magnetic field strength. For example, in a 400MHz spectrometer (magnetic field strength of 9.4 T), the energy gap at 300K for proton is 2.65 x 10^{-25}J. The ratio of transitions are explained by the Boltzmann distribution as can be seen in Equation 1.3.

$$\frac{N_\alpha}{N_\beta} = exp\left(\frac{-\Delta E}{k_B T}\right) \tag{1.3}$$

Where N is the population of nuclei (α is -$\frac{1}{2}$ and β is +$\frac{1}{2}$), ΔE is the energy difference between the spin states, k_B is the Boltzmann constant, T is the temperature in K.

The thermal energy k_BT is 4.14 x 10^{-21} J, is much larger than the energy difference. This

leads to approximately only one nucleus in every $10^4 - -10^6$ being detected. The intensity of the NMR signal is dependent on the population difference, which is ultimately dependent on B_0. This lack of sensitivity is one of the biggest challenges in NMR spectroscopy,[18] which is why the desire for stronger magnets (and hence magnetic field strength) is paramount, to increase the energy difference and consequently increase the sensitivity.

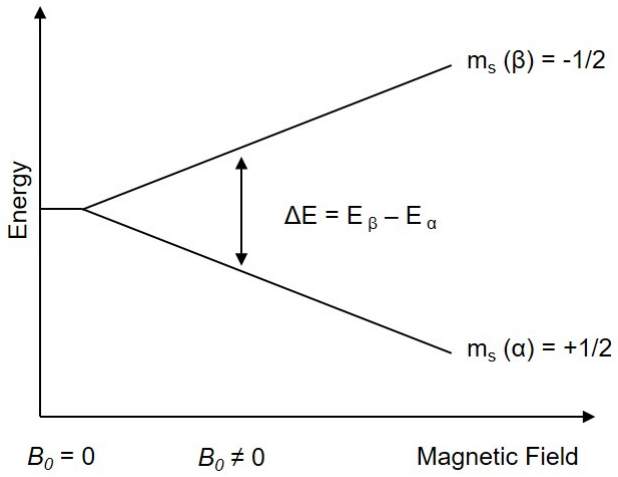

Figure 1.7: Splitting of energy levels in a magnetic field

For an I = $\frac{1}{2}$ nuclei the two spin states are labelled α (for spin up i.e. aligned with the magnetic field) and β (for spin down i.e. opposed to the field). The α spin state will have an excess of spins, due to it being lower in energy. The excess of spins leads to an overall magnetisation denoted, **M**, for magnetisation (Eqn. 1.4).

$$M = \sum_{i=1}^{N} \mu_i \tag{1.4}$$

As can be seen in Figure 1.7 the stronger the magnetic field the greater the split in energy levels, and therefore greater sensitivity.

As with all spinning bodies, the nuclei possess angular momentum, **P**, the motion and charge give rise to an associated magnetic moment, μ:

$$\mu = \gamma \mathbf{P} \tag{1.5}$$

The gyromagnetic ratio is the ratio of the angular momentum relative to its magnetic dipole moment, information for specific nuclei can be seen in Table 1.1.

Table 1.1: Gyromagnetic ratios, NMR frequencies (in a 9.4T field) and natural abundancies[19]

	γ /10^7 rad T^{-1} s^{-1}	ν_{NMR} /MHz	Natural abundance /%
^{1}H	26.752	400.0	99.9885
^{2}H	4.107	61.4	0.0115
^{11}B	8.583	128.4	80.1
^{19}F	25.181	376.5	100.0
^{31}P	10.839	162.1	100

Nuclei precess around at their Larmor frequency within the magnetic field, Equation 1.6:

$$\nu_0 = \frac{|\gamma|}{2\pi}|B_0| \tag{1.6}$$

If a radiofrequency (RF) field, $\mathbf{B_1}$, perpendicular to $\mathbf{B_0}$ at a frequency close to the Larmor frequency, is used to tip the magnetisation away from the z-axis:

$$\frac{d\mathbf{M}}{dt} = \gamma(\mathbf{B_0} + \mathbf{B_1})\mathbf{M} \tag{1.7}$$

The nuclei will then precess around the xy-axis at the Larmor frequency. The oscillation of the magnetisation induces a current, which is then amplified and measured producing free induction decay (FID). This induced current decays with time as the system returns to equilibrium (relaxation). The difference between the frequency of the NMR signal and excitation frequency is measured, giving *relative frequencies*. As spectra are calibrated to a known standard taking relative frequencies instead of absolute frequencies is not problematic. For optimum alignment of the nuclei to the magnetic field we need a very homogeneous magnetic field, how this is achieved will be explained in Section 1.2.7.

Chemical shift and coupling constants

The magnetic field felt by different nuclei in a molecule varies causing nuclei to precess at its own frequency. This is due to electrons surrounding the nuclei, changing the magnetic field felt by them, and therefore the frequency they precess at. The magnetic field felt is

defined by $B = B_0(1 - \sigma)$, where σ is known as the shielding constant. This is the origin of the chemical shift (δ), which is typically expressed relative to a frequency of a standard.[19]

$$\delta = 10^6 \frac{\nu - \nu_{ref}}{\nu_{ref}} \tag{1.8}$$

The frequency difference, $\nu - \nu_{ref}$, is divided by the reference frequency to remove magnetic field dependence of the value. The 10^6 allows the values to be given in *parts per million*, ppm.

Interactions between spins are called spin-spin couplings, and consist of two categories: direct and indirect dipole-dipole couplings. Direct coupling is generated through space of nuclear magnetic fields, dependent on their relative orientations and therefore averages to zero in isotropic liquids. Indirect spin-spin coupling (scalar or J-coupling) is the result of interactions with electrons. The signals of each spin will then be split according to the possible energy eigenstates of each neighbouring spin (2nI + 1), i.e. the signal belonging to a spin-1/2 nucleus will, in the simplest case, be split into two signals, when coupled to another spin-1/2 nucleus. The magnitude of the separation is the coupling constant, J, which is independent of the magnetic field strength. This splitting pattern provides useful information on the arrangement of chemical bonds within a molecule.

1.2.2 Relaxation

Relaxation Pathways

Relaxation is the term used to describe the magnetisation returning to 99% of the equilibrium; the process can take anything between a few seconds up to minutes, in liquids.[20,21] Relaxation is a lot slower in NMR compared to other spectroscopic techniques, which allows further manipulation of the nuclear spins to obtain information about the studied system. Different nuclei and local environments will lead to different time scales for relaxation.

There are two relaxation processes; spin-lattice (T_1) and spin-spin (T_2) relaxation. T_1 relaxation is associated with the relaxation back to the z axis, whilst T_2 relaxation is associated with the decay of the xy magnetisation due to loss of coherence.

The equilibrium itself arises due to the energy levels in the spin system no longer being degenerate in a magnetic field. As described in Section 1.2.1, the split in energy levels leads to a preferential (lower energy) state, where the spins align with the magnetic field according to a Boltzmann distribution.

After the application of a RF pulse, the population ratios are altered, giving transverse magnetisation $\mathbf{M}_{xy}$. This spin-lattice magnetisation decays exponentially until the Boltzmann equilibrium is restored, as shown in equation 1.10.

$$M_z(t) = M_{z,eq}\left[1 - exp\left(\frac{-t}{T_1}\right)\right] \tag{1.9}$$

Where $M_{z,eq}$ is the equilibrium population difference, T_1 is the inherent spin-lattice relaxation time and t is time.[22]

T_1 quantifies the rate of transfer of energy from the spin system to neighbouring molecules (hence the name spin-lattice). Prior to pulsing the sample again it needs to be allowed to relax back to equilibrium. The exponential factor means that for 99% relaxation we need to wait $5T_1$. This is usually not a problem as T_1 is commonly a few seconds for spin-half liquid samples, however for rapid repetition of scans it becomes a hindrance. Relaxation can be thought of as equilibrium for a reversible reaction, therefore to reach equilibrium the rate of $\beta \rightarrow \alpha$ must exceed the rate of $\alpha \rightarrow \beta$ by a factor of exp $(\hbar\omega_0/k_BT)$.[23] Transitions back to equilibrium are enabled by local magnetic fields which are oscillating close to the Larmor frequency.

The RF pulse which flips the z magnetisation into the xy plane also generates a coherence between the spins where all spins start precessing in the xy plane with the same phase. The spin-spin relaxation, characterised by the spin-spin relaxation time T_2, removes this coherence described by:

$$M_z(t) = M_{z,eq}exp\left(\frac{-t}{T_2}\right) \tag{1.10}$$

The consequence of this exponential decay is the Lorentzian line shape of NMR signals

produced by Fourier transformation. The Lorentzian line can be described as:

$$s\left(\Omega\right) = \frac{1}{T_2\left(\left(\frac{1}{T_2}\right)^2 + (\Omega - \Omega_c)^2\right)} - i\frac{\Omega - \Omega_c}{\left(\frac{1}{T_2}\right)^2 + (\Omega - \Omega_c)^2} \tag{1.11}$$

Where Ω is linewidth, and Ω_c is the corrected linewidth. NMR line shapes are typically broader; there are many reasons for this broadening, most common is magnetic field inhomogeneity. As can be seen in Equation 1.11, the shape is dependent on T_2, in the presence of magnetic field inhomogeneity this becomes T_2^*. Another factor that affects line shape is chemical exchange, discussed in Section 1.2.3.

Relaxation Mechanisms

The mechanism of relaxation is dependent on magnetic interactions, the most prevalent being dipolar coupling.[19] The local fields can interact with one another; they are time dependent due to molecular motions within the sample. The dipolar coupling and movement of the nuclei then leads to the spins acting as an oscillating magnetic field which induce transitions of the spins (much like a RF pulse). The T_1 relaxation works by providing a mechanism for the energy to dissipate to the surroundings (the "lattice"). This interaction can occur via nuclei in the same molecule (intra-) or different molecules (inter-). Due to the inherent closeness, intra-molecular relaxation is the principal mechanism. Molecular motion plays a role in dipole-dipole relaxation, whereby molecular size plays a role, described in Figure 1.8. The molecular motion can be quantified by the correlation time (τ_c), which is an estimate of the time taken for a molecule to rotate through one radian.

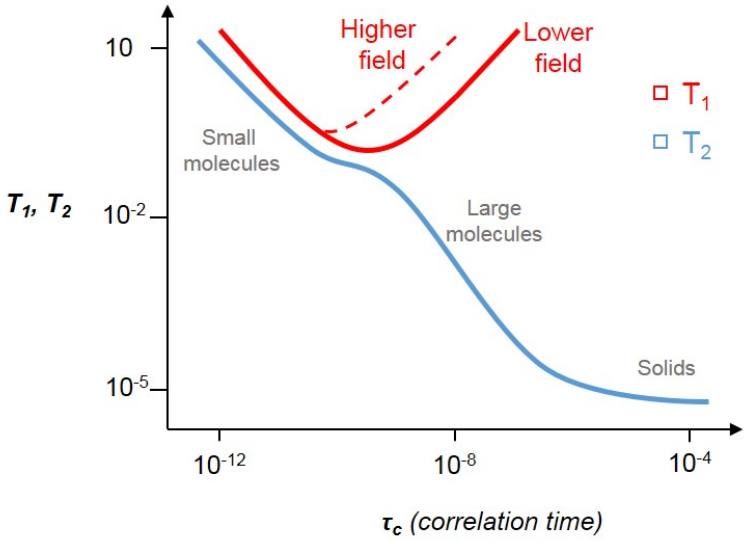

Figure 1.8: Graph depicting molecular size effects on T_1 and T_2 relaxation[19]

Another relaxation mechanism is the chemical shift anisotropy (CSA). Nuclei in different environments (i.e. surrounded by different electron densities) have varying chemical shifts, as they experience a different magnetic field. These variations in fields can also cause relaxation, in a similar way to dipole-dipole interactions. CSA has a greater effect on nuclei with large chemical shift ranges, and in higher fields for obvious reasons, i.e. CSA is more prevalent in ^{19}F than ^{1}H due to the larger chemical shift ranges.

Quadrupolar relaxation can only occur in nuclei with $I > \frac{1}{2}$, and is often predominant in these species. Nuclei with $I > \frac{1}{2}$ possess a quadrupolar moment, as well as a magnetic dipole moment, due to the charge distribution within the nucleus. These quadrupolar nuclei can interact with asymmetrical electric field gradients. The mechanism of quadrupolar relaxation itself is similar to dipole-dipole relaxation. Quadrupolar nuclei, such as ^{11}B, relax very quickly and therefore often have very broad line shapes (Eqn. 1.11).

1.2.3 Chemical Exchange

NMR spectroscopy allows us to see the environment that nuclei are in, and sometimes these species are in equilibrium. The rate of this exchange dictates the lineshape within the spectrum, shown in Figure 1.9. If two species are in equilibrium, they can be described by

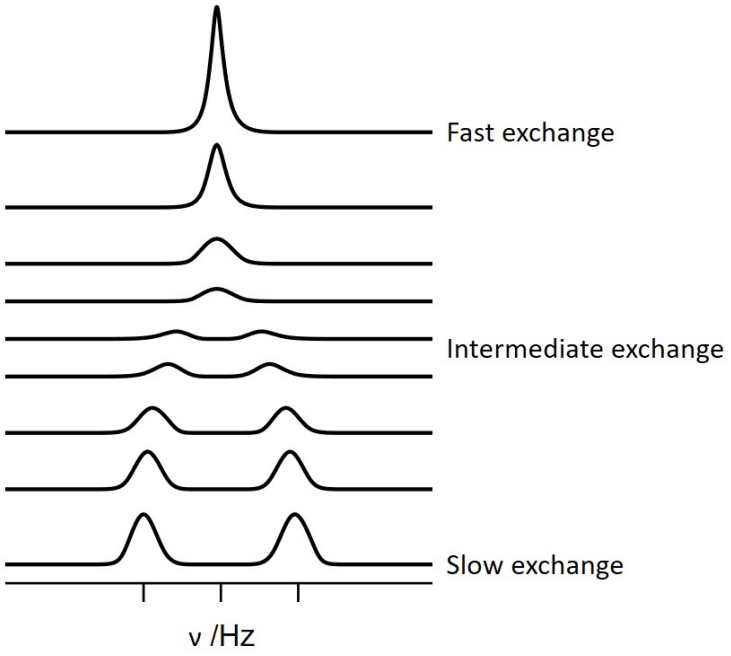

Figure 1.9: An example of chemical exchange between two conformations of the same nucleus, showing different rate of exchanges on the NMR timescale

the following:

$$\mathrm{A} \underset{\mathrm{k_b}}{\overset{\mathrm{k_a}}{\rightleftharpoons}} \mathrm{B} \tag{1.12}$$

If there is an equilibrium between A and B, the nuclei concerned will experience two different chemical environments. As the chemical shift is dependent on chemical environment, the effect on the peak positions will be dependent upon rates, k_A and k_B, and the difference

between the chemical shifts ($\Delta\nu$).

If the rate is slow on the NMR time-scale, where k_A and $k_B << \Delta\nu$, then two separate signals are observed. This is denoted *slow exchange*, where each peak corresponds to the two species (A and B). The relative intensities are dependent on the concentrations of each species. However, if the interconversion rate increases, to the point where k_A and $k_B \approx \Delta\nu$, then the species are in *intermediate exchange*. This exchange regime results in partial averaging of each of the chemical shifts, leading to broadening of both peaks. Finally, when the interconversion rate is fast on the NMR time-scale, where k_A and $k_B >> \Delta\nu$, the effects of chemical shifts are completely averaged, so only one peak is observed. This single signal will appear between the shifts of A and B, the exact position will be dependent on the populations of each species.

At chemical equilibrium the rate of exchange can be explained by Equation 1.13.

$$k_{ex} = k_a + k_b \tag{1.13}$$

Under these circumstances, the relative site populations, p_A and p_B ($p_A + p_B = 1$) satisfy the balance relationship $p_A k_A = p_B k_B$. If $p_A \gg p_B$ (or $p_B \gg p_A$), the transverse relaxation rate constant R_2 of the population-averaged resonance line is given by Equation 4.3.

$$R_2 = R_2^0 + \frac{p_A p_B \Delta\nu^2}{k_{ex}} \tag{1.14}$$

Where $R_2^0 = p_A R_{2A} + p_B R_{2B}$ and the position of the observed spectral line (Ω) is given by Equation 4.4.

$$\Omega = p_A \Omega_A + p_B \Omega_B \tag{1.15}$$

1.2.4 The vector model

A simple way to visualise what happens to the magnetisation during a pulse sequence is the Bloch sphere method, known as the vector model. It allows visualisation of what happens during the pulses, and the free evolution intervals.

The overall magnetisation, **M**, can be described as a vector quantity as it has both magnitude and direction. The magnetic field of both the instrument and the RF pulse determine what happens to the magnetisation vector **M**. At equilibrium the magnetisation is precessing about the z-axis, at the angular velocity given by -γB. During a RF pulse the spins precess around B_{eff}, which is the sum of both B_0 (the instrument's magnetic field) and B_1 (the magnetic field caused by the RF pulse). The laboratory frame becomes complicated here, due to the fact that B_{eff} is actually precessing around the z-axis. To simplify the vector model, we can imagine ourselves rotating about the z-axis at the same rate as B_1, this is called the rotating frame. The rotating frame concept is very useful as spectrometers detect the offset frequencies (i.e. the difference between the frequencies from a specified frequency as described in Section 1.2.1). At equilibrium the magnetisation can be thought of as stationary in the z direction in the rotating frame. The application of a RF pulse along the x-axis then causes the magnetisation to precess around the x axis, moving the magnetisation towards the y-axis, Figure 1.10.

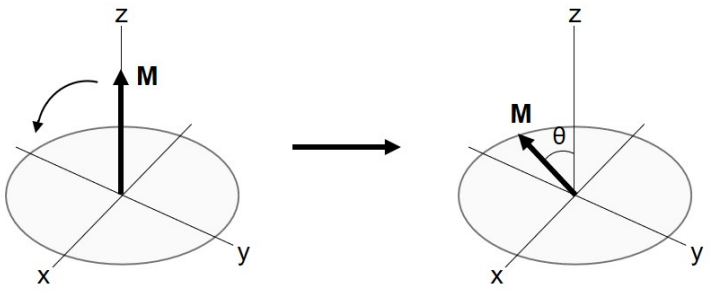

Figure 1.10: Magnetisation during a RF pulse

The RF pulse has a much stronger effective magnetic field than the external magnetic field due to it being *resonant* with the Larmor frequency. Hence, neglecting the off resonance effects, the B_{eff} is aligned with B_1.[21] The magnetisation is pushed into the xy-plane, precessing around the effective magnetic field. The RF pulse is switched off after the nucleus performed a $\frac{\pi}{2}$ rotation.

After the pulse the nuclei begin precessing around the z-axis (around B_0), Figure 1.11. The rate at which they precess is dependent on the nuclei and the magnetic environment the nuclei are in.

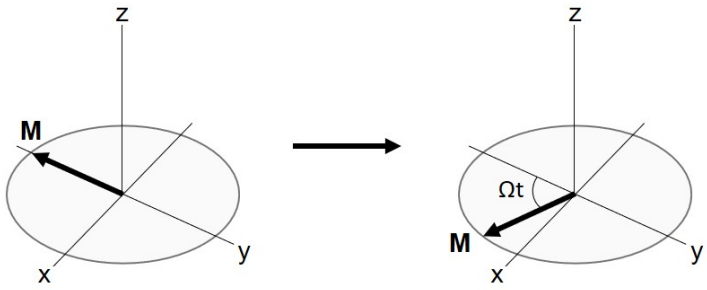

Figure 1.11: Magnetisation precessing about the xy-plane after a RF pulse

Whilst the nuclear spins precess about the z-axis they begin to relax, as discussed in Section 1.2.2. During the relaxation, the receiver coil measures the voltage of the oscillating magnetisation. There are two parts to the spectrum known as real and imaginary, the projection of the magnetisation in the x and y axis, as shown in Figure 1.12. The free induction decay is measured, containing information regarding the different frequencies, amplitude and T_2.

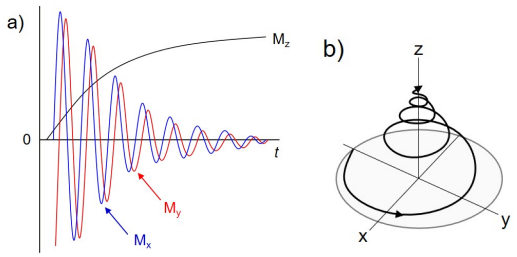

Figure 1.12: a) The real and imaginary frequencies (where $T_1 = T_2$). b) Following the magnetisation after a 90° pulse.[19]

Spin echoes

Spin echoes (Figure 1.13) are commonly used elements in pulse sequences, they are used to refocus the signals.

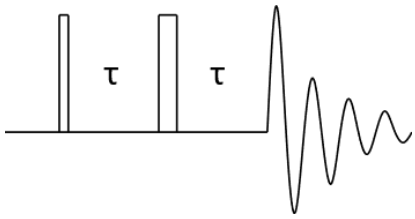

Figure 1.13: Spin echo pulse sequence. Narrow and thick boxes represent a 90° and 180° pulse respectively.

To describe the effect of the spin echo, the vector model can be used (Figure 1.14). The initial 90° pulse brings the magnetisation into the xy-plane, during the time τ the magnetisation precesses, the 180° pulse then flips the magnetisation into the mirror image, then the magnetisation refocuses during the next τ period.

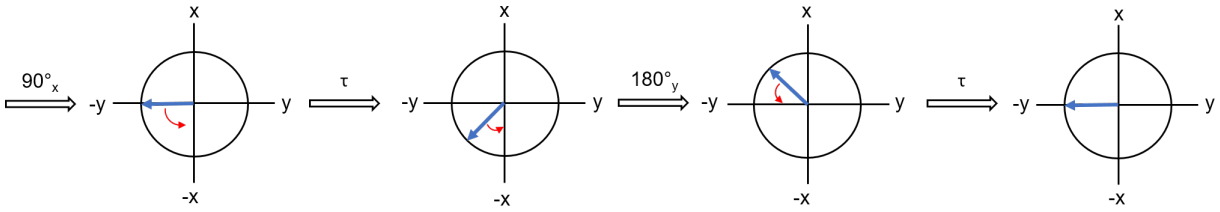

Figure 1.14: Impact of spin echo on the magnetisation (blue), direction of movement shown (red)

1.2.5 Pulsed field gradients (PFG)

To create a PFG a coil is placed near the RF coil in the NMR probe, so a magnetic field gradient can be generated by a flowing current. Pulsed field gradients apply a "linear" gradient along the NMR tube, shifting the magnetic field so it becomes spatially dependent, as shown in Figure 1.15.

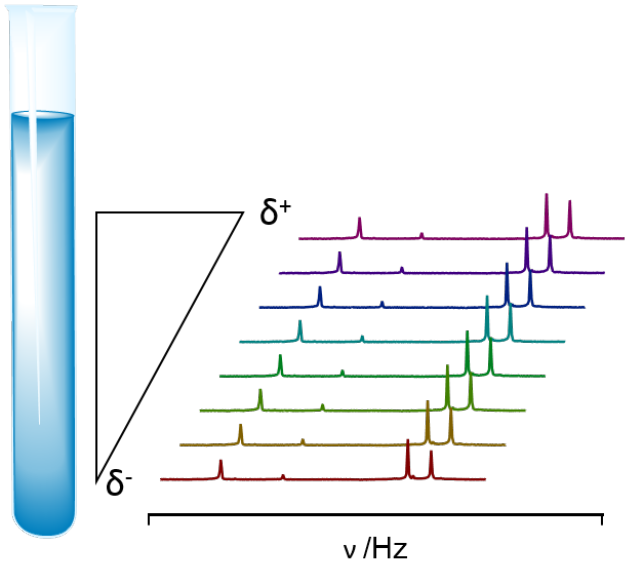

Figure 1.15: Magnetic field effect during PFG, tilting B_0

The gradients are generated by a gradient coil, which are standard in modern spectrometers. During gradients the angular velocity of spins will be:

$$\omega_0 = -\gamma|B_0| - \gamma G_z \tag{1.16}$$

Therefore, after a gradient pulse of amplitude G and duration τ, the phase change of the magnetisation will be given by:

$$\Psi = -p\tau\gamma G_z \tag{1.17}$$

Where p is the coherence order. Gradients dephase coherences in the plane perpendicular to the direction in which the gradient is applied. This dephasing is performed in a reproducible way and can therefore be refocused by applying an opposite gradient.

When gradients are applied, they generate eddy currents, these electrical currents in the conducting parts of the probe and magnet are due to the sudden change in magnetic field. These can be reduced by an outer coil (shield) that generates a field outside the inner coil

opposite to that generated by the latter. It isn't possible to completely cancel out the external field perfectly, so after PFGs, a stabilisation delay needs to be inserted into the pulse sequence to allow the currents to dissipate.[24]

1.2.6 NMR techniques

Fast NMR techniques

NMR spectroscopy is an information rich, non-destructive and non-invasive technique. However, one of the drawbacks of NMR spectroscopy is that it can be very time consuming, not only because of its limited sensitivity[18] but also because of the way NMR spectra are acquired. Many techniques have been developed trying to reduce the time it takes to obtain high quality data rapidly, much of which is focused on 2D (or greater dimensional) NMR, as multidimensional NMR methods are particularly time consuming.[25–27]

Fast NMR is a quite ambiguous term, especially as in different fields it will have a different meaning. For example, ^{19}F NMR of a fluorobenzene trifluoroethanol (FB/TFE) mixture has a T_1 of $\sim$ 3 seconds. This means for a 90° pulse, the time required between scans for relaxation, to recover 99% of magnetisation, is $5T_1$, $\sim$15 seconds. For only 5 scans following the reaction, that is already one minute. One simple method for speeding up scan repetition without rendering the data useless (by repeatedly scanning without a long enough relaxation delay) is via decreasing the pulse length.

In this thesis fast NMR means monitoring kinetics that have a sub-minute half life. As T_1 has an exponential decay (as described in Section 1.2.2). If repeated for example with 30° pulse the spins are already 87% relaxed, requiring less time to completely recover. This allows faster repetition of the pulsing, acquiring more data in a shorter space of time.[28] Reducing the pulse strength does however reduce the signal intensity, decreasing signal-to-noise ratio.

Another technique to avoid waiting for relaxation is by using selective pulses in combination with PFG (pulsed field gradients - Section 1.2.5).[1,29] Applying a weak gradient field to the

sample gives a location-dependent frequency shift described in equation 1.18 below.[30,31]

$$\Delta\omega = \gamma * G * s \tag{1.18}$$

Where s is the distance from the centre of the gradient coil in cm.

Whilst the gradient is on, a selective pulse is employed, which excites the whole spectrum however due to the location-dependent frequency shift the signals are excited in different parts of the sample.[32–34] This technique has been used for broadband decoupling[30,35–37] , diffusion measurements,[38,39] single sample titrations[40] and fast reaction monitoring.[1,41] Due to the recent implementation of this technique for fast reaction kinetics without the need for delays between scans this pulse program has been employed and tested, which will be discussed in Chapter 3.

Many techniques have been developed to speed up nD (where n > 1) NMR. Some of these use data prediction methods[42] from obtained data such as NUS[43] and hadamard encoding.[44,45] Other techniques utilise pulse programs to speed up the nD such as ASAP, EXACT,[26,46,47] SOFAST[48] and ultrafast NMR,[49–51] these are able to deliver multidimensional spectrum in a single transient (scan) via spatial manipulations.[31]

Pure shift NMR

Pure shift (PS) NMR spectroscopy has been increasing in popularity recently, due to the benefits it provides and continuous improvements in the technique. Pure shift (also known as broadband homonuclear decoupling) is named due to the removal of J couplings, leaving a singlet, giving purely the chemical shift information. Although J couplings provide useful information, they impede spectral resolution. This is most beneficial for ^{1}H spectroscopy due to its narrow spectral width and overlapping signals.[52]

The first pure shift methodology, which is still widely used is J-resolved spectroscopy.[53] The pulse program itself works by projecting the J-coupling in the second dimension, whilst giving the chemical shifts in the other. These 2D spectra can then be summed, to give a 1D pure shift spectrum. There have been many developments since this, most of which fall into two acquisition methods, and four refocusing techniques.

There are two main pure shift acquisition methods - interferogram and real-time. Interferogram methods work by acquiring several FIDs and summing them together to get a full PS spectrum. Real-time acquisition methods, interrupt the acquisition, to actively refocus the spins. Each acquisition method has its benefits, interferogram being good S/N and clean spectra without J-modulation. Real-time methods being significantly shorter in acquisition time, collecting the data in "chunks", however these chunks result in J-modulation of the signals, producing chunking artefacts.

There are four main active spin refocusing methods, shown in Figure 1.16: **Bi**linear **R**otation **D**ecoupling (BIRD),[54] **Z**angger-**S**terk (ZS),[55] **B**and-**S**elective (BS),[56,57] "double β" (such as PSYCHE and anti-z-COSY).[58,59] Again each method has its own benefits.

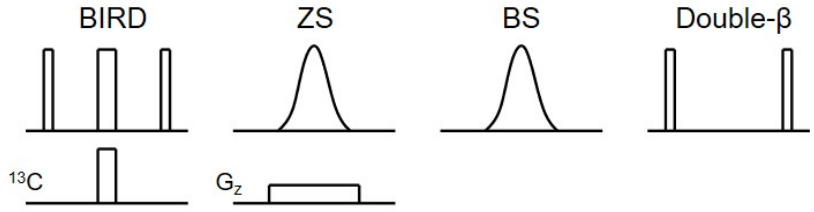

Figure 1.16: Spin refocusing techniques used in pure shift NMR

BIRD works via "natural abundance" filter, utilising a heteronuclear spin echo. This pulse sequence element provides a filter whereby, any nuclei not directly bound to a ^{13}C, are not detected. This method therefore has a sensitivity directly related to the natural abundance of ^{13}C (1.1%). This loss of signal can be problematic for 1D spectra. However, for 2D ^{13}C experiments, such as HSQC, there is no extra sensitivity penalty, with S/N increases from the collapsing of multiplets (if used with real-time acquisition). Another of the drawbacks of this is that geminal protons are not decoupled as they are bound to the same ^{13}C. This has been addressed via a modification of the BIRD element, in the pulse sequence "Perfect BIRD".[60]

Both ZS[30] and BS invert active spins using selective pulses. The difference between the two methods is that ZS uses gradients during pulses to spatially encode and refocus couplings, whereas band selective techniques utilise selective spin echoes, to refocus couplings. ZS gives a broadband pure shift spectrum, whereas BS gives a band-selective pure shift spectrum. Due to spatial encoding ZS suffers from low sensitivity, whereas band-selective techniques have excellent sensitivity.

Double β acquisitions work via a π rotation of a fraction $\sin^2\beta$ of spins. This is effectively a statistical selection of spins, which again results in a reduction of S/N. For reaction monitoring, decreasing S/N is not ideal, it can mean missing important intermediates.

In this thesis we develop a pure shift band-selective real-time pulse program, discussed in Chapter 4.

Multiple receivers

Multiple receiver technology is a recent development in NMR hardware. Having more than one receiver allows detection of multiple nuclei in a reduced time which allows an increase in efficiency and throughput, with multi-nuclear experiments for structural elucidation and analysis.[61] There are three main types of experiments: interleaved, parallel and sequential acquisition.[45] Examples of these experiments can be seen in Figure 1.17.

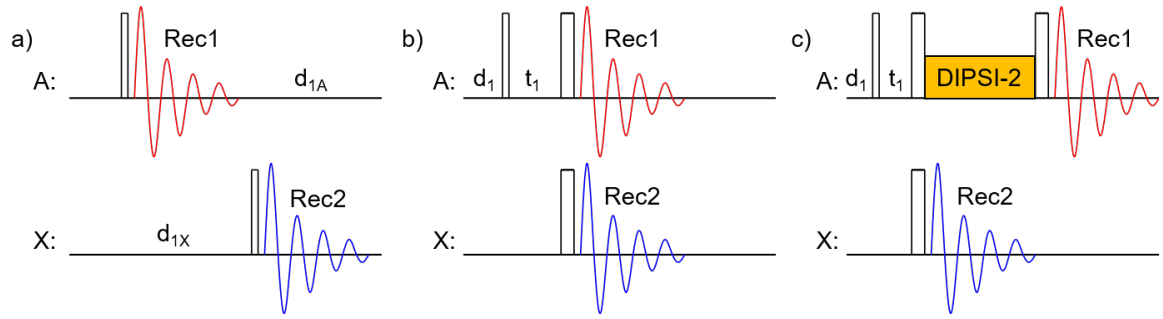

Figure 1.17: Example of multiple receiver experiments. Showing a) sequential 1D (A and X) b) parallel PANSY-COSY (A-A and A-X) c) interleaved PANSY-TOSCY (2D A-A and 1D X) NMR.

Sequential experiments allow nuclei to relax whilst the next pulse sequence and acquisition is executed, which is beneficial for slow relaxing nuclei. Parallel acquisition allows twice the amount of data to be obtained in one scan, ideal for nuclei with similar sensitivities and relaxation. Interleaved experiments mean that the dead time in NMR experiments are utilised, which increases efficiency during long experiments. The types of experiment combinations that are possible, especially for sequential and interleaved, are innumerable, and each acquisition type is appropriate for different NMR experiments.[62]

There has been much initial research and development of multiple receiver techniques using ^{1}H and ^{19}F,[45] due to their high natural abundances, sensitivity and similar gyromagnetic

ratios. The three categories of experiment each have their own advantages and limitations. Interleaved experiments are preferential for spin systems with negligible J couplings between A and X. Parallel acquisition experiments (PANSY)[45,49,61] allow multiple nD experiments to be ran, 1D experiments are limited by the slowest nuclei to relax, hence why similar behaving nuclei (such as ^{1}H and ^{19}F) are preferential. For nD parallel acquisition nuclei can give coherence transfer via the use of pulsing and gradients allowing two nD spectra to be obtained at once. Sequential acquisition experiments are essentially a combination of interleaved and parallel, obtaining data for one nuclei during a mixing period for the second nuclei.[45]

Each of these multiple receiver experiments require new pulse programs to be written to allow independent spectra to be acquired. The increase in NMR productivity can be utilised for kinetic measurements, allowing multiple nuclei to be monitored simultaneously. Combining multiple receivers with new fast NMR methods such as spatial encoding,[63] Hadamard encoding,[64] NUS sampling[65] and Ultrafast[66]/SOFAST[67] techniques can allow rapid nD (where n $>$ 1) spectra to be recorded.

1.2.7 From Sample to Spectrum

Although understanding how the spectrum is obtained and what information it gives is important, there are several steps before signal detection can occur. To obtain a spectroscopic measurement we first need to prepare a sample. Most often the sample is dissolved in a deuterated solvent, a solvent where the protons have been replaced with deuterium (^{2}H). Deuterated solvents are used so the magnetic field can be "locked" and any changes of the magnetic field compensated for. Using deuterated solvent also eliminates the need to suppress the proton solvent signal of protonated solvents which are very large in comparison to the dissolved sample due to NMR being a quantitative spectroscopic technique. The sample must be fully dissolved as solid matter will likely affect the magnetic field homogeneity and lead to a poor spectrum.

Once the sample is ready the instrument needs to be prepared which is done via tuning and matching, locking and shimming. Tuning involves tuning the resonance circuit to the

frequency of the nucleus to be pulsed and observed. Whilst matching refers to matching the impedance (resistance) of the probe and transmission (commonly 50 Ω).[68] The sample can also be "locked"; the lock follows the resonance of the deuterated solvent, and the magnetic field strength at this frequency. Locking is not essential for shorter experiments as the magnetic field drift is very slow. For high quality spectra, shimming is very important. The term shimming actually arose from the word shim, meaning to wedge due to old spectrometers using pieces of metal placed near the magnet producing additional magnetic fields to improve the homogeneity. These so called passive shims produced magnetic fields as the metal pieces were magnetised by the main magnetic field. Shimming now works via active shims, where electric currents in shim coils produce additional magnetic fields of specific geometry to minimise the inhomogeneity of the main magnet.

After the sample and probe are prepared, the pulse program can be initiated. Pulse programs are effectively instructions for the spectrometers: they contain information on the sequence and length of delays, pulses, pulsed field gradients, number of loops *etc.* At the end of the pulse program the signal acquisition is initiated where the instrument records the FID. As the FID is a record of the intensity vs. time, it must be converted to the desired format, intensity vs. frequency.[28]

This is done via a Fourier transformation (FT):

$$A(\omega) = \int A(t)[cos(\omega t) - isin(\omega t)]dt \tag{1.19}$$

Where ω represents frequency and the cosine and sine functionalities represent the "real" and "imaginary" parts of the FID respectively. The spectra obtained by the FT contains signals at Larmor frequencies which allows elucidation of the environments present in the sample.

Another consideration is the number of scans needed: more dilute samples or less sensitive nuclei can require a considerable number of scans. This means summing the FID to improve the signal-to-noise, however this again takes time. Altogether this can be a lengthy process, resulting in up to minutes before the spectrum is acquired. There are ways to reduce this time for reaction monitoring, i.e. shimming, tuning and matching on a "dummy" sample, and then inserting your kinetic run and initiating acquisition then. This can save a lot of

time, however it will still take at least 30 seconds to efficiently mix the sample, insert into the spectrometer and begin measurements.

1.3 Reaction monitoring by NMR

Commonly used methods for reaction monitoring are *in-situ* where the reaction is within the NMR tube, *on-line* whereby the reaction vessel is connected to the spectrometer via tubing or *off-line* where aliquots are taken from a reaction vessel, quenched and then studied. Each method has it benefits and short-comings. *In-situ* reaction monitoring allows the reaction to be studied in real-time, however the reaction solution needs to be thoroughly mixed, so there are no concentration gradients. Issues can therefore occur as there is no mixing of reactants in an NMR tube, which will affect the kinetics, when compared to rates when the mixture is stirred.[69] *On-line* techniques allow a representation of the reaction when being carried in the normal reaction vessel, however the flow of the sample impacts the spectra that can be obtained.[70,71] The flow not only can cause broadening of signals, but also the time the species spend in a magnetic field can have implications on quantification. *Off-line* techniques allow more time to study the reaction mixture, as the reaction has been stopped. However, quenching can cause species to decay, and the sample has been taken out of the reaction environment which also can impact the results seen.

For fast reactions the most appropriate methods are *in-situ* or *off-line* provided you have either stopped-flow or quench-flow apparatus. For *in-situ* analysis you need to make sure that the reactants are thoroughly mixed. Rapid quench-flow apparatus are commercially available, and have previously been used by the Lloyd-Jones group to study fast reactions.[11,12]

1.3.1 Stopped flow systems

Stopped-flow techniques were first described by Chance in 1940 and later by Milnes in 1964. Stopped flow was developed to allow rapid mixing and sampling to observe kinetics of fast reactions in the solution phase.[72] Syringes allow rapid injection of solutions into a mixing cell, and on to the observation chamber.[73] As the previous solution needs to be fully dis-

placed there will also be a dead volume.[74]

Stopped flow allows better measurement sensitivity as the solution can be held in the observation chamber for as long as required after initial injection. Stopped flow allows a dead time of hundreds of milliseconds, whereas hand mixing can take anything from seconds to minutes.

Another benefit of a stopped flow system is the pressure, temperature and atmospheric control a closed system is capable of. For this type of condition control there are factors that need to be accounted for, such as the flexibility and composition of the tubing, pressure build up within the system and achievement of homogeneity within the system.[20,75,76]

The key factor for stopped flow is efficient mixing. This can be achieved with rapid injections, which force the reagents into contact with each other.[77] This means density and viscosity of solutions need to be considered whilst deciding mixing speeds for the solutions (if control is available with the apparatus being used).

1.3.2 Stopped flow NMR

As discussed in Section 1.2.1, relatively slow relaxation of nuclei in magnetic fields prevents rapid data acquisition, especially compared to techniques such as IR, UV and fluorescence. The adverse consequences of relaxation can be minimised by the pulse program used either by smaller flip angles, more advanced NMR techniques or interleaving experiments. Before any NMR measurements the system must be allowed to reach equilibrium, allowing maximum signal after pulsing. The equilibrium can take any time between seconds to minutes to achieve, it is therefore imperative that the reagents must be pre-magnetised (i.e. reach equilibrium) prior to mixing and injecting into the observation cell. For this to occur the reagents must be within the magnetic field itself.

There are several reports about reaction monitoring by NMR, utilising different techniques.[77–82] The most common theme, is the rapid injection of solution A into solution B. Either via a coaxial insert or tubing holding solution A and it then being rapidly injected in to solution B.[77,78,81,82] Many variations on this apparatus have been used successfully for reaction monitoring by NMR, however the rapid injection causes perturbation and broadening of

the NMR signals until the mixture becomes homogeneous again. This broadening can be problematic for fast reactions, especially in crowded spectra such as ^{1}H NMR.[79]

Another methodology developed for reaction monitoring by NMR are new probes. They are specifically developed to allow rapid injection of solutions and monitoring the resulting spectra.[77,79,82] Another example is a micro-reactor probe head,[74] as well as flow probes, both of these examples replace the usual NMR probe for a specialised reaction monitoring probe. This can be less than ideal when warming up a cryoprobe is required. Bruker developed a flow probe, which is compatible with any 5mm probe (InsightMR). This flow probe will be briefly discussed in Chapter 2.

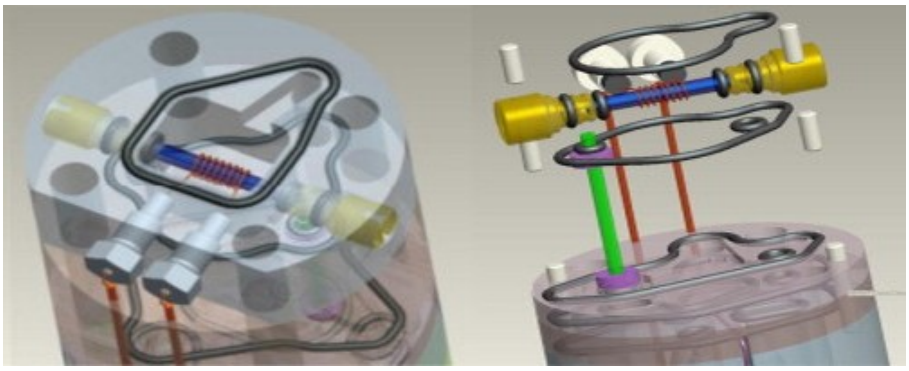

Figure 1.18: Micro-reactor probe head, reproduced from paper[74]

Chapter 2

Stopped flow NMR

2.1 Introduction

There are two main restrictions in studying fast reactions: the ability to initiate the reaction at a defined timescale, and the ability to observe the relevant changes in the system. Stopped-flow techniques have been developed and commercialised for a multitude of spectroscopic techniques. However, stopped-flow NMR had not been previously made as a commercially-available product. Bruker provided their product, *InsightMR* a continuous flow probe, as part of my PhD studentship. Initial testing was done with the Bruker system, and the stopped-flow NMR equipment was developed from the basic design of the continuous flow probe. The stopped flow NMR probe, *InsightXpress*, was made via a collaboration with the company TgK Scientific.

2.2 Results and Discussion

2.2.1 InsightMR probe

The original Bruker InsightMR flow probe, which can be seen in Figure 2.1, is a continuous flow probe which consists of a glass tube, sample holder, tubing to allow flow of sample in and out, temperature regulation lines and an insulating cover. The thermostating is provided by a Lauda Alpha R8 water bath and pump.

Figure 2.1: Bruker flow probe. Image reproduced from Bruker with permissions.

The flow probe was mounted on a stand which allowed syringes and tubing to be screwed into a moveable four way junction. InsightMR was designed for online reaction monitoring, meaning that the system pumps the reaction solution from a vessel through the system and back to the original vessel. To study fast reactions, reagents need to be held separately and measurements taken as soon as possible after mixing. To allow us to test not only the basics of the system such as fill volumes, but also effects on mixing, we attached a two syringe drive pump and a T-junction to the inlet valve, shown in Figure 2.2.

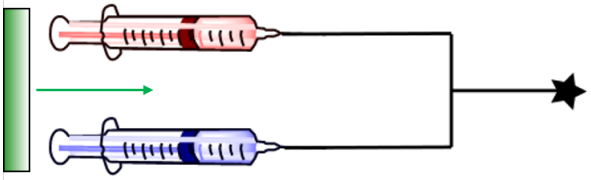

Figure 2.2: Diagram showing the two syringe drive set up. Where the green block and arrow show the driver block and the direction it pushes in. The star indicates the beginning of the flow system.

As InsightMR has previously been used as a continuous flow system, there was no provided information on fill volumes of the tubing, or the observation chamber. The volume of the observation chamber is however highly important in stopped-flow systems as completely flushing the system between runs is important to ensure no product remains in the cell, or this can lead to false kinetic data. Most of these tests required an unreactive system, so solutions of fluorobenzene **4**, trifluoroethanol **5** and trifluorotoluene **6**, seen in Figure 2.3, were used.

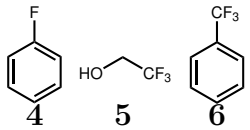

Figure 2.3: Chemical structures of FB, TFT and TFE

Fill volumes

To minimise the waste of chemicals, the volume of solution required to prime the inlet lines, and the volume of the observation cell is required. The solutions of **4** and **5** in methanol (0.1 M) were manually injected, at approximately 0.06 ml/s, and the process monitored using a pseudo 2D ^{19}F pulse sequence. The initial signal was seen at 19.96 s, and full signal achieved at 23.03 s, as can be seen in Figure 2.4. This was repeated pushing out the **4** solution with the **5** solution. This data showed the approximate volume the tubing held was 1.2 ml, and the observation cell holds approximately 0.2 ml (190 μl).

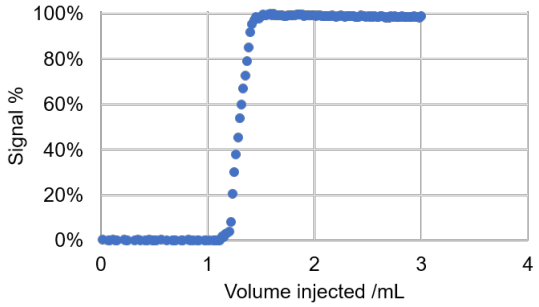

Figure 2.4: Graph showing the integral data obtained from injecting in of **4** into the flow probe. Initial signal seen at 1.2 mL injected and 100% signal seen at 1.4 mL.

Tube diameter effects

A range of different sized NMR tube fittings were supplied by Bruker including 2.5 mm, 3 mm and 5 mm diameter versions. Each tube was tested using a 1 M solution of **4** in methanol and the signal to noise (S/N) was measured, Table 2.1. For comparison, a normal 5 mm NMR tube was also tested to assess the effects of the thin Tefzel tubing within the NMR tube, denoted 5mm* in the table.

Table 2.1: Signal-to-noise comparison for each of the different tube sizes provided by Bruker, where 5 mm* is a standard NMR tube without any tubing inside. V_{rel} is the expected relative volumes based on the diameter of the tubing. ^{19}F data from a 1M solution of fluorobenzene in methanol. ^{1}H data from the -CH_3 peak of methanol. Integrals normalised to %.

Tube diameter	V_{rel}	^{1}H (%)	^{19}F (%)
2.5mm	0.25	25	23
3mm	0.36	27	24
5mm	1.00	90	96
5mm*	1.00	100	100

A loss of sensitivity is expected when reducing the diameter of the tube. The reduction in the volume required for each experiment can outweigh the loss in sensitivity when using expensive materials. Reducing the active volume can also be beneficial when using PFG, as discussed in Chapter 1.

Rate of injection effects

Initial testing explored the effect of the rate of injection on the mixing and spectra. Alternating 5ml injections of **4** and **5** in methanol were performed while acquiring pseudo 2D ^{19}F spectra. The alternating 5 ml injections allowed visualisation of the mixing and purging of reagents.

The injections were performed using a syringe drive mount which controlled injection rates. The rate of injection was varied between 30 – 60 ml/hour in 10 ml intervals. There were no differences in the effective purging or mixing between each flow rate as can be seen in Figure 2.5.

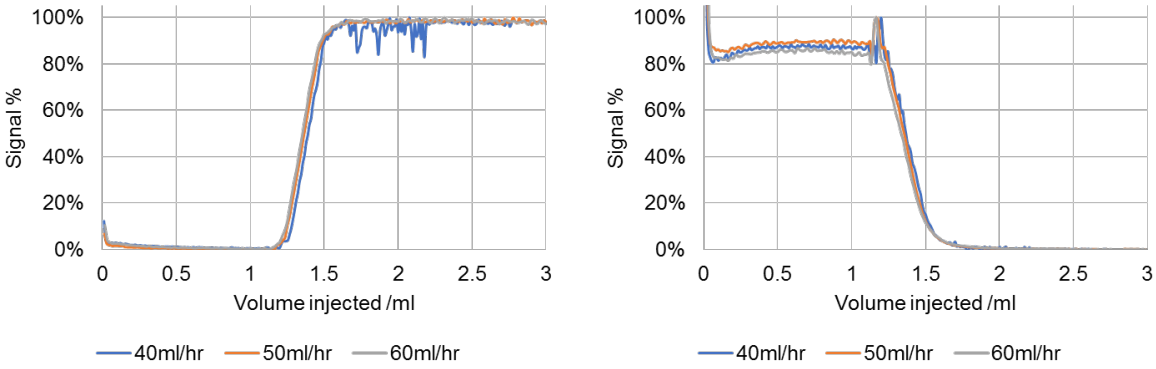

Figure 2.5: Comparison of flow rates injecting in and purging out fluorobenzene solution from the flow probe.

There was however a large difference in the purging abilities between the two solutions, as can been seen in Figure 2.6. The solution of **4** was much more effective at displacing the solution of **5**. Due to the solutions varying in both viscosity and density, further testing was needed to see which factor was affecting the displacement, as discussed next.

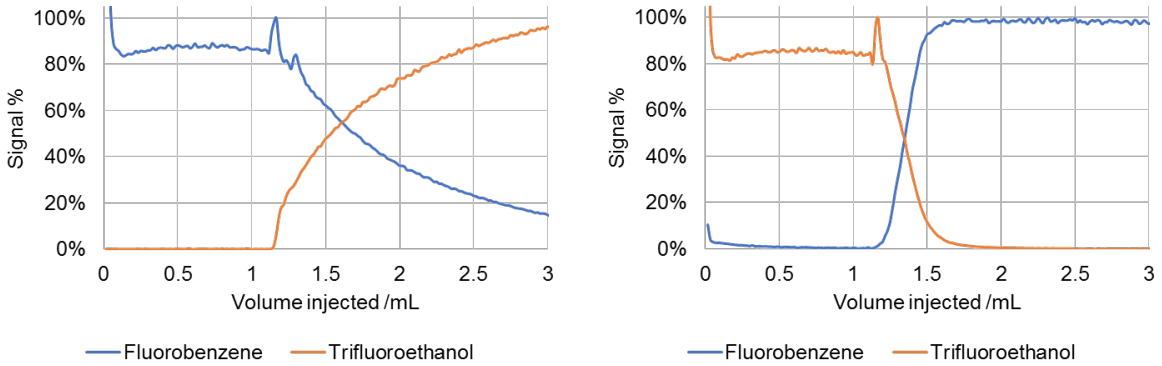

Figure 2.6: Comparison of injection/purging fluorobenzene and trifluoroethanol solutions.

Viscosity and density effects

To test the impact of density and viscosity solutions with **4** (in each solvent) and pure solvent were injected alternately. This allowed comparison of both mixing the fluorobenzene solution in, and purging the fluorobenzene solution out. Comparison of the alcohol series allowed viscosity effects to be observed due to the similarity of the density.

Table 2.2: Viscosity and Density of Organic Solvents

Solvent	**Viscosity /cp, 293 K**	**Density /g mL^{-1}**
Methanol	0.55	0.791
Ethanol	1.10	0.816
Propan-1-ol	2.26	0.804
Butan-2-ol	2.95	0.810
Chloroform	0.58	1.492

Normally when injecting into the observation cell, the solution enters via the red tubing - as shown in Figure 2.7. This then forces out the "old" solution via a small hole at the top of the observation cell and flows out through the wider green tubing. Prior to these experiments we tested the effects of "reversing" the flow, to see if this had any effect with injecting and purging. These experiments revealed no real differences in purging/injecting abilities. The set up was then left in "reverse" flow for these experiments, and will only be used in these experiments due to the more noisy NMR spectra.

The alcohol series allows comparison of varying viscosity, and as can be seen in Figure 2.8, injecting and purging show no large differences.

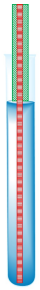

Figure 2.7: Schematic of stopped flow probe tube. Red tubing indicates the inlet tube, and green the exit tubing.

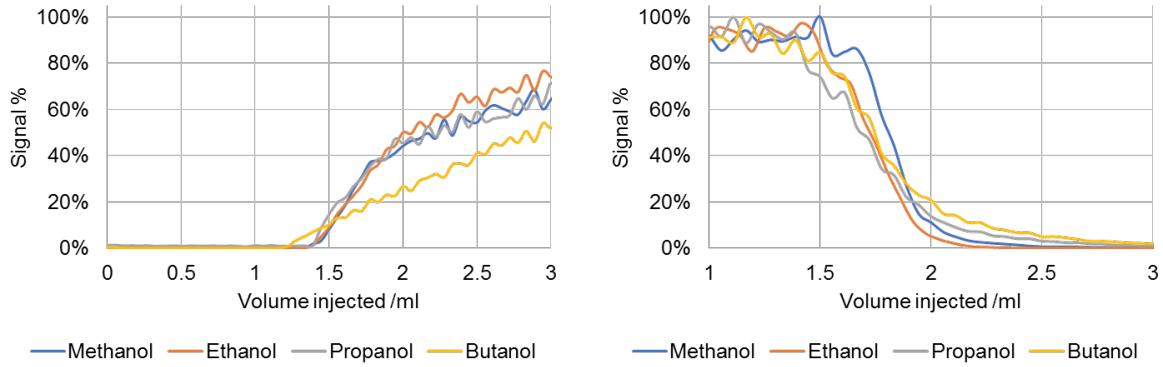

Figure 2.8: Viscosity effects on mixing, tested using an alcohol series. Monitored using ^{19}F NMR of **4** signal (δ -115 ppm), signal shown as a percentage to allow for variation in concentration in each solution.

Comparison of methanol and chloroform, showing effects of density only, showed large differences between the two. Purging and mixing with chloroform solution showed rapid displacement, taking only 400 μL once the inlet lines have been purged. The increase in density therefore aids in pushing the lighter solution out of the observation cell. From the tests it shows that the viscosity has no effect on the displacement of solutions at flow rates possible with this set up; however density does. The more dense the solution the easier it is to purge out the other, less dense, solution in the normal set up.

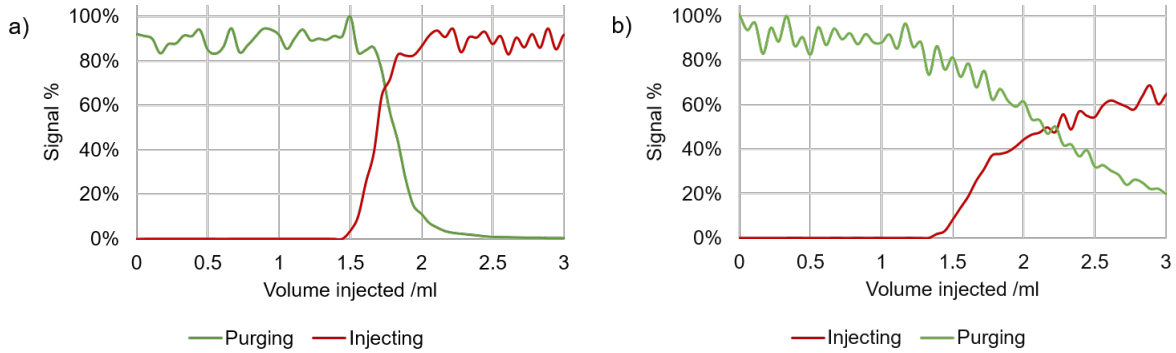

Figure 2.9: Density effects on mixing, tested using methanol and chloroform solutions. Monitored using ^{19}F NMR of **4** signal (δ -115 ppm), signal shown as a percentage to allow for variation in concentration in each solution. Where a) is the chloroform solution, and b) is the methanol solution.

Testing the magnetic field strength

The equilibrium state of nuclei in a magnetic field was described in Section 1.2.1, the population difference of individual spin states is dependent on the magnetic field strength. As the sample of **4** in methanol is moved away from the centre of the magnet, the strength of

the magnetic field felt by the nuclei decreases. To aid in reaction monitoring, the nuclei need to be pre-magnetised so initial kinetic data can be obtained. To aid the design of the probe, testing was done to obtain pre-magnetisation vs. distance from the centre of the magnet. To test this, the flow probe was held at varying distances from the centre of the magnet for two minutes to allow equilibrium to be reached. The probe was then rapidly inserted to the centre of the magnet and measurements initiated. This was repeated several times at each distance; the integral intensities of the observed signals are shown in Figure 2.10.

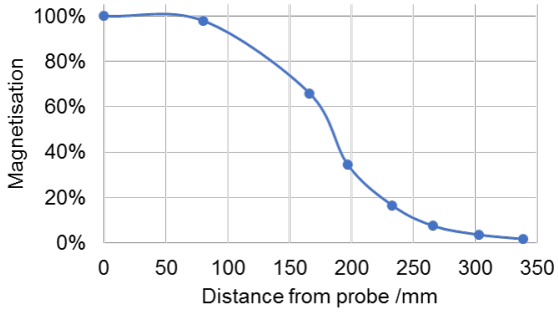

Figure 2.10: Signal intensity variation as you move away from the centre of the magnet. Showing the pre-magnetisation at increasing distance from the centre of the bore of the magnet.

The graph indicates that the magnetic field strength rapidly decreases, and less than 80% magnetisation is observed at 150 mm away from the centre of the magnet. This data established that we needed reservoir coils as close as possible to the centre of the magnet to maximise pre-magnetisation, ideally in the 100 mm range.

Conclusions

The testing of the InsightMR flow probe established clear initial goals for the stopped flow system: an effective mixing block, pre-magnetisation coils <150 mm away from the centre of the magnet. Other specifications included 3 separate inlets, communication with the spectrometer to allow dead times to be accurately calculated. These specifications were given to TgK Scientific who then produced an initial prototype of both hardware and software, for testing which will be discussed next.

2.2.2 Stopped flow NMR probe prototype 1

The initial stopped flow kit consisted of a 3 pump syringe drive. Trigger out (and in) BNC, TTL/CMOS 0-5V connections which facilitate communication between the syringe pump drive and the NMR console. Communication and control of the syringe drive is performed using the program KinetaDrive, provided by TgK Scientific. KinetaDrive allows inputs for injection speed, total volume of injection, and the ratio of input from each syringe as can be seen in Figure 2.11.

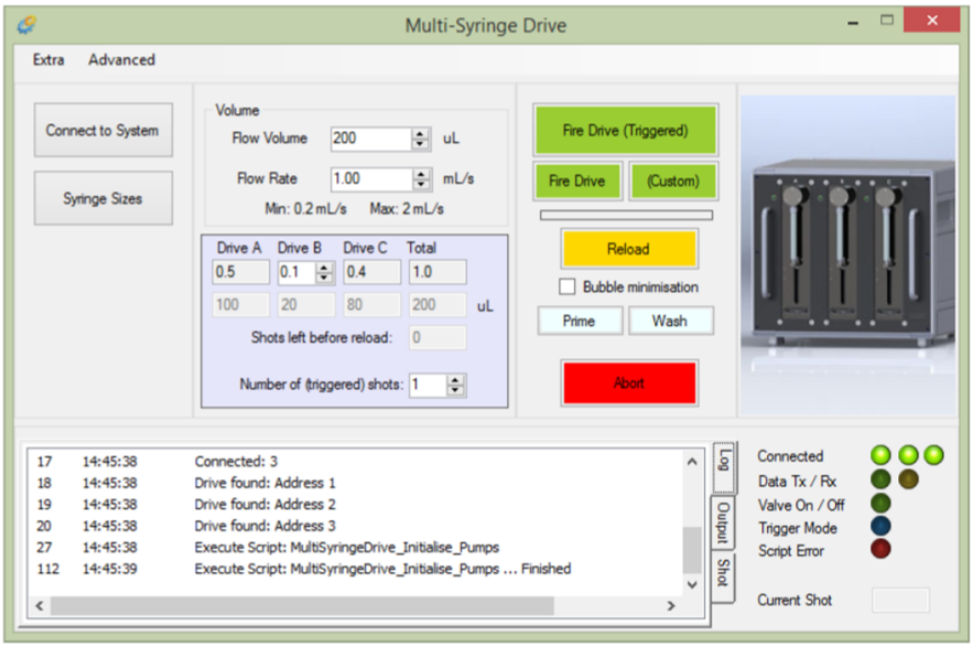

Figure 2.11: Kineta Drive software: Allowing inputs for total volume injected, injection rate (0.1 - 2 mL/s), ratios of syringes, prime function - which primes all the lines by injecting 1.5mL, wash function - which pulls in the solution in the wash lines, bubble minimisation which rapidly pulls in and out solutions to minimise bubbles.

Connection of the syringe pump and computer is achieved via a RS232 connection. The head of the flow probe, shown in Figure 2.12, is externally similar to the Bruker InsightMR head, however the umbilical is modified. The new umbilical contained three inlet tubes as opposed to the original one tube. Above the head there are three reservoir coils of varying sizes, and above these the mixing block. These coils allow the three solutions to be pre-magnetised prior to mixing and injection into the observation tube. Above the coils the mixing cell is housed, which consists of three "in" tubes which are screwed in, and one out tube which flows into the observation chamber. After the observation cell the tubing

exits the system and the waste is collected in a syringe or beaker. The length of tubing is housed in a plastic ringed cover, which has temperature regulating flow tubes connected to allow thermostating of the system. A basic schematic of the set up can be seen in Figure 2.12.

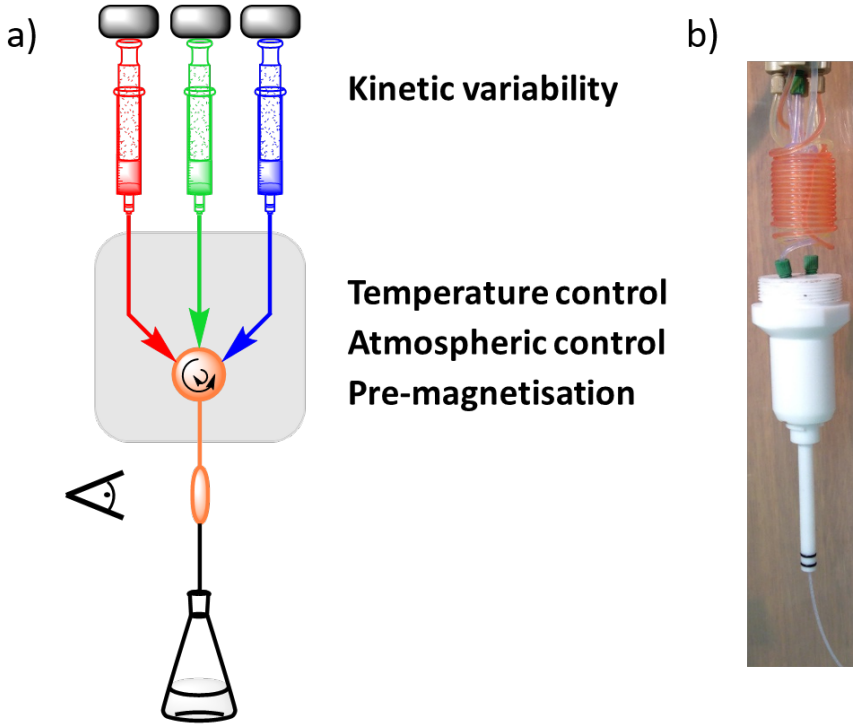

Figure 2.12: a) General scheme of the stopped flow NMR set up: 3 independent syringe drives allows kinetic variability, aiding kinetic evaluation. Grey box indicates the umbilical, which is thermostated, containing the mixing cell and pre-magnetisation coils. The sealed system allows atmospheric control, when connected to the desired gas inlets. The observation cell then allows flow out into the waste. b) Internal set-up inside the head of the umbilical

Temperature testing

The new probe system thermostating was tested using methanol. Methanol is commonly used in NMR for temperature calibrations between 178 and 330 K using well known calibration equations,[83] Equation 2.1. The chemical shift differences, $\Delta\delta$, for the two proton signals of methanol indicate temperature of the sample.

$$T(K)methanol = 409.0 - 36.54\Delta\delta - 21.85(\Delta\delta)^2 \tag{2.1}$$

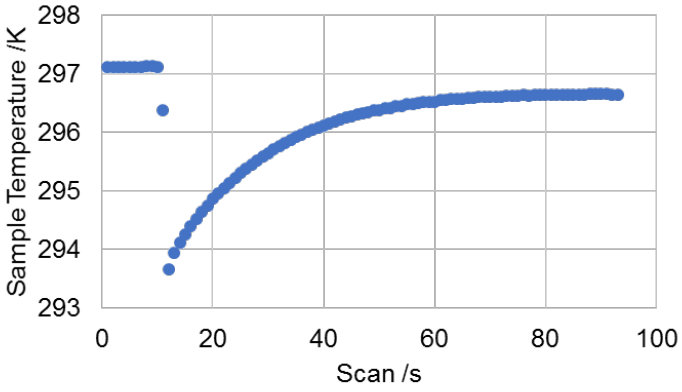

Figure 2.13: Data showing the difference in temperature between the thermostating bath and of the solution upon injection into the NMR spectrometer, using peak positions of methanol. Injection at scan 11. Bath temperature set to 288 K and spectrometer set to 297 K.

As can be seen in Figure 2.13 the temperature of the initial solution held in the probe is constant. The injection at scan 11 produced a drop in temperature by 3.5 K. The solution in the observation cell is then heated up by the air flow within the probe to the desired temperature. The injected solution should have been at 288 K, however it only reached 293.6 K. The stopped flow probe temperature decreased at the region of the mixing cell and reservoir coils, which could be felt by hand at high temperatures. The thermostating pump was set at a rate of 15 L/min, however due to the flow probe being held high above the bath, this was not the actual flow rate achieved. This combined with the decrease in space to flow past the mixing cell caused the thermostating to be ineffective: this serious issue was addressed in prototype 2.

Coil volume testing

SFNMR set-up with: Fluorobenzene in A, trifluoroethanol in B and trifluorotoluene in C. The system was then primed ,i.e. the reservoir coils were filled from the reagent syringes. Note that the coils increased in size from A to C.

Varying the volumes injected from each syringe allowed calculations of the volume of sample that is pre-magnetised in the reservoir coils using the integrals of the ^{19}F signal from each solution. The data showed the volume of pre-magnetisation from each reservoir coil: A - 500 μl, B - 600 μl and C - 700 μl. This data is in agreement with UV test data acquired by TgK Scientific.

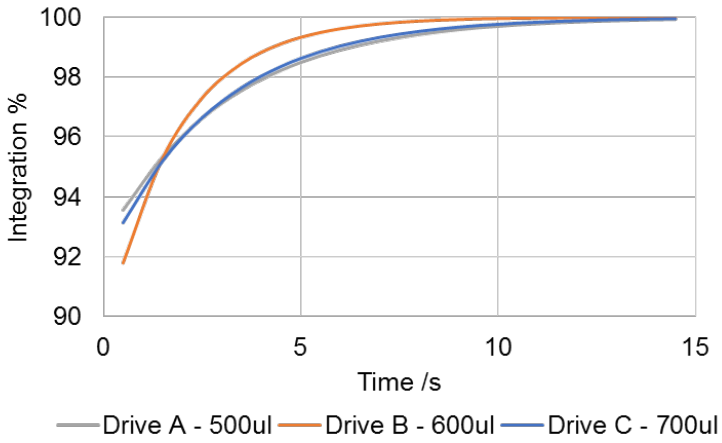

Figure 2.14: Pre-magnetisation testing for coils A B and C. Showing the >90% magnetisation for each coil, at varying volumes.

Contamination testing

During high speed injections a pressure builds up in the system. This can lead to unwanted flow after injections, the primary concern being the pull back from the mixing cell contaminating the pre-magnetisation coils. To confirm there was no contamination, experiments were performed with a concentrated solution of **4** (1M), a dilute solution of **6** (0.08M) and solvent (water/dioxane 1:1). Initially an injection is fired from each syringe at 1.6 ml/s. This is followed by two injections from the solvent syringe, to clear the mixing and observation cell. Followed by a final injection from the dilute solution to see if any of the concentrated solution had been "pulled back" into the dilute solution pre-magnetisation coil. This was

repeated, having the concentrated solution in A, B and C to confirm each of the inlet lines behaved the same. For each inlet there was no visible contamination of the dilute solution with the concentrated solution.

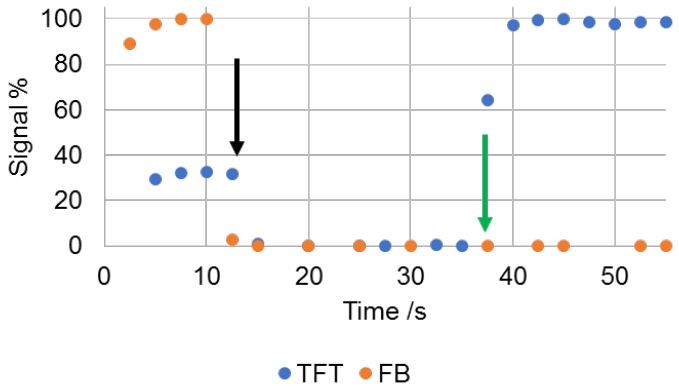

Figure 2.15: Testing of concentrated 1 M fluorobenzene solution and dilute 0.08 M trifluorotoluene solution to confirm no pull back being caused from pressure building up in the system. Data normalised to signal % to allow integrals of each solution to be visible on one axis. All three syringes fired at time 0, followed by 2 shots of solvent the first of which is donated by a black arrow, then one shot of the dilute trifluorotoluene donated by a green arrow.

Conclusions

Based on the initial testing dicussed we wanted to improve the pre-magnetisation, temperature control and flushing of the system between kinetic runs. Modifications were made by TgK scientific, each of the modifications were tested and the results discussed next.

2.2.3 Stopped flow NMR probe prototype 2

After feedback from experiments, TgK Scientific produced a second prototype the SFNMR equipment. These changes were of the pre-magnetisation coils, temperature control unit, and mixing chamber; each of these modifications have been explored in this section.

Improved premagnetisation

The only way to improve the premagnetisation was to locate the coils closer to the centre of the magnet. This was done by TgK scientific, by remaking the original probe head. The plastic housing was remodelled to allow the premagnetisation coils to be housed in a tiered manner, allowing stronger premagnetisation of A.

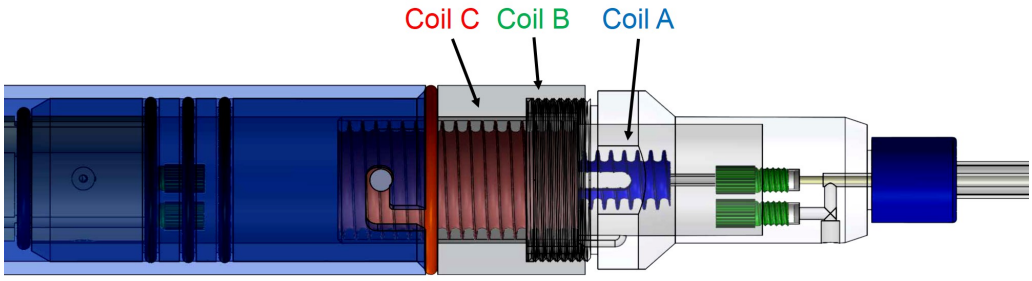

Figure 2.16: Image showing the internal set up of the SF-NMR probe head. pre-magetisation coils are stacked on top of each other in a Russian doll format. Image reproduced from TgK Scientific.

To test the pre-magnetisation and volume of each of the coils, solutions were pushed through each of the inlets. The pre-magnetisation varies between 92-95%, with coil A (blue) being the most pre-magnetised, as can be seen in Figure 2.16. The volume of each coil has been calculated in the same way shown in Figure 2.10, yielding the results: A - 860 μL, B - 700 μL, C - 600 μL.

Improved temperature control

The temperature control was failing in two ways: the pump was not powerful enough and the premagnetisation coils were constricting flow. To overcome these issues we replaced the Lauda Alpha R8 water bath and pump with a Huber Grand Fleur Pilot One. The Huber system allowed process temperature monitoring, using a PT100 resistor. The PT100 resistor

was placed in the umbilical adjacent to the premagnetisation coils, so that the temperature of the solutions can be monitored prior to injection. This then provides feedback to the Huber which can change the temperature of the system to get the process temperature to the desired temperature.

Another improvement was made by modifying the mixing block. Previously it was cylindrical, impeding the flow of thermostating liquid past it to the premagnetisation coils. Three semi-circle grooves where made in the edge of the mixing block to facilitate flow of the thermostating liquid down to the pre-magnetisation coils.

To calibrate the temperature of a NMR spectrometer, methanol and ethylene glycol are commonly used. The temperature is calculated via the change in chemical shift ($\Delta\delta$).[83]

$$\text{Methanol} = 409 - 36.4\Delta\delta - 21.85(\Delta\delta)^2 \text{ between 178 and 330K}$$

$$\text{Ethylene glycol} = 466.5 - 102.00\Delta\delta \text{ between 273 and 416K}$$

Bruker provided calibration samples, are dry and sealed. To test the SF-NMR standard Sigma Aldrich methanol was used, which is wet. Before testing the system we wanted to confirm the water would not affect the temperature calibration.

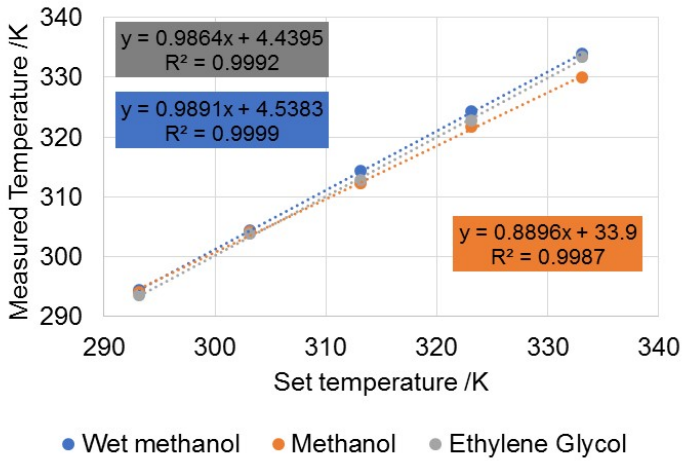

Figure 2.17: Temperature calibration using ethylene glycol, methanol and wet methanol. The ethylene glycol and wet methanol show the strongest correlation to the set temperature.

Following on from the wet methanol testing the full SF-NMR temperature range, 278 – 333 K, was tested. The temperature of the sample had a variation of ± 2.5 K, as can be seen in Figure 2.18. For the experiment each temperature was set, and after 2 minutes an injection

fired from each syringe drive and the temperature averaged.

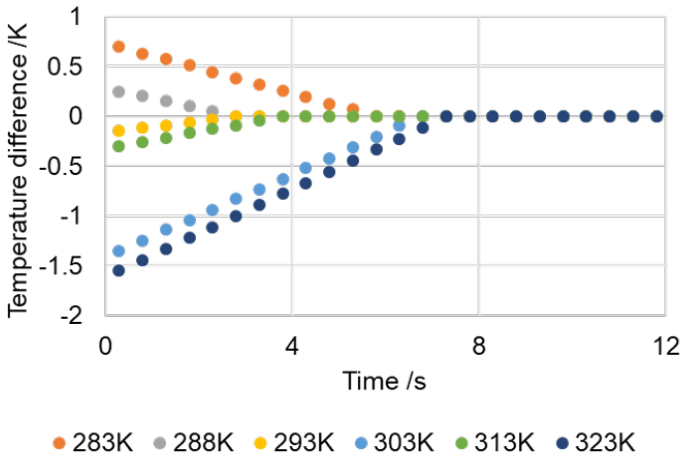

Figure 2.18: Temperature testing of the new umbilical, using (wet) methanol. The difference in sample temperature vs. the set temperature.

Improved mixing block

As mentioned previously the mixing block was modified to add in grooves to allow better flow of the thermostating liquid. As well as this, a flush line was added, which is directly connected at the top of the mixing block to allow previous reagents to be fully removed. The angle of the three inlet lines were also modified to improve mixing and prevent back flow during pressure build ups within the system.

2.2.4 Reaction monitoring using SF-NMR

Once the SF-NMR kit was up and running we wanted to test its capabilities and showcase the benefits of the equipment. To illustrate these benefits, several fluorinated phenyl boronic acids were used, and the protodeboronation kinetics studied. This reaction has been extensively studied by the Lloyd-Jones group,[11] and therefore allowed us to compare and contrast the different methods for reaction monitoring.

Eyring analysis of 2,3,6-trifluorophenyl boronic acid

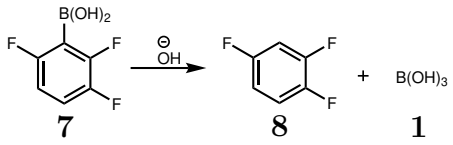

Figure 2.19: Protodeboronation reaction of **7** in the presence of KOH to give **8**

The protodeboronation of **7** has been studied by the Lloyd-Jones group using SFIR, as well as RQF. To show the capabilities of the SFNMR, as well as confirming that both methods give the same results, and Eyring analysis was performed. It should be noted that all IR data was obtained by another member of the Lloyd-Jones group, Marc Reid, and is only used in this section to compare results obtained by the SFNMR.

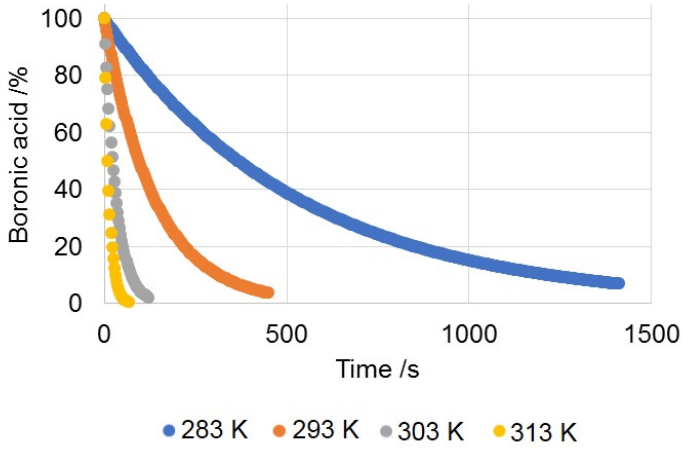

Figure 2.20: Kinetics from the ^{19}F F-3 integral of **7** at varying temperatures

The SFNMR results are shown in Figure 2.20, as can be seen the graph follows a first order decay as expected. The time scales of some of these reactions are so fast that without the SFNMR, some (if not all), of the reaction will be missed. With the SFNMR this analysis is very easy, the solutions are held within the thermostating, and all that is needed is for the solutions to equilibrate at the desired temperature.

We also wanted to confirm the two SF techniques produced the same results, and there were no issues with either set up. To do this the Eyring analysis was extended to higher temperatures, still able to be studied by SFIR and the data collated.

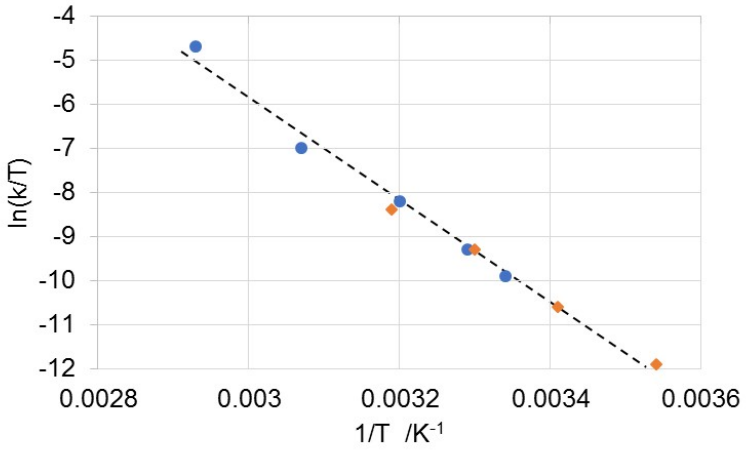

Figure 2.21: Eyring analysis of the protodeboronation of **7**, comparing both SFNMR (orange diamond) and SFIR (blue circle)

As can be seen in Figure 2.21 the SFIR and SFNMR data have good agreement. The analysis yielded a $\Delta H^{\ddagger}$ of 25.5 kcal mol^{-1}, and $\Delta S^{\ddagger}$ of + 6.2 cal mol^{-1} K^{-1}. The Eyring analysis took only 2 hours, to do this manually would have taken a minimum of 1 day.

pH analysis of 2,3,4,6-tetrafluorophenyl boronic acid

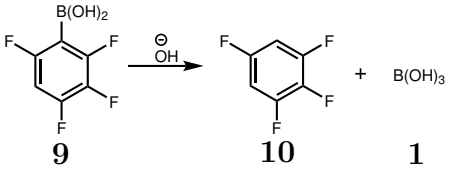

Figure 2.22: Protodeboronation reaction of **9** in the presence of KOH, to give **10**

Next a pH titration of the protodeboronation of **9** was performed. This entailed 14 experiments, using variable concentrations and equivalents of the KOH solution, further details in the experimental section of this chapter.

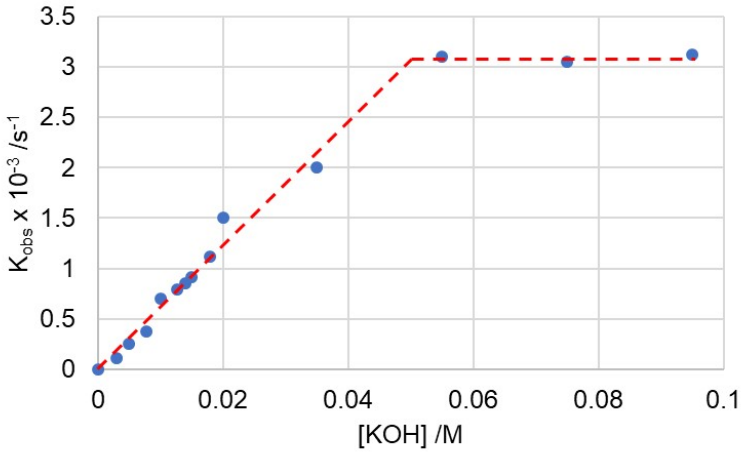

Figure 2.23: Reaction rates from the ^{19}F F-4 integral of **9** at varying KOH concentrations. The dashed line indicating the rate expected.

The graph depicted in Figure 2.23 shows data from the 14 reactions which were studied, all of which were acquired in less than 3 hours. This required 4 stock solutions: solvent, boronic acid and two KOH solutions of varying concentration. This type of analysis without the SFNMR would take around 3 days. From the graph one can see the rate increases linearly, up until a ratio of 1:1 boronic acid:KOH is reached where it reaches a plateau.

Rapid kinetics of 2,3,5,6-tetrafluorophenyl boronic acid

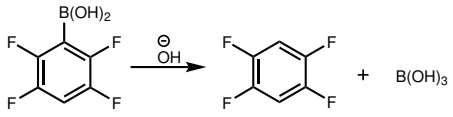

11 **12** **1**

Figure 2.24: Protodeboronation reaction of **11** in the presence of KOH, to give **12**

Stopped flow techniques allow initial data of reactions to be obtained, with a known dead time. However SFNMR, due to NMR relaxation times, has relatively low data density which can be problematic for fast reactions. Due to the communication between the SFNMR equipment and the NMR spectrometer, to build data density of "fast" reactions, we coded a pulse program to have a delay between SFNMR injection and initiation of the pulse program. This allowed us to study the rapid protodeboronation of **11**, building up data density using initial delays of varying lengths.

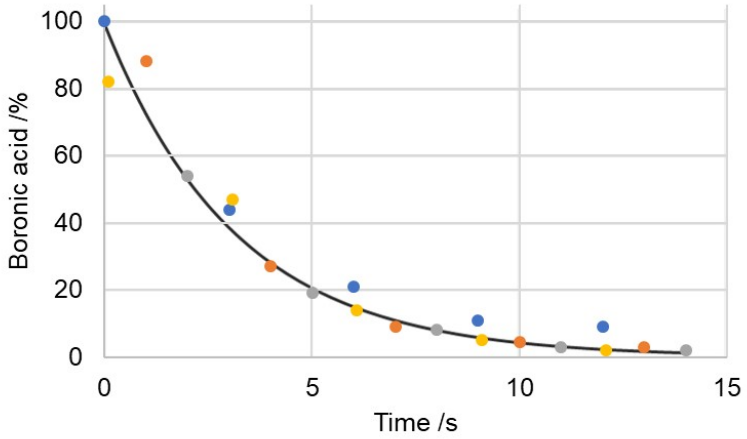

Figure 2.25: Integrals from the ^{19}F F-4 integral of **11** from several different kinetic runs

The combined kinetic runs, shown in Figure 2.25, show the integrals of the boronic acid over time. Analysis of the data showed the half-life of this reaction was just 2.2 s. Without the SFNMR equipment, a reaction with $t_{\frac{1}{2}} \geqslant 15$ s would be able to be studied.

Dual receiver kinetics of 2,3,6-trifluorophenyl boronic acid

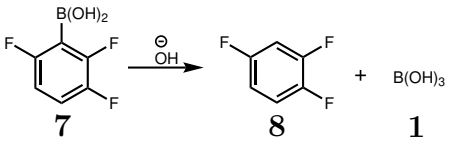

Figure 2.26: Protodeboronation reaction of **7** in the presence of KOH, to give **8**

After increasing data density using repeat runs, we next wanted to combine a new NMR technique which increases data density with SFNMR, dual receiver NMR. Parallel receiver technology requires a second (or third, fourth...) receiver, and modified pulse programs, examples can be seen in Chapter 7. This dual receiver technology was used to study the protodeboronation of **7**.

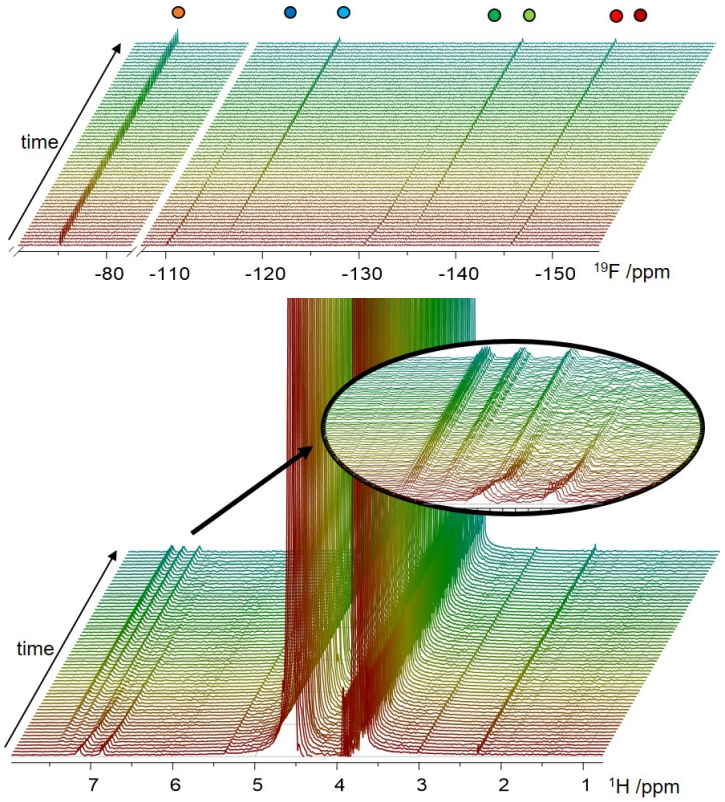

Figure 2.27: ^{19}F and ^{1}H stacked spectra, showing the protodeboronation of **7**. The coloured circles in the ^{19}F spectra depict the following: orange square - TFA, blue - F-2, green - F-6, red - F-3 (where the circles indict the boronic acid starting material, and the triangles the phenyl product).

The results obtained in Figure 2.27 follow the expected results from previously studied protodeboronation of **7**. However, the additional information obtained from the ^{1}H data could be very crucial for unknown reaction mechanisms.

2.3 Conclusions

We have developed a SF-NMR system which has three pre-magnetised (92-95%) coils which allow rapid reaction monitoring, and a flush line to clear the mixing cell and observation chamber. The umbilical is fully thermostated, with the option of atmospheric control. The SF-NMR system is able to send a signal to the NMR console after injection to initiate pulsing. This communication function also allows building up of data density, as you can modify the initial delay and combine data sets.

The application of the SF-NMR kit allows not only initial kinetic data, also the build up

of data density from repeat kinetic runs, as well as rapid analysis with varying conditions. The system is now being commercialised.

2.4 Experimental

All data was acquired on a two-channel 400 MHz Bruker Avance III NMR spectrometer equipped with a Prodigy probe at 300K unless otherwise specified.

The data seen in Table 2.1 was acquired from a solution of 1M FB (**4**) in d-MeOH. A standard 1D pulse program - zg was used. ^{1}H parameters: 0 dummy scans, 1 scan, acquisition time 3.98 s, 90° 8.05 μs, o1p 6.175 ppm and spectral width 20.548 ppm. ^{19}F parameters: 0 dummy scans, 1 scan, acquisition time 1.47 s, 90° 8.70 μs, o1p -63.0 ppm and spectral width 237.121 ppm.

The data seen in Figure 2.5 and Figure 2.6 were acquired from solutions of 2M FB (**4**) and 0.6M TFE (**5**) in methonal. The ^{19}F spectra that were analysed were acquired using: 0 dummy scans, 1 scan, acquisition time 0.99 s, 90° 8.70 μs, o1p -96.0 ppm and spectral width 50.1 ppm. The injections were of 5 mL of FB then 5 mL of TFE, each described in the figures, of varying rates of 40, 50 and 60 mL/hour.

The data seen in Figure 2.8 and Figure 2.9 were acquired from solutions of 1M FB (**4**) in methanol, ethanol, propan-1-ol, butan-2-ol and chloroform. The ^{19}F spectra that were analysed were acquired using: 0 dummy scans, 1 scan, acquisition time 0.4 s, 90° 1.45 μs, o1p -63 ppm and spectral width 237 ppm.

The data seen in Figure 2.10 were acquired from a solution of 1M FB (**4**) in methanol. The ^{19}F spectra that were analysed were acquired using: 0 dummy scans, 1 scan, acquisition time 0.78 s, 90° 8.7 μs, o1p -92 ppm and spectral width 120.7 ppm. This was done using a pseudo2D pulse program, using 32 scans.

The data seen in Figure 2.13 were acquired from a solution of methanol. The ^{1}H spectra that were analysed were acquired using: 0 dummy scans, 1 scan, acquisition time 0.5 s, 90° 8.25 μs, o1p 6.175 ppm and spectral width 20.5 ppm. This was done using a pseudo 2D pulse program, using 200 scans. The data was then analysed using 2.1, taking the peak positions of the -CH_3 and -OH, and the differences between these signals in Hz.

The data seen in Figure 2.14 were acquired from a solution of 1M FB (**4**), TFE (**5**) and TFT (**6**) in methanol. The SF-NMR set up was FB in syringe A, TFE in syringe B, TFT in syringe C. The ^{19}F spectra that were analysed were acquired using: 0 dummy scans, 1 scan, acquisition time 1.5 s, 90° 8.70 μs, o1p -63.0 ppm and spectral width 237.1 ppm. This was done using a pseudo 2D pulse program, using 30 scans. Varying volumes were used until the volume used had the maximum pre-magnetisation.

The data seen in Figure 2.15 were acquired from a solution of 1M FB (**4**) and 0.08M TFT (**6**) in 1:1 water-dioxane. The ^{19}F spectra that were analysed were acquired using: 0 dummy scans, 1 scan, acquisition time 3.57 s, 90° 8.70 μs, o1p -100 ppm and spectral width 99.6 ppm. To test the contamination one shot from all three syringes, two shots of solvent, then a final shot from the dilute solution. This was repeated varying which solution was in each syringe.

The data seen in Figure 2.17 were acquired using "wet" methanol (i.e. from an open bottle of methanol), bruker standard NMR temperature calibration samples of both methanol and ethylene glycol, using a zg30 pulse program. The ^{1}H spectra that were analysed were acquired using: 2 dummy scans, 8 scans, acquisition time 3.98 s, 30° 2.68 μs pulse, o1p 6.175 ppm and spectral width 20.5 ppm. The data was then analysed using 2.1, taking the peak positions of the -CH_3 and -OH, and the differences between these signals in Hz. This was repeated at varying temperatures: 293 - 333 K, in 10 K intervals.

The data seen in Figure 2.18 were acquired using "wet" methanol (i.e. from an open bottle of methanol). The ^{1}H spectra that were analysed were acquired using: 0 dummy scans, 1 scan, acquisition time 1.5 s, 90° 8.05 μs pulse, o1p 6.175 ppm and spectral width 20.5 ppm. Using a pseudo2D pulse program with 32 separate scans. The data was then analysed using 2.1, taking the peak positions of the -CH_3 and -OH, and the differences between these signals in Hz. This was repeated at varying temperatures: 278 - 333 K, in 5 K intervals.

The data obtained in Figure 2.20, and Figure 2.21 were obtained using 3 stock solutions: 0.1M 2,3,6-trifluorophenyl boronic acid (**7**) and 0.01M TFA, 0.2M KOH and solvent (1:1 H_2O:dioxane). The solutions were connected to syringes A, B and C, in the order stated at ratios 0.5, 0.3 and 0.2. The acquisition parameters used were: 0 dummy scans, 1 scan, acquisition time 1.5 s, 90° 8.05 μs pulse, o1p -63 ppm and spectral width 237 ppm. Each

kinetic run was performed at a different temperature, between 283 - 313K, in 10 K intervals.

The data obtained in Figure 2.23 were obtained using 4 stock solutions: 0.1M 2,3,4,6-tetrafluorophenyl boronic acid (**9**) and 0.01M TFA, (0.2M and 0.05M) KOH and solvent (1:1 H_2O:dioxane). The solutions were connected to syringes A, B and C, in the order stated, at varying ratios. The acquisition parameters used were: 0 dummy scans, 1 scan, acquisition time 1.5 s, 90° 8.05 μs pulse, o1p -63 ppm and spectral width 237 ppm.

The data obtained in Figure 2.25 were obtained using 3 stock solutions: 0.1M 2,3,5,6-tetrafluorophenyl boronic acid (**11**) and 0.01M TFA, 0.2M KOH and solvent (1:1 H_2O:dioxane). The solutions were connected to syringes A, B and C, in the order stated, at ratios 0.5, 0.3 and 0.2. The acquisition parameters used were: 0 dummy scans, 1 scan, acquisition time 1.5 s, 90° 8.05 μs pulse, o1p -63 ppm and spectral width 237 ppm.

The spectra shown in Figure 2.27 were obtained using 3 stock solutions: 0.1M 2,3,6-trifluorophenyl boronic acid (**7**)and 0.01M TFA, 0.2M KOH and solvent (1:1 H_2O:dioxane). The solutions were connected to syringes A, B and C, in the order stated, at ratios 0.6, 0.4 and 0. The data was acquired on a 400MHz Bruker Neo spectrometer equipped with a Smart probe at 300K. The acquisition parameters used for the ^{19}F spectra were: 0 dummy scans, 1 scan, acquisition time 2.3 s, 90° 15 μs pulse, o1p -125 ppm and spectral width 301 ppm. The acquisition parameters used for the ^{1}H spectra were: 0 dummy scans, 1 scan, acquisition time 2.3 s, 90° 15 μs pulse, o1p 5 ppm and spectral width 15 ppm.

Chapter 3

Spatially selective NMR

3.1 Introduction

One of the time consuming aspects of NMR experiments is the interscan delay, allowing nuclei to relax back to equilibrium after pulsing. Recent literature[1,41] presented a pulse program that allowed continual pulsing and acquisition via the use of simultaneous gradients and selective pulses, enabling studying of fast reactions. A pulsed field gradient (PFG) effectively tilts B_0, removing the homogeniety of the magnetic field along the axis of the gradient (usually parallel with B_0). If a selective pulse coincides with the PFG it selectively excites spins in different slices of the sample.[29,84] The gradient is then turned off and the data acquired, following acquisition the gradient is applied again and another shaped pulse applied at a different frequency. This frequency shift allows continual pulsing as the previously excited spin is allowed to relax before it is pulsed again.

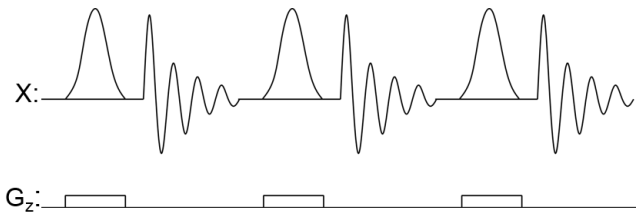

Figure 3.1: Frequency shifted spacially selective excitation pulse program. Where X the nuclei of choice, being pulse by selective 90° pulses and G_z is the gradient channel.

The pulse program can be seen in Figure 3.1. This was written after reading the aforementioned papers.[1,41] The pulse program was implemented, and parameters tested, the results

are discussed in this chapter.

For this slice selective frequency shifted pulse program to have good temporal resolution, the parameters such as gradient strength (**G**) and excitation band width ($\Delta\nu$) need to be optimised for the relaxation of the species being observed. The thickness of the slice (Δz), shown in Equation 3.1, is directly related to both these parameters, and the number of slices used will dictate the time until the same slice is pulsed on again.

$$\Delta z = \Delta\nu / \frac{\gamma}{2\pi} G \tag{3.1}$$

The position of the excited slice in the NMR tube can be calculated using Equation 3.2. Where Ω is the Larmor frequency of the spin in the absence of PFG and ν_i is the frequency shift applied to the pulse.

$$z = (\Omega - \nu_i) / \frac{\gamma}{2\pi} G \tag{3.2}$$

The spectral window (SW_G), covered by the applied gradient is shown in Equation 3.3, this allows confirmation that the applied gradient will allow visualisation of all spins. Here L represents the length of the coil in cm.

$$SW_G = \frac{\gamma}{2\pi} LG \tag{3.3}$$

All values should be in cm, Hz, Gauss or a combination of these units.

3.2 Results

Initially tests were performed to test the effects of both gradient strength and selective pulses. The observed effects were compared to the parameters calculated using Equations 3.1 - 3.3.

3.2.1 Gradient strength effects

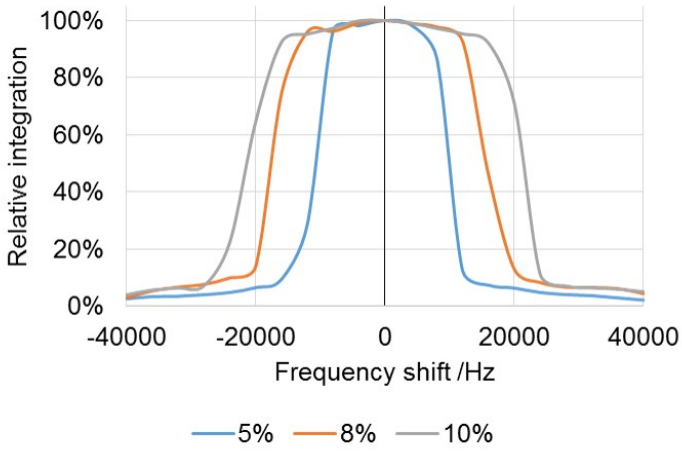

Figure 3.2: Comparison of the results of different gradient strengths on the frequency shifted spatially selective excitation (Pulse program of Figure 3.1)

As can be seen in Figure 3.2 strengthening the gradient broadens the range of frequency shifts. At the same time the S/N is reduced, as expected due to the decrease in effective volume (data not shown). The frequency shifts used allowed calculation of the coil length (1.6 cm) in the probe used, as no signal is observed when the frequencies extend past the coil length.

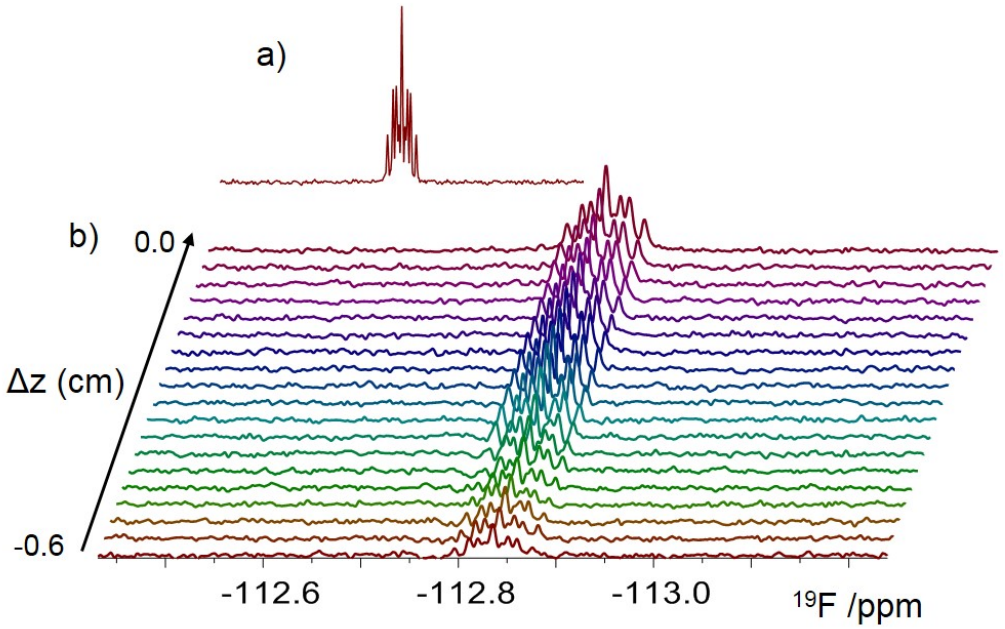

Figure 3.3: ^{19}F spectra of fluorobenzene. Where (a) shows the ΔZ 0 cm slice during a 10% gradient (S/N 181.42) and (b) shows stacked spectra of ΔZ -0.6 to 0 cm during a 40% gradient (S/N 64.49). The only difference between (a) and (b) are the gradient strengths.

During stronger gradients, shown in Figure 3.3, the S/N is reduced. This can be problematic during reaction monitoring, especially when unknown intermediates may be short-lived dilute species.

3.2.2 Performance of different selective pulses

Next a comparison of different excitation pulses was done to see how they perform in slice selective excitation. To test this three pulses were used: Gaussian270, Eburp and Esnob.

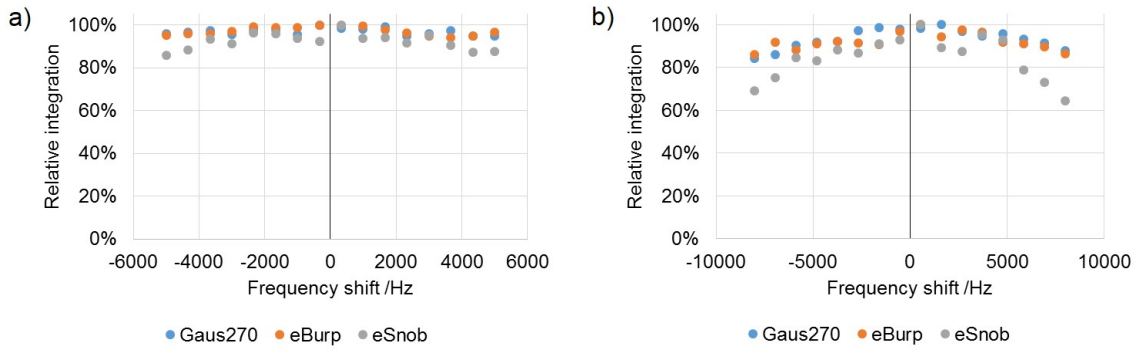

Figure 3.4: Performance of different pulses in slice selective excitation on (a) ^{1}H and (b) ^{19}F spectra

As can be seen in Figure 3.4, there are differences in how each selective pulse performed. These differences are exaggerated in the ^{19}F spectra, due to the larger spectral width. Surprisingly, Esnob, which is in the middle of the three pulses in terms of how flat top (i.e. similar to hard pulses) it is, performed worse. Eburp was therefore used in all future experiments to allow the most uniform excitation of the sample.

3.2.3 Frequency shifting methods

The next aspect tested was the method of frequency shifting. There are three possible choices, using: shaped pulse offsets (SPOFFS), a frequency list or a shaped pulse list. Whereby SPOFFS is implemented by performing multiple 1D spectra and specifying the frequency shift/offset using the parameter SPOFFS, a frequency list specifies which frequencies to pulse at, and a shaped pulse list specifies the pulse type, length, power and the frequency at which it is applied. Each of these were coded and the results analysed the three different pulse programs and lists are presented in Chapter 7. Initially SPOFFS and a frequency list were compared as they are most similar.

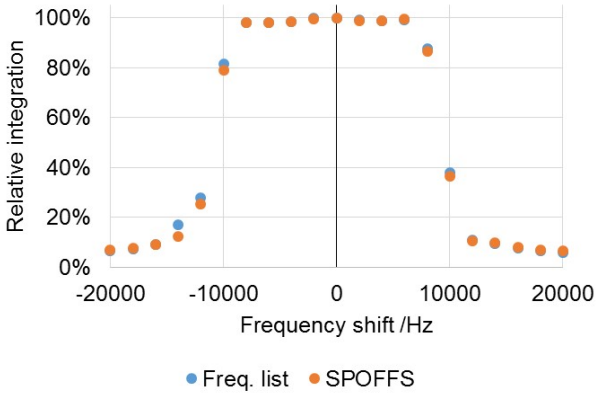

Figure 3.5: SPOFFS vs. frequency list. A comparison of the integrals of ^{19}F TFT signal as a function of the frequency shift.

As can be seen in Figure 3.5 there is *virtually* no differences between the two methods of frequency shifting for this pulse program. The next comparison was done between the two list methods: frequency lists vs. shaped pulse lists.

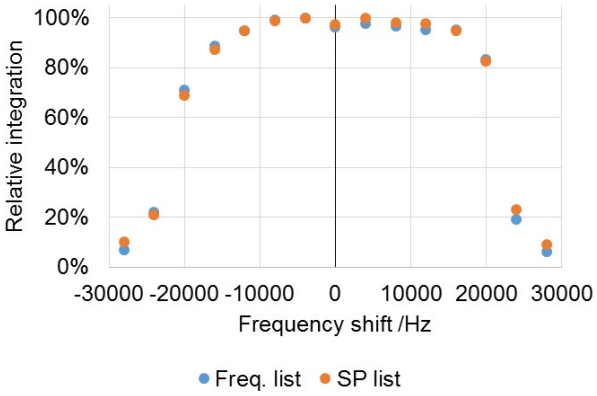

Figure 3.6: Frequency list vs. shaped pulse list. A comparison of the integrals of ^{19}F F-3 signal of 2,3,6-difluoropheyl boronic acid as a function of the frequency shift.

Yet again, the two methods of frequency shifting give almost identical results, as can be seen in Figure 3.6, with the shaped pulse list providing slightly more uniform values.

3.2.4 Biphasic NMR

Initially the slice selective excitation was developed to allow rapid pulsing without the need to wait for nuclei to relax. However, this method also allows spatially selective data to be acquired. To illustrate this a biphasic sample was prepared, sample shown in Figure 3.8.

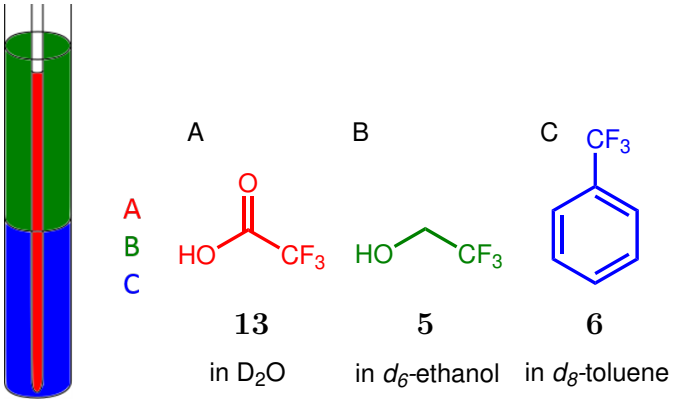

Figure 3.7: Schematic showing the biphasic sample used for slice selective excitation shown in Figure 3.8

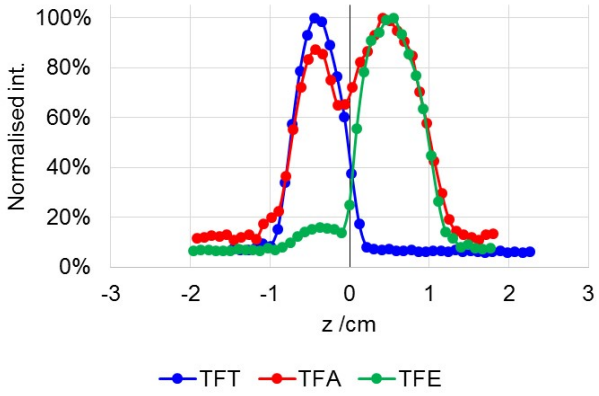

Figure 3.8: ^{19}F frequency shifted spatially selective spectra of a biphasic sample with a capillary insert, shown in Figure 3.7

The biphasic sample shows several things. Firstly, the two layers can be seen separately, which is fundamentally what this experiment set out to do. Secondly, **5** diffuses into the toluene layer. Finally, the integrals of **13** at the phase boundary are not reliable, this is due to the solvents having different magnetic susceptibility which leads to large magnetic field inhomogeneities. The coil is not tuned properly and therefore the pulses are "miscalibrated".

3.3 Conclusions

The spatially selective frequency shifted pulse program works in the way described in the paper.[1] The parameters have been tested and the pulse program works best with Eburp pulses; frequency shift methods have no impact and gradients perform as expected. Stronger gradients effectively tilt the magnetic field more strongly, separating the frequencies out more. However, the stronger the gradient used, the worse the S/N.

^{19}F tags on molecules are commonly used for reaction monitoring. To improve signal-to-noise ^{1}H decoupling would help a lot, however, the probe our spectrometer is equipped with has both proton and fluorine on the same coil (common in modern probes). To overcome this S/N issue, a pulse program was developed, discussed in Chapter 4, and the slice selective version of this pulse program in Chapter 5.

3.4 Experimental

All data, unless specified, were acquired using a two-channel 400 MHz Bruker Avance III NMR spectrometer equipped with a Prodigy probe at 300 K.

The data shown in Figure 3.2 were acquired using the pulse sequence of Figure 3.1 using a sample of trifluorotoluene (**6**) in d-Toluene with the following paramters: 2 dummy scans, 1 scan, 1.5 s acquisition time, o1p of -60.5 ppm, spectral width of 80 ppm, 90° 10 ms Eburp pulse, frequency shift of ± 32,000 Hz, with a gradient of variable strengths (5, 8 and 10%).

The ^{19}F spectra shown in Figure 3.3 are of fluorobenzene (**4**) in $CDCl_3$. The spectra were acquired with 0 dummy scans, 2 scans, o1p of -112 ppm, spectral width of 30 ppm, 90° 9 ms eBurp pulse, frequency shift of ± 10,000 Hz, with a sine gradient of 10%.

The data shown in Figure 3.4 shows the effects of different pulse types on a sample of **7** in d_4-MeOH. For both ^{1}H and ^{19}F the pulses were calibrated to have an excitation bandwidth of 200 Hz, this resulted in the following pulse lengths: 8.74 ms Gaussian270, 24.76 ms Eburp, 9.61 ms Esnob. The ^{19}F spectra were acquired using 2 dummy scans, 4 scans, 1.5 s acquisition time, o1p of -76.85 ppm, spectral width of 120.7 ppm, frequency shift of ± 8000 Hz and a 5% sine shaped gradient. The ^{1}H spectra were acquired using 0 dummy scans, 1 scan, 1.5 s acquisition time, o1p of 7.29 ppm, spectral width of 7 ppm, frequency shift of ±

5000 Hz and a 5% sine gradient.

The data shown in Figure 3.5 shows the differences in integrals when using SPOFFS (shaped pulse offset, where you can modify the frequency of the shaped pulse relative to the center of the spectrum) or a frequency list, analysing the ^{19}F signal of TFT (**6**) in d-Toluene. The acquisition parameters used were 2 dummy scans, 1 scan, 1.5 s acquisition time, o1p of -60.5 ppm, spectral width of 80 ppm, 90° 10 ms Eburp pulse, frequency list of ± 32000 Hz, with a sine shaped gradient of 5%.

The data shown in Figure 3.6 shows the differences in integrals when using a frequency list or a shaped pulse list, analysing the ^{19}F signal of TFT (**6**) in d_8-Toluene. The acquisition parameters used were 0 dummy scans, 4 scans, 1.5 s acquisition time, o1p of -60.5 ppm, spectral width of 80 ppm, 90° 10 ms Eburp pulse, frequency list of ± 28000 Hz, with a sine shaped gradient of 10%.

The data shown in Figure 3.8 shows the integrals from the spatially selective biphasic sample. The sample consists of TFT (**6**) in toluene, with a layer of TFE (**5**) in ethanol, with a capillary of TFA (**13**) in D_2O. The acquisition parameters used were 2 dummy scans, 1 scan, 1.5 s acquisition time, o1p of -70 ppm, spectral width of 80 ppm, 90° 10 ms Eburp pulse, frequency list of ± 20000 Hz, with a sine shaped gradient of 5%.

Chapter 4

$SHARPER^2$

Sensitive, Homogeneous, And Resolved PEaks in Real time

4.1 Introduction

A new "pure-shift" method, termed "SHARPER" (**S**ensitive, **H**omogeneous **A**nd **R**esolved **PE**aks in **R**eal time) is designed for the analysis of reaction and equilibria kinetics using NMR. SHARPER focuses on one signal, selectively exciting it, and refocusing all couplings using a chain of selective spin echoes during acquisition. It does not require pulsing on X channels to achieve heteronuclear decoupling, overcoming the hardware limitations of conventional spectrometers - i.e. ^{1}H and ^{19}F being on the same channel.

The simplest form of SHARPER works by pulsing non-selectively, and removing all heteronuclear couplings using non-selective 180° pulse during acquisition. This is only possible when a single X spin (e.g. ^{19}F or ^{31}P) is in the molecule/system. A more versatile decoupling scheme, called "sel-SHARPER", works via a non-selective 90° pulse and a selective 180° pulse flanked by gradient pulses (SPFGSE), and selective 180° pulses during the acquisition, removing all hetero- and homonuclear couplings. The 180° pulses during acquisition not only refocus the couplings, they also compensate for both pulse imperfections and magnetic field inhomogeneity giving narrow singlets. The line narrowing effects combined with the decoupling allows for increased signal-to-noise, twenty-fold increases were routinely achieved for ^{19}F detection. The sensitivity gains are most substantial for inhomogeneous

magnetic fields, including inhomogeneity caused by gas sparging. Parameters of the pulse program have been tested to develop guidelines for their optimal application, and have been tested on several different systems.

Considerable reduction in the detection threshold induced by (sel)-SHARPER, make the technique particularly suited for *in situ* monitoring of reaction kinetics. The approach is illustrated by ^{19}F-NMR studies of the protodeboronation of aryl boronic acids. Here, the high S/N allowed reliable determination of the protodeboronation kinetics, whilst the excess line-broadening of ^{19}F singlets were used to characterize the boronic acid/ boronate equilibrium kinetics.

Oxidation of diphenylphosphine, monitored by ^{31}P NMR under optimized gas-flow conditions, demonstrated high tolerance of SHARPER to gas-sparging. The principles of the (sel)-SHARPER sequences are expected to find numerous applications in design of new NMR experiments.

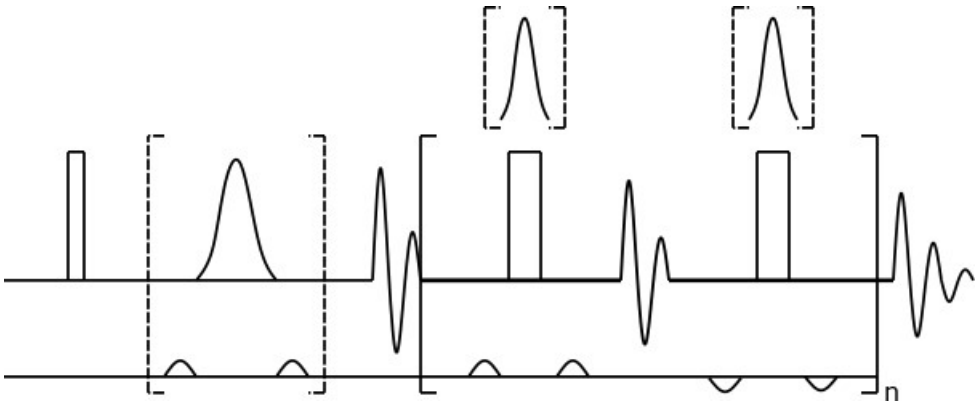

Figure 4.1: SHARPER pulse program - where dashed lines indicate additional options in the pulse program. Option SPFGSE uses selective 180° pulses for both initial signal selection and during acquisition. Full pulse program can be seen in Chapter 7.

SHARPER works by manipulating spin systems during the acquisition period of the NMR experiment, as can be seen in Figure 4.1. Band-selective pure-shift approaches generally maintain all available magnetisation, increasing signal-to-noise, for only a subset/single signal. This is of importance for reaction monitoring, where maximising sensitivity is highly beneficial.

4.2 Results and Discussion

Alternative Pure-Shift Arrangements

The radio-frequency carrier is placed on the chemical shift of a selected signal, which eliminates chemical shift evolution, producing an exponentially decaying FID. Under these conditions, 180° pulses can be repeatedly applied to the active spin to refocus couplings. The effective 0°/180° rotation of the detected/coupled spins, which is at the heart of broadband decoupling of selected signals during indirect or direct acquisition periods, can thus be replaced with a 180°/0° element, maintaining all the attributes of a pure shift methodology while realising additional benefits.

In its simplest form, the described pure-shift real-time experiment removes all heteronuclear couplings of an isolated nucleus. The pulse program, shown in Figure 4.2, consists of a 90° pulse, followed by an acquisition interrupted by a periodic application of a hard 180° pulses, flanked by low-level PFGs. Part of the repeating unit consists of two such events, where the two pairs of PFGs are of equal strength, but opposite polarity, which minimises the disturbance of the static magnetic field and lock circuitry.

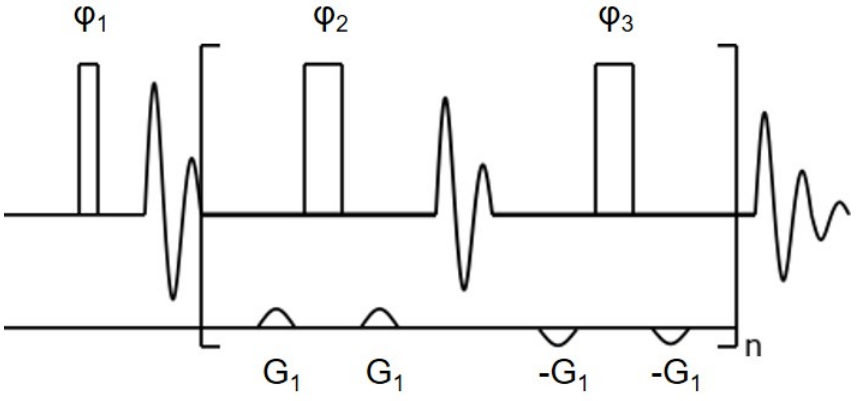

Figure 4.2: SHARPER pulse sequence. Narrow and wide rectangles represent 90° and 180° pulses, respectively. 300 μs sine-shaped PFGs were applied using G_1 of 1% followed by a 200 μs gradient recovery delay. Where Psi_1 is x, Psi_2 is y and Psi_3 is -y.

By maintaining a 90° phase difference between the initial 90° excitation pulse and the subsequent 180° pulses, this experiment possesses all the attributes of the CPMG pulse sequence, compensating for the static magnetic field inhomogeneity and pulse imperfections.

These properties have historically been used by Freeman and Hill,[85] for recording proton

"J-spectra". Such spectra showed extremely narrow linewidths, reflecting the true T_2 relaxation of protons. Freeman and Hill's experiment acquired signal only at the peaks of individual spin-echoes, where the effects of the magnetic field inhomogeneity are completely removed.[85] In a different context, a spin-echo applied during an indirectly detected dimension of heterocorrelated experiments has been shown by Gochin et al[86] to remove signal broadening due to magnetic field inhomogeneity. Remarkably, as illustrated below, a significant line-narrowing is maintained while relaxing the conditions applied for *J*-spectra to allow acquisition of signal in "chunks" of tens of milliseconds long, in the technique SHARPER.

Single Channel Heteronuclear Decoupling

The basic version of SHARPER, Figure 4.2, removes all heteronuclear splittings, effectively performing heteronuclear decoupling without the need to pulse on X nuclei. This can be highly beneficial, especially for fluorinated compounds, as modern NMR spectrometers often have ^{1}H and ^{19}F on the same channel - not allowing simultaneous pulsing on both nuclei. Another benefit of SHARPER, as its decoupling is achieved by pulsing on the observed nucleus, is that it removes all heteronuclear coupling, e.g. ^{19}F in a partially-deuterated compound, both the ^{1}H- and ^{2}H-couplings are removed, revealing the ^{19}F$\{^{1}$H,^{2}H$\}$ signal for the nucleus of interest. To illustrate the performance of the basic SHARPER pulse sequence, a ^{19}F SHARPER spectrum of fluorobenzene, is presented in Figure 4.3. It is overlaid with a ^{1}H-coupled ^{19}F spectrum of FB (**4**) containing a single ^{19}F resonance as a triplet of triplets (9.1 and 5.8 Hz) due to the splitting by pairs of chemically equivalent ortho- and meta-protons.

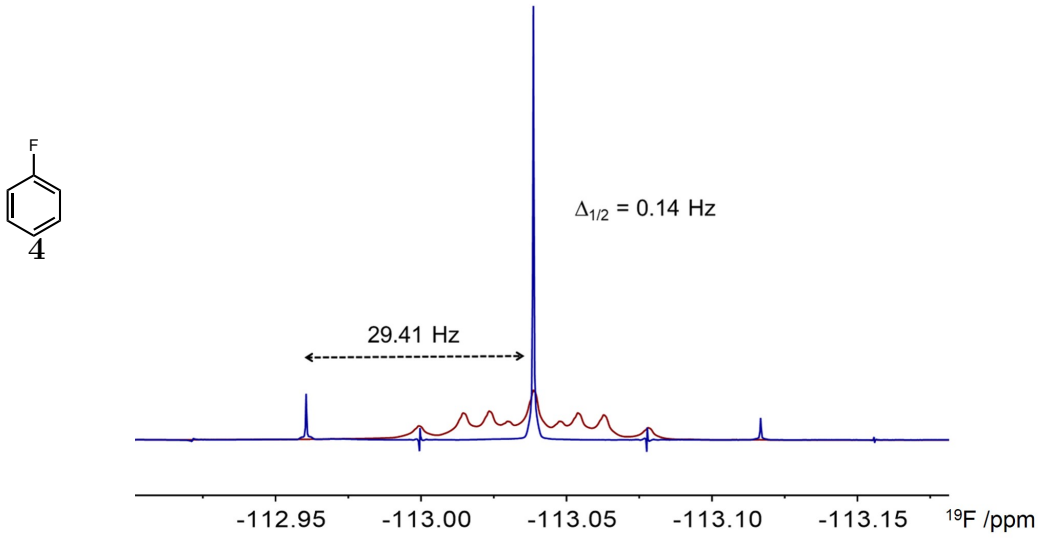

Figure 4.3: ^{19}F SHARPER NMR spectrum of **4**, acquired using the pulse sequence of Figure 4.2 with a 34 ms chunk time, overlaid with a ^{1}H-coupled ^{19}F spectrum of fluorobenzene. The position of the first side bands at 1000/34 = 29.41 Hz is indicated.

The ^{19}F-SHARPER spectrum of **4** contains an extremely narrow singlet (half-height linewidth, $\Delta_{\frac{1}{2}} = 0.14$ Hz) that has 8-fold the S/N of the central line of the ^{1}H-coupled ^{19}F multiplet. In this example, a deliberately long chunk time of 34 ms was chosen to illustrate the robustness of the method. The odd-numbered chunking artefacts at k/(2 x chunk time) (k=1, 3, 5 ...) frequencies are largely suppressed by acquiring an initial half-chunk, while the sidebands at k/(1 x chunk time) decay rapidly with increasing k. A systematic exploration of the effects of the chunk length on the SHARPER spectra is presented later in this chapter.

Hetero and Homonuclear Decoupling

Modifications of the basic pulse sequence (Figure 4.4) allow it to be used with systems that have multiple signals, removing both hetero- and homonuclear couplings. The first modification involves an additional selective 180° pulse with two flanking PFGs, giving the signal of interest 270° pulse, whilst all other signals are destroyed by the PFGs. The second modification is the use of selective pulses during the acquisition instead of non-selective 180° pulses. This can take the form of a carefully adjusted 180° rectangular pulse, positioning signals of coupled spins in-between the lobes of its sinc inversion profile, or an arbitrary refocusing selective shaped pulse. Both approaches are collectively referred to as selective

SHARPER or sel-SHARPER (Figure 4.4).

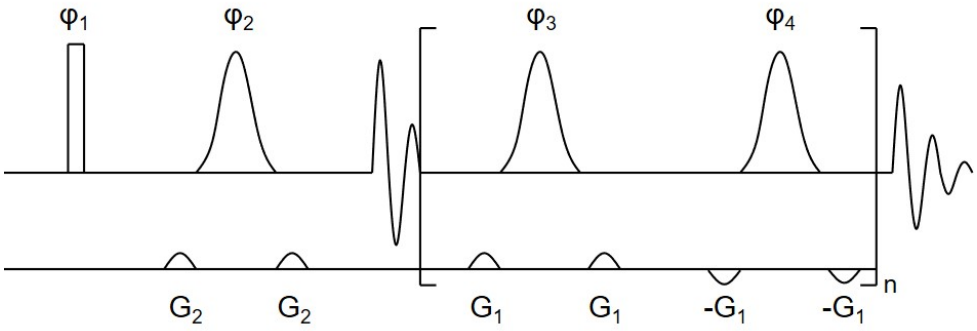

Figure 4.4: Pulse sequence of the sel-SHARPER experiment. The narrow rectangle represents a 90° non-selective pulse, while open Gaussian shapes represent selective 180° pulses. 300 μs sine-shaped PFGs were applied using G_1 of 1% or a G_2 of 30%, followed by a 200 μs gradient recovery delay.

The benefits of sel-SHARPER are illustrated below through the KOH catalyzed protodeboronation of fluorinated aryl boronic acids, via the corresponding boronates. Protodeboronation of 2,3,6-trifluorophenyl boronic acid (**7**), via the boronate, in a 1:1 mixture of deuterated methanol and H_2O, yields 1,2,4-trifluorobenzene (**8**), and its isotopologue 3-[^{2}H]-1,2,4-trifluorobenzene (**14**), (Figure 4.5a). After complete consumption of the boronic acid, the ^{19}F spectrum of the resulting mixture shows six ^{19}F signals, split by numerous ^{19}F-^{19}F, ^{1}H-^{19}F and ^{2}H-^{19}F couplings. These complex ^{19}F multiplets are up to 50 Hz wide, with corresponding ^{19}F resonances separated by ^{1}H/^{2}H-isotope shifts for the two products. Coupling constants are given in Table 4.1.

Table 4.1: Coupling constants in Hz of Compound 1,2,4-trifluoro(-3-deutero)phenyl

Compound		F-1	F-2	F-4	H/D-3	H-5	H-6
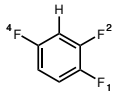	F-1	-	3.2	20.5	10.9	2.0	9.1
	F-2	3.2	-	15.3	8.5	8.0	5.1
	F-4	20.5	15.3	-	6.4	10.3	3.3
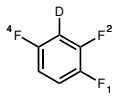	F-1	-	3.3	20.5	1.6	2.0	9.0
	F-2	3.3	-	15.3	1.3	8.0	5.1
	F-4	20.5	15.3	-	0.9	10.2	3.3

Focusing on the signal F-1 of 1,2,4-trifluoro-3-deutero-phenyl (**14**) a ^{1}H, ^{2}H-coupled ^{19}F spectrum (Figure 4.5a) and two ^{19}F sel-SHARPER spectra (Figure 4.5b and c) are compared. The two sel-SHARPER spectra were acquired using a 10 ms sinc pulse during the initial single pulse field gradient spin echo (SPFGSE) selecting the signal of F-1, while

205 μs 180° rectangular (Figure 4.5b) or 10 ms Gaussian pulses (Figure 4.5c) were applied during the acquisition respectively. The length of the rectangular pulses were adjusted to position the F-3 and F-4 resonances of **14** between the lobes of their sinc inversion profile, in order not to change the spin states of these nuclei. In both instances, the collapse of the F-1 multiplet in the sel-SHARPER spectra delivers significant sensitivity gains: the S/N is 20-fold greater than in the ^{1}H, ^{2}H-coupled ^{19}F spectrum. The signal loss due to real-time decoupling is small, with 82 and 73%, respectively, of the integral intensities preserved in the two sel-SHARPER spectra relative to the reference 1D spectrum. This is mainly because the actual acquisition time has almost doubled from the nominal value of 3.49 s to 6.30 s, in this instance, while only a modest increase to 3.79 s accompanied the use of rectangular pulses. In both cases the signals have not yet decayed to zero intensity. The small increase in the linewidths, from $\Delta_{\frac{1}{2}}$ of 0.24 to 0.31 Hz, is thus caused by the additional relaxation during the longer Gaussian pulses.

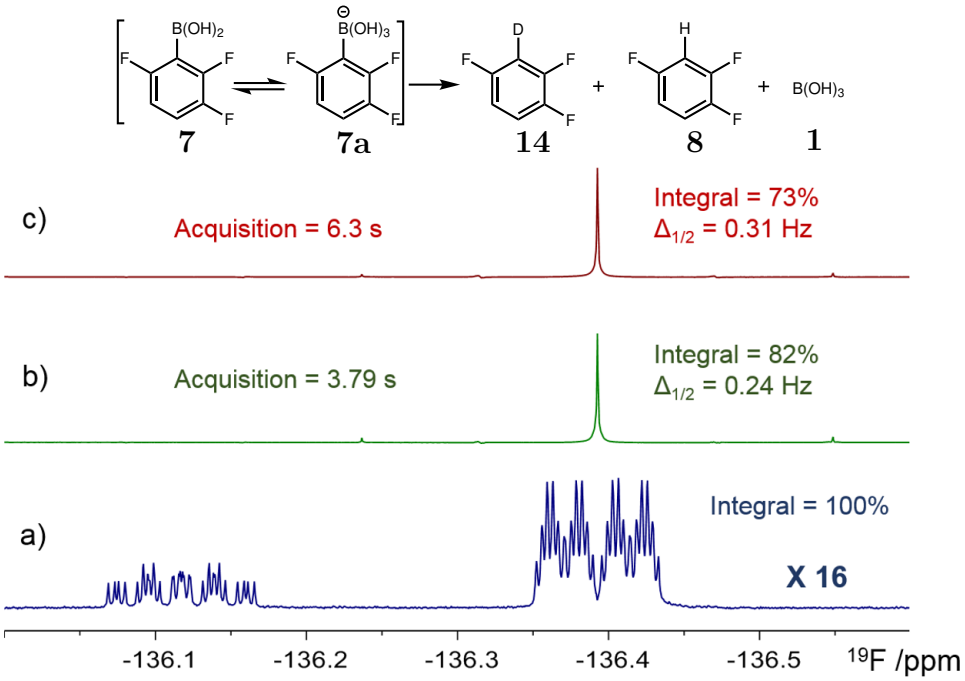

Figure 4.5: Partial ^{19}F spectra focusing on F-1 resonances in a mixture of products **8** (δ -136.12) and **14** (δ -136.39) obtained by KOH-catalyzed protodeboronation of **7** in CD_3OD / H_2O. (a) ^{1}H-coupled ^{19}F spectrum (scaled up 16 times) (b) and (c) sel-SHARPER spectra of **14** acquired using the pulse sequence of Figure 4.4, a 205 μs 180° rectangular (b) or 10 ms Gaussian pulses (c) during the acquisition. Both $\Delta_{\frac{1}{2}}$ and integral intensities relative to that of F-1 in (a) are given.

Line-narrowing Properties of SHARPER

Magnetic field inhomogeneity can be detrimental to NMR spectra, and it is not always possible to achieve and/or maintain. Examples include monitoring slow reactions in non-deuterated solvents without autoshim, reactions taking place in multiphase environments, or reactions which require or induce agitation, e.g. for phase transfer, or gas-generation as a reaction evolves.

As SHARPER utilises CPMG properties it is able to compensate for such field inhomogeneities. To test this property, the shim corrections were miss-set by 500 units and a mixture of 1,2,4-trifluorophenyl **8** and 1,2,4-trifluoro-3-deutero-phenyl **14** were reacquired using otherwise identical experimental parameters. The results are presented in Figure 4.6. The intensities of the main signal F-1 of 1,2,4-trifluoro-3-deutero-phenyl **14** dropped by 18% with an increase in line-width of less than 0.04Hz.

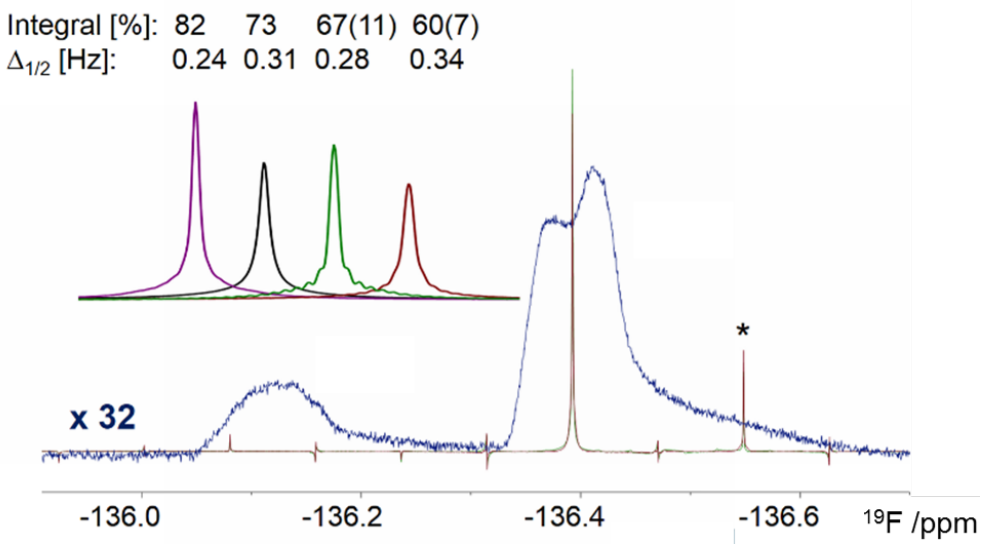

Figure 4.6: Overlay of ^{19}F spectra of **8** as presented in the Figure 4.5, but acquired in an inhomogeneous magnetic field with x, y, z, z^2, z^3, xy, xz and yz shim corrections miss set by +500 units from their optimal values. The ^{1}H-coupled ^{19}F spectrum (blue, scaled up 32 times) and sel-SHARPER spectra using rectangular (green) and Gaussian (red) inversion pulses. The inset shows, left to right, the F-1 signals from spectra of Figure 4.5b (violet) and Figure 4.5c (black), and the two corresponding signals acquired under miss-shimmed conditions. Signal attributes ($\Delta_{\frac{1}{2}}$ and integral intensities) are given relative to those presented in Figure 4.5. The values in parenthesis belong to the sidebands.

The missing integral from the SHARPER singlet is directed into the first side-band at the frequency where a fraction of the spins resonate. The implication is that shorter chunk

times better compensation of magnetic field inhomogeneity will be achieved; this approach is illustrated in Figure 4.7. Upon closer inspection of spectra shown in Figure 4.7 it can be seen that the sum of the integrals of the main peak and sidebands remain almost constant, therefore inclusion of the sidebands during quanititation is advisable if a reduced chunk time is not desired.

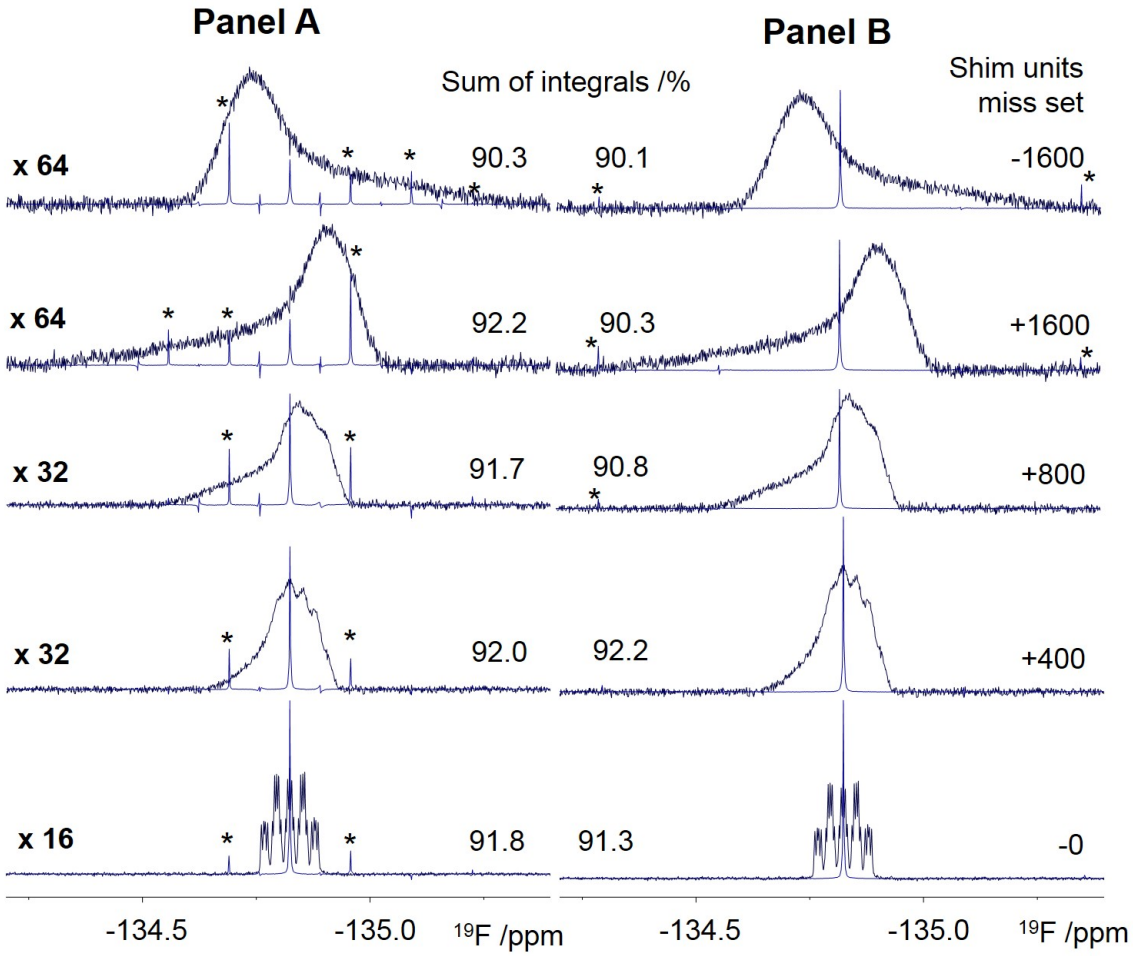

Figure 4.7: Effects of magnetic field inhomogeneity on SHARPER spectra. Overlay of 1D and sel-SHARPER ^{19}F spectra of **8**. Panel A and B present spectra acquired using the pulse sequence of Figure 4.4 with n=55 (chunk time of 19.86 ms) and n=218 (chunk time of 5.01 ms), respectively. The 1D ^{19}F spectra were scaled up by the factors given on the left. The sums of integrals of the central signal and sidebands (labelled with asterisks), are given in the middle for each sel-SHARPER spectrum (relative to that of a well shimmed 1D spectrum). The degree of miss shimming of the x, y, z, z^2 and z^3 shims is indicated on the right.

Gas-sparging

As an example of the ability of SHARPER to compensate for "dynamic" magnetic field inhomogeneity, SHARPER spectra of **4** were recorded while nitrogen was bubbled through the solution (Figure 4.8).

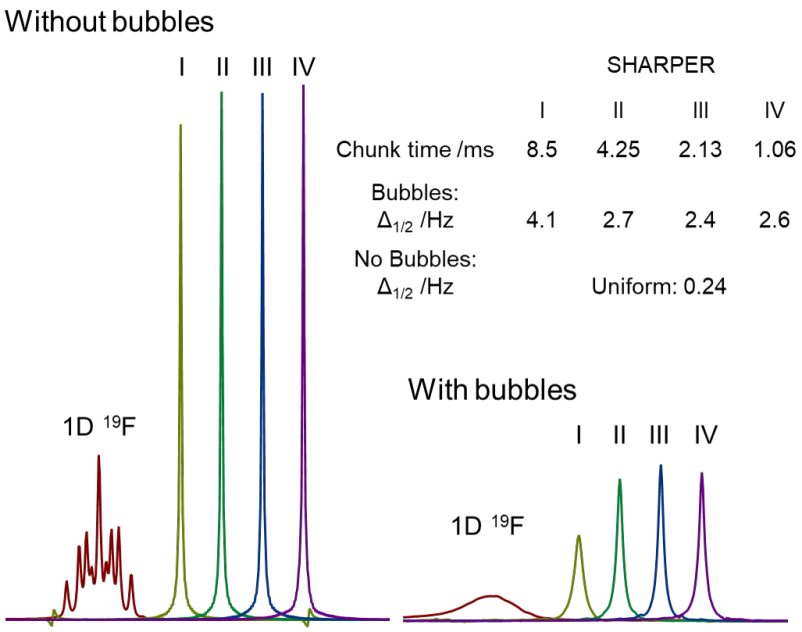

Figure 4.8: ^{19}F SHARPER spectra without (left) and with N_2 sparging (right) plotted on an identical vertical scale. ^{1}H-coupled ^{19}F 1D spectra of **4** obtained under these conditions are also shown. The signal half widths are stated as a function of the chunk time.

Shorter chunk times (i.e. shorter spin-echoes) are better able to restore line shape than longer ones - this is due to the fact that the time scale of the magnetic field fluctuation, e.g. caused by bubbling, must not be faster than spin-echoes. If this magnetic field fluctuation is faster than the spin echoes it cannot be compensated for. The singlets of **4** during gas-sparging produced by SHARPER are ten times wider than without gas sparging, however this is still ~8 fold increase in S/N compared to the 1D ^{19}F spectrum acquired under the same conditions. After testing SHARPER during gas-sparging the following step was to test kinetics that required gas-sparing. To test this, air was bubbled through a sample of **15** acid in unstabilised THF, the results of which can be seen in Figure 4.9. As can be seen the exponential decay is clearly visible, but the data shows considerable scatter, with two parallel exponentials, corresponding to varying volumes of bubbles within the r.f. coil space.

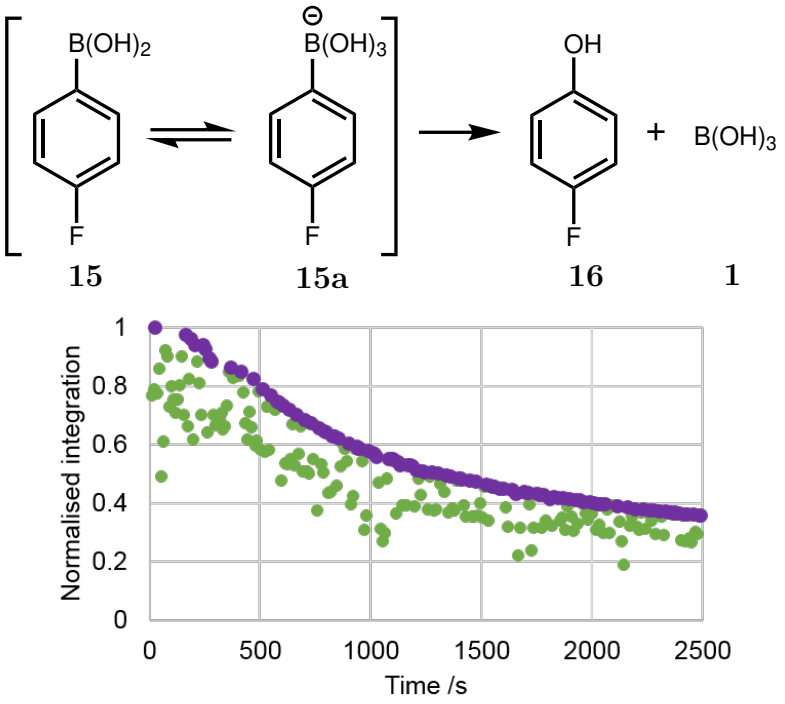

Figure 4.9: The effect of the bubbling rate on the reproducibility of signal integrals whilst monitoring the reaction of 4-fluorophenyl boronic acid with oxygen using SHARPER under slow bubbling of air.

Using a slower bubbling rate allowed us to obtain narrower linewidths (Figure 4.9), however the integrals were not uniform as seen above. To allow monitoring of reactions under gas sparging, further tests were performed, depicted in Figure 4.10, to allow optimal bubbling conditions to be found. A flow rate of 180 ml/hour allowed the integrals became substantially more stable.

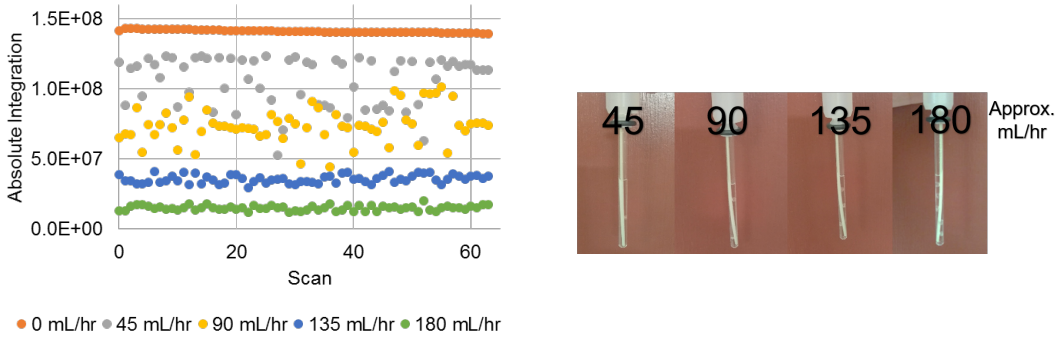

Figure 4.10: The effect of the bubbling rate on the reproducibility of signal integrals. Corresponding time course of integral intensities. Snapshots of videos showing the density of bubbles, and approximate flow rates.

At lower bubbling rates, the rationale for the observed inconisitent integrals is that, either

one or no bubbles are present at any given time in the active volume of the coil. At higher rates they become consistent as there are two bubbles always present. Even though this leads to loss of signal, whilst monitoring reactions, consistency of integrals in important. It should be noted that if one signal needs to be selected during the initial SPFGSE of the sel-SHARPPER (Figure 4.4), the duration of the selective pulse, and the strength and duration of PFGs should all be kept to a minimum, otherwise the SPFGSE becomes a source of significant signal losses and intensity variations due to intense convection and subsequent incomplete refocusing of magnetisation during SPFGSE.

As discussed, the relationship between chunk time and experimental conditions, affect the quality of SHARPER spectra. The effects of chunk length on SHARPER spectra were systematically explored, as well as frequency mismatch and pulse miss-calibration. These will be discussed in detail in this chapter.

The Factors Affecting SHARPER Spectra

The optimal settings depend on the nature of the molecule/reaction/mixture being studied, the relaxation properties and the complexity of the spectrum. The most important factors are chunk length, and the method for selective inversion of the active spin (for details see Figure 4.12 and Table 4.1). Short chunk times are generally beneficial, however for couplings of <15 Hz chunk lengths of tens of milliseconds are acceptable, and preferable when using long selective inversion pulses. The long pulses extend the time that spins spend in the transverse plane, increasing the effective spin-spin relaxation, broadening the spectral lines. This is common to all band-selective real-time pure shift methods, however, only SHARPER compensates for magnetic field inhomogeneity through the CPMG scheme. Band-selective methods usually effectively apply a 0° pulse to the active nuclei between acquisition chunks, and hence cannot act in a similar manner. To maximise these benefits, the 180° pulses applied during the acquisition must avoid inversion of the spins coupled to the observed spin. Non-coupled spins can be inverted during acquisition without impacting the outcome as they will have been eliminated via the initial SPFGSE that can be highly selective. This becomes more difficult and important for crowded ^{1}H spectra. During gas evolution, short

chunk times perform better, as the spin-echoes should be shorter than the dynamic inhomogeneity caused by bubble evolution. Some PS techniques reduce the effect of magnetic field inhomogeneity, such as spatially selective pure-shift experiments,[56] however their sensitivity is reduced due to spatial selection.

SHARPER works by sitting on resonance of a signal, which can be problematic in the context of reaction monitoring, as signals can change their resonance frequency, e.g. pH changes, phase separation. The shifting of signals can have a negative consequences for SHARPER. We show in Figure 4.13 that SHARPER can be used for quantitative analysis of reaction kinetics even when signals are moving during monitoring, but it is essential to include sidebands in the data analysis. Short chunk times reduce the "leakage" of signal into sidebands and are required when larger movements of resonances are anticipated. Similarly, as previously discussed, sidebands need to be included for quantitative analysis when magnetic field inhomogeneity is present.

Finally, the effect of pulse accuracy (or excessive B_1 inhomogeneity) on the quality of the SHARPER sequence was investigated (Figure 4.14). The results demonstrate remarkable tolerance of SHARPER to pulse imperfections, pulse calibration to an accuracy of $\pm 10\%$ is recommended to maximize the S/N and the lineshape quality.

To show that SHARPER is not only useful for ^{19}F, but also the more crowded ^{1}H spectra, we show an example using vincamine (Figure 4.11). The aromatic system of vincamine (**17**), is an ABCX spin system, (Figure 4.11b, panel A), and we show the singlet of the X spin using SHARPER. To test the ability of SHARPER we next wanted to excite only one of the H5 signals, which are part of an ABMRX spin system. To achieve this a long (80 ms) selective pulse was needed to not invert proton B (H_{5eq}). This lead to a non-uniform inversion of individual lines of this multiplet, which in combination with fast relaxation of this CH_2 proton decreased the signal intensity; nevertheless, a singlet was produced (Figure 4.11c, panel B).

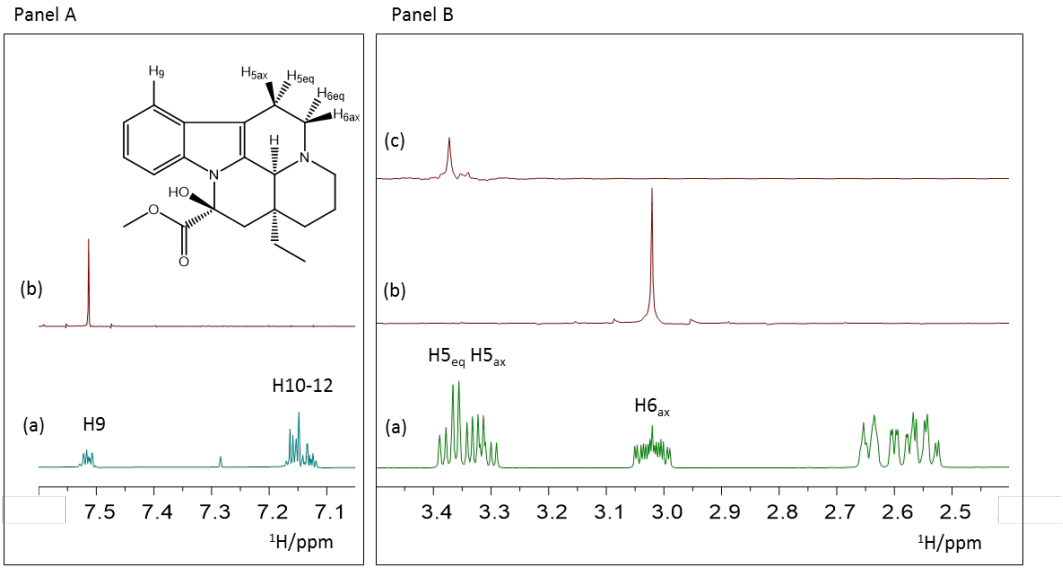

Figure 4.11: ^{1}H sel-SHARPER spectra of vincamine (pulse sequence of Figure 4.4) (a) in Panel A and B shows parts of the ^{1}H spectrum of vincamine. Panel A (b) shows ^{1}H sel-SHARPER spectrum of H_9. Panel B (b) shows ^{1}H sel-SHARPER spectrum of H_{6ax}. Panel B (c) shows ^{1}H sel-SHARPER spectrum of H_{5eq}. Spectra within each panel are drawn using identical vertical scales.

4.2.1 Effects of pulse sequence parameters on the quality of SHARPER spectra

Chunk Length

A series of sel-SHARPER spectra with varied chunk length were obtained for the F-1 signal of 1,2,4-trifluorobenzene (**8**), which in the standard 1D spectrum presents a >50 Hz wide multiplet (2 ^{19}F-^{19}F couplings of 20.5 and 3.2 Hz, and 3 ^{1}H-^{19}F couplings of 10.9, 9.1 and 2.0 Hz). Two sets of spectra were acquired, one using a 250 μs rectangular pulse (Figure 4.12) and the other using 5 ms Gaussian inversion pulses during the acquisition. The chunk lengths varied between 5 and 40 ms. The intensity of the main signal was reduced by a factor of 0.55 when the chunk time was increased from 5 to 40 ms, this was accompanied by increased intensity of sidebands. Whilst the sum the integrals remained practically constant, the $\Delta_{\frac{1}{2}}$ values doubled from 0.15 to 0.30 Hz. When using the Gaussian inversion pulses, the performance of the experiments was similar, except for a 5 ms chunk time, where a broader signal ($\Delta_{\frac{1}{2}} = 0.28$ Hz) was observed due to additional relaxation during the longer Gaussian pulses. A detailed analysis of the spectra is presented Table 4.2.

Table 4.2: Integrals and acquisition parameters for Figure 4.12

Spct.	n	Chunk length /ms	Acquisition time /s	Signal height *	Main signal integral *	Side integrals	Sum of integrals	$\Delta_{\frac{1}{2}}$ /Hz
A	256	5	3.20	100	100	2	102	0.15
B	128	10	2.88	91	98	5	103	0.19
C	64	20	2.71	81	90	13	103	0.25
D	32	40	2.62	55	67	39	106	0.30

* relative to Spectrum A

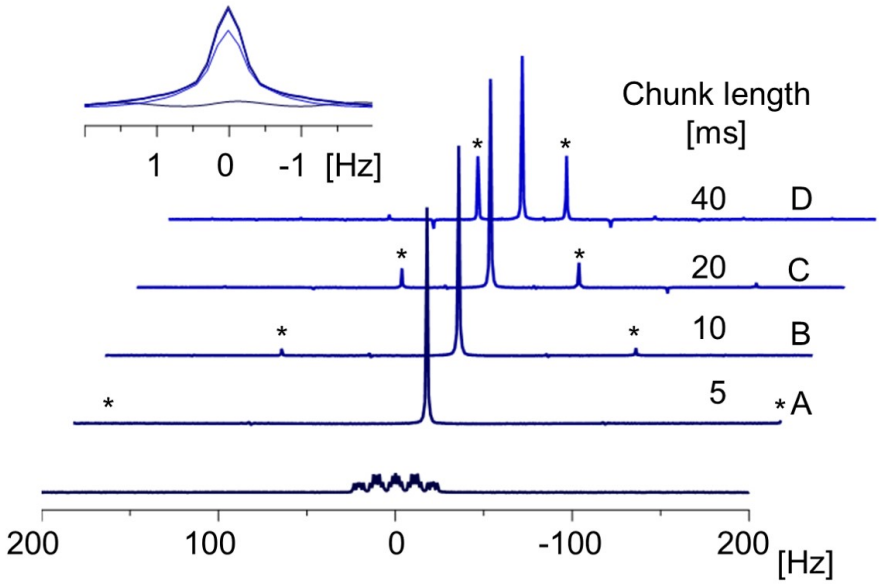

Figure 4.12: Effects of the chunk length on the ^{19}F sel-SHARPER spectra of F-1 of **8**. The bottom spectrum is a reference ^{19}F spectrum. Spectra were acquired using the sel-SHARPER pulse sequence of Figure 4.4. The length of 180° rectangular pulses was set to avoid perturbation of F-3 and F-4 spins. Four acquisition chunk lengths were used (4.992, 9.984, 19,958 and 39.668 ms) producing side-bands at ± 200.32, ± 100.16, ± 50, 08 and ± 25.04 Hz, respectively. The spectra were processed using exponential line broadening of 0.1 Hz; this value was subtracted from the reported line widths. Table 4.2 shows the parameters of spectral lines.

In conclusion, relatively long chunk times can therefore be used even in the presence of large coupling constants. When longer selective pulses are required, additional line broadening occurs, with spins affected more by the relaxation during these pulses. A compromise between selectivity and chunk time is therefore required to avoid excessive signal broadening.

Frequency mismatch

As mentioned previously, during reaction monitoring signals can shift, so testing the effects of mismatch between the carrier frequency and the resonance frequency is required. To test this, three series of sel-SHARPER spectra of the F-1 signal of **8** were acquired using rectangular 180° pulses during acquisition and varying the chunk time (5, 10 and 20 ms). The carrier frequency was decreased relative to the chemical shift of F-1 in steps of 10 Hz up to a final value of -100 Hz. This resulted in a gradual decrease of the height and the integral intensity of the main signal, accompanied by increased intensity of sidebands (Figure 4.13). Some line-shape deterioration was observed at the foot of the signal.

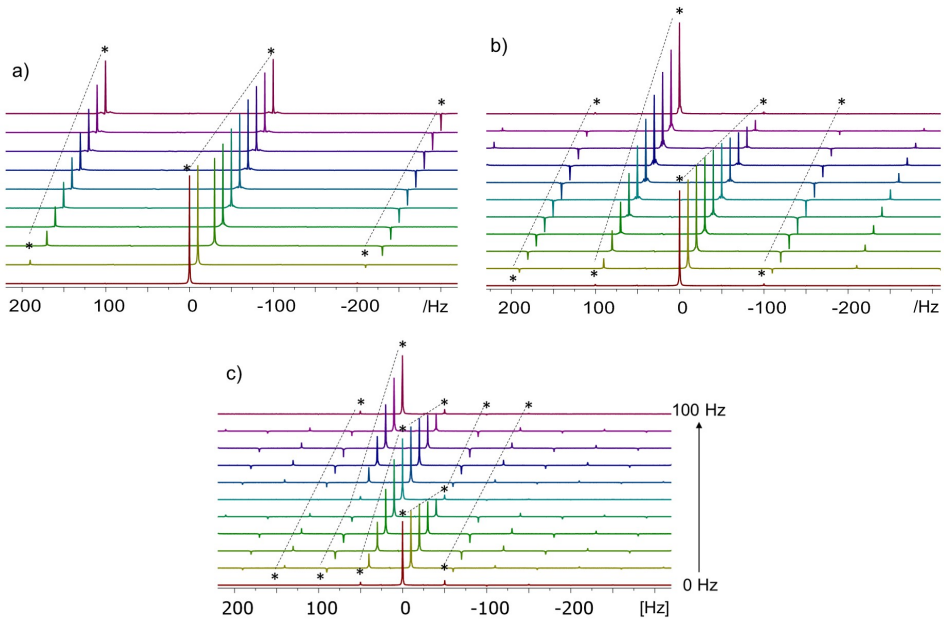

Figure 4.13: Effects of the mismatch between the r.f. carrier and the resonance offset on the SHARPER spectra. Eleven spectra showing the F-1 signal of 1,2,4-trifluorophenyl (**8**) obtained with an increasing carrier offset relative to its chemical shift in steps of -10 Hz up to -100 Hz. (a) to (c) show spectra for chunk times of 5, 10 and 20 ms, respectively, with sidebands at 200, 100 and 50 Hz. Dashed lines indicate the signals in each spectrum which were summed up to give the integral intensities listed next to the spectra (relative to the sum for the on-resonance spectrum in each experiment). Note that when the carrier displacement reaches a multiple of the sideband frequency, the sideband signals move to the left by the amount of the sideband frequency (e.g. for the carrier offset of -100 Hz in (b) and -50 and -100 Hz in (c)).

Reduction in the main signal intensity was least severe with shorter chunk times. For example, when the carrier frequency was offset by -20 Hz, 98.6, 94.1 and 79.6% of the integral intensity remained within the main signal for 5, 10 and 20 ms chunk times, respectively.

Within the constraints we explored, the sum of the main signal and side bands remained relatively constant, with standard deviations of <5% (Figure 4.13). It can therefore be concluded that that SHARPER can be used for quantitative analysis of reaction kinetics when signals deviate from their original resonance during monitoring, but sidebands must be included in the data analysis. Shorter chunk times again are beneficial, as they reduce signal leakage into sidebands, and are required when larger shifts are anticipated.

Pulse miscalibration

Pulse accuracy affects all NMR spectra, and we wanted to test how SHARPER dealt with inaccurate pulse calibrations. As a reference, a ^{19}F SHARPER spectrum of fluorobenzene was acquired using 10 ms chunk times, an accurate 63 μs 180° rectangular ^{19}F pulse applied 512 times during a 5.65 s acquisition time. Spectra were then acquired when the 180° pulses were miss-set by ± 10, 20 and 30%. The results are presented in Figure 4.14 and can be summarised as follows: pulse miss-setting causes (i) a modest decrease in the signal intensity (20% for ±30% miss set pulses in this case) and (ii) a broadening of the base of the signal due to scaled down modulation by ^{1}H-^{19}F couplings of a fraction of spins. Importantly, the linewidth and the integral intensity of the signal remained practically unchanged. Identical results were obtained for shorter (5 ms) or longer (20 ms) chunk times (data not shown).

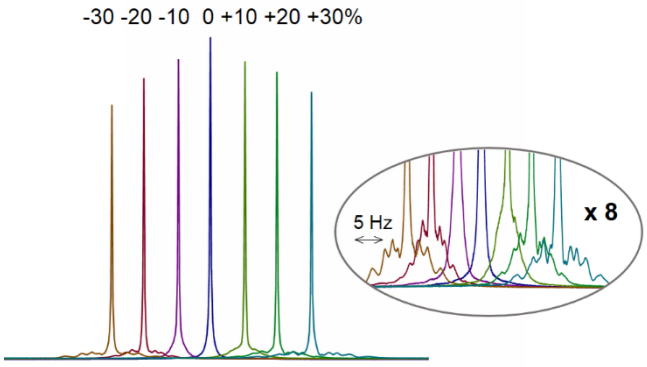

Figure 4.14: Overlay of ^{19}F sel-SHARPER spectra of **4** with pulses miss set by ± (10, 20 and 30)%. The inset shows an 8-fold vertical expansion of spectra. Spectra were acquired using the pulse sequence of Figure 4.2, with 10 ms acquisition chunks.

These results demonstrate that SHARPER compensates for pulse imperfections remarkably well despite acquisition taking place during hundreds of spin-echoes of appreciable length.

4.2.2 Reaction Monitoring and Chemical Exchange

Protodeboronation of 2,3,6-trifluorophenyl boronic acid

An example of reaction monitoring, protodeboronation of 2,3,6-trifluorophenyl boronic acid (**7**), using SHARPER can be seen in Figure 4.15. The reaction was initiated using a stopped-flow NMR system, described in Chapter 2, to allow fast and efficient mixing of the boronic acid solution, with a KOH solution, in dioxane/water. Several sel-SHARPER experiments were performed to study each of the ^{19}F signals of both reactants and products, as can be seen in Figure 4.15.

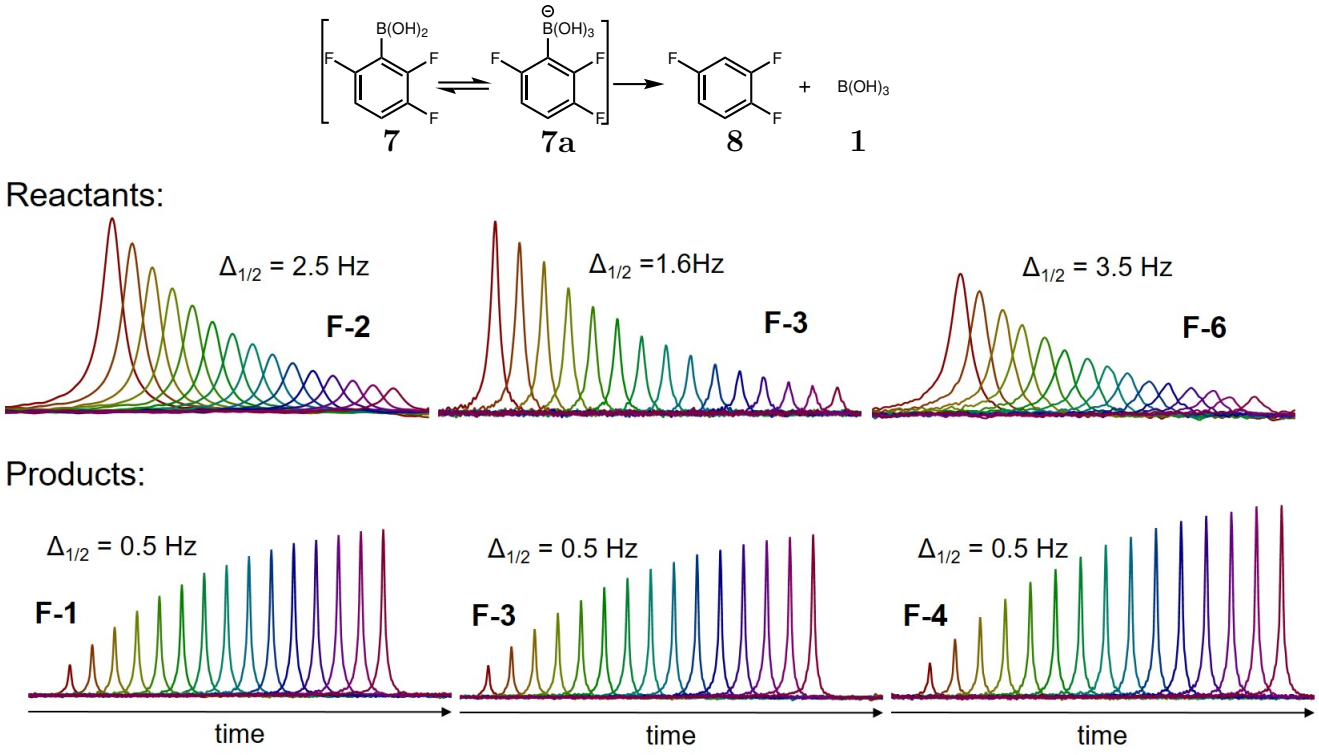

Figure 4.15: ^{19}F sel-SHARPER NMR spectra following the KOH facilitated protodeboronation of 2,3,6-trifluorophenyl boronic acid (**7**)to 1,2,4-trifluorophenyl (**8**). The signals of the reactant (top row) and product (bottom row) as acquired in a stopped-flow experiment.

In the runs shown in Figure 4.16, the magnetic field was deliberately made non-homogeneous, as evidenced by the imperfect line shape of the trifluoroacetic acid (TFA, see inset in Figure 4.16b) that was used as a (pH) stabilizer in the stock solution of **7**. The signals arising from F-2 of the reactant, which convert to F-2 of the product via protodeboronation (k_{obs} = 1.28 x 10^{-2} s^{-1}), are intense and narrow. This stands in contrast to the very broad mul-

tiplets observed during analysis by standard 1D ^{19}F NMR techniques. The numerous scalar couplings and line broadening by the magnetic field inhomogeneity would make extraction of the kinetic data very much less reliable than that acquired using sel-SHARPER.

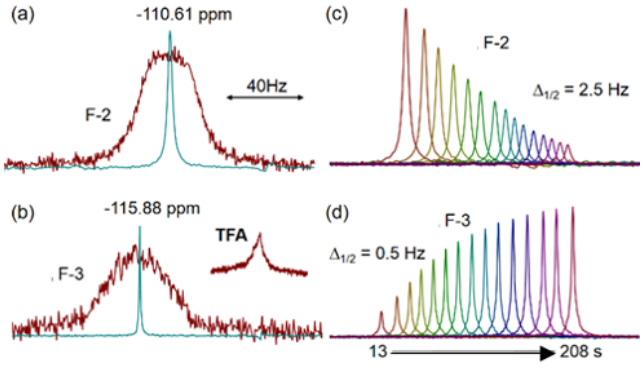

Figure 4.16: Monitoring protodeboronation of 2,3,6-trifluorophenyl boronic acid (**7**). (a) and (b) show an overlay of ^{19}F signals of the reactant and product from a ^{1}H coupled ^{19}F spectrum of the reaction mixture and sel-SHARPER spectra of F-2 and F-3. The inset in (b) shows the signal of trifluoroacetic acid, indicating poor magnetic field homogeneity; (c) and (d) follow intensity changes over 3.5 minutes. The $\Delta_{\frac{1}{2}}$ values are indicated.

Each of the ^{19}F products signals were sharp and narrow, $\Delta_{\frac{1}{2}} = 0.5$ Hz, however the reactants were notably broader, ranging from 1.6 to 3.5 Hz. As SHARPER compensates for field inhomogeneity, and each fluorine signal was broadened to a different extent, the additional line broadening must be due to chemical exchange. Hence excess line broadening (i.e. $\Delta_{\frac{1}{2}}$ >1.5 Hz) can be interpreted in terms of dynamics associated with underlying equilibrium processes. In this example, **7** is in rapid exchange with the equivalent trihydroxy-boronate anion (**7a**), the key intermediate in the protodeboronation reaction. This line broadening depends on several factors: (i) the rate of equilibrium, (ii) the differences in chemical shift between the two exchanging sites and (iii) the equilibrium population.

Chemical Exchange of Aryl Boronic Acids - 2,4-difluorophenyl boronc acid

Due to the short half-life of the protodeboronation of **7** ($t_{\frac{1}{2}} = 90$ seconds), it was decided to study the rate of exchange of an analogous molecule, 2,4-difluorophenyl boronic acid (**18**), which has a much slower rate of protodeboronation ($t_{\frac{1}{2}} = 8$ hours, $k_{rel} \leqslant 10^{-5}$). This enabled carrying out this analysis without any time pressure, although the reactions with

shorter half lives are equally amenable to this analysis, much more in-depth analysis of the dynamics between the boronic acid and boronate was performed.

Previously, Ishihara et. al, studied the analogous boric acid (A) – borate (B) equilibrium (Equation 4.1) in detail by ^{11}B NMR.

$$\mathrm{A} \underset{\mathrm{k_b}}{\overset{\mathrm{k_a}}{\rightleftharpoons}} \mathrm{B} \tag{4.1}$$

It was shown that k_a increases linearly with [OH^-], approaching a constant value: $k_a = k_2 c_T$, when [OH^-] $\gg K_b$ (where $c_T = c_A + c_B$, the total boron concentration; and K_b is the basicity constant of the borate, B). Thus, NMR analysis of the apparent exchange rate (Equation 4.1) at known c_T, allows determination of k_2 ($M^{-1}s^{-1}$), the intermolecular rate constant for degenerate OH^- exchange between pairs of boric and borate reactants (Equation 4.2).

$$A^* + B \underset{}{\overset{\mathrm{k_2}}{\rightleftharpoons}} B^* + A \tag{4.2}$$

When applied to our system, A, A* and B, B* are 2,4-difluorophenyl boronic acid (**18**) and its counter boronate species (**18a**) respectively. To determine k_2, we analysed ^{19}F sel-SHARPER and 1D ^{19}F spectra of a series of 2,4-difluorophenyl boronic acid/boronate samples (c_T = 0.1 M) containing 0.1 to 1.7 equivalents of exogenous OH^-. The excess line broadening was determined from the measured line widths of the sel-SHARPER spectra, or by matching the signals in 1D spectra with those generated by applying an appropriate line broadening to the spectrum of **18a** measured at larger excess of OH^-. As indicated, the 2,4-difluorophenylboronic acid/boronate exchange (Eqn. 4.1) is fast on the chemical shift scales ($k_a \gg \Delta\omega$, where $\Delta\omega = \Omega_A - \Omega_B$ and Ω_A, Ω_B are the resonance frequencies of spins in sites A and B in the absence of chemical exchange) and also on the relaxation time scale ($\Delta\omega \gg \Delta R_2$ and $k_{ex} \gg \Delta R_2$, where $\Delta R_2 = \Delta R_{2B} - \Delta R_{2B}$ and ΔR_{2A}, ΔR_{2B} are the relaxation rate constants for spins in sites A and B in the absence of chemical exchange and $k_{ex} = k_a + k_b$). Under these circumstances, the relative site populations, p_A and p_B ($p_A + p_B = 1$) satisfy the balance relationship $p_A k_A = p_B k_B$. If $p_A \gg p_B$ (or $p_B \gg p_A$), the transverse relaxation rate constant R_2 of the population-averaged resonance line is given by Equation 4.3.

$$R_2 = R_2^0 + \frac{p_A p_B \Delta\omega^2}{k_{ex}} \tag{4.3}$$

Where $R_2^0 = p_A R_{2A} + p_B R_{2B}$ and the position of the observed spectral line is given by Equation 4.4.

$$\Omega = p_A \Omega_A + p_B \Omega_B \tag{4.4}$$

Based on the measured values of Ω_A, Ω_B, Ω, R_{2A} and R_{2B} values of p_A and k_{ex} were calculated using Equations 4.3 and 4.4. One can express the p_A using these equations.
As previously, only one signal is observed for each fluorine nucleus due to the fast exchange on the NMR time-scale. When super-stoichiometric OH^- is added, the signals sharpen as the equilibrium is pushed towards to boronate (**18a**) (see the F-2 signals in Figure 4.17).

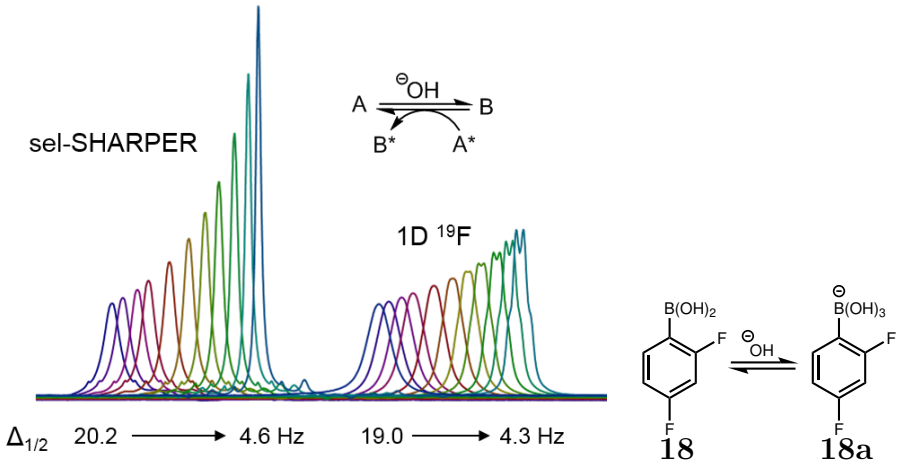

Figure 4.17: Overlay of ^{19}F sel-SHARPER (left) and ^{19}F 1D (right) F-2 signal of 2,4-difluorophenyl boronic acid undergoing the equilibrium shown in the inset. The $\Delta_{\frac{1}{2}}$ values, determined as explained in the text, are indicated for the first and last titration point using increasing KOH concentration.

A comparison of the two methods (i.e. SHARPER vs. standard 1D NMR) revealed that the $\Delta_{\frac{1}{2}}$ values obtained by SHARPER are systematically larger, by a factor of 1.069 for F-2, and 1.062 for F-4. This increase is due to additional relaxation occurring during the PFGs and 180° pulses applied between the acquisition chunks of the SHARPER acquisition period. When $t_{chunk} \gg \delta_{(PFG+pulses)}$, a linear approximation can be used to calculate a linewidth correction factor (Equation 4.5; for details see Figure 4.18).

$$t_{chunk}/(t_{chunk} + \delta_{(PFG+pulses)}) \quad (4.5)$$

For our experimental setting this factor is 1/1.06, which is in a very good agreement with the average experimental values of 1/1.066. After correction of the $\Delta_{\frac{1}{2}}$ values, Equations 4.2 and 4.5 were used to analyse the data (Table 4.3). For F-2, the population of A (i.e. 2,4-difluorophenyl boronic acid), p_A, varied between 0.022 and 0.167, yielding k_{ex} = 132,000 ± 13,500 s^{-1} and 134,000 ± 16,000 s^{-1}, as an average of eleven measurements, for SHARPER and 1D ^{19}F spectra, respectively. For F-4, p_A varied between 0.018 and 0.150 yielding k_{ex} = 146,000 ± 6,800 s^{-1} and 149,000 ± 8,200 s^{-1} for SHARPER and 1D ^{19}F spectra, respectively (Figure 4.18).

As Equations 4.3 and 4.4 are valid only when there is very large excess of either A or B (i.e. 2,4-difluorophenyl boronic acid/boronate), we simulated a two-site exchange process according to the expressions derived by Rogers and Woodbrey. Using experimental values of $\Delta\omega$ for F-2 (1061 Hz) and F-4 (3552 Hz), with p_A ranging from 0.001 and 0.16 and k_{ex} between 110,000 and 145,000 s^{-1}, allowed determination of Ω and R_2. These were then used to calculate k_{ex}, according to Eqns. 4.3 and 4.4. The values for k_{ex} obtained in this way showed relative standard deviations between 1 and 3% (data not shown) across the stated p_A range, indicating that the use of Equations 4.3 and 4.4 is justified.

Table 4.3: Parameters of F-2 and F-4 of 2,4-difluorophenyl boronic acid (**18**) during the KOH titration

0.1M KOH added /μL	F-2			F-4		
	Distance from F-2 /Hz	$\Delta_{\frac{1}{2}}$ /Hz		Distance from F-4 /Hz	$\Delta_{\frac{1}{2}}$ /Hz	
		SHARPER	1D ^{19}F		SHARPER	1D ^{19}F
50	177.5	19.1	19.0	533.5	148.3	147.8
60	166.5	17.6	17.8	500.5	140.5	138.8
70	153.3	16.9	17.0	456.6	127.2	128.8
80	140.6	15.8	16.0	419.2	119.2	118.9
90	117.6	13.6	13.5	348.8	100.8	101.9
100	97.6	11.5	11.9	286.3	85.1	84.0
780	80.8	9.8	9.9	233.3	71.6	69.6
800	65.9	8.4	8.3	191.4	59.3	57.1
810	49.2	6.7	6.5	139.6	45.4	42.2
830	29.6	5.3	5.3	96.4	31.6	30.2
850	23.7	4.3	4.3	62.7	20.8	20.8

During analysis of the data using Equations 4.3 and 4.4 several observation were made. It was thought that both ^{19}F signals would provide identical results, however the population of the boronic acid/boronate values were determined based on F-2 and F-4. The rate of exchanges were therefore slightly different, with F-4 being more accurate. Such variation can account for the differences between the p_A values from analysis of F-2 and F-4 signals. To explore this hypothesis, the F-4 derived values were deemed to be accurate and the F-2 chemical shifts were adjusted to achieve an agreement between the two data sets. When a gradual and approximately linear movement of the F-2 signal across the studied range of OH^- concentrations was implemented (from -23 to -7 Hz), it was possible to obtain practically identical p_A values based on both fluorine atoms (Figure 4.18).

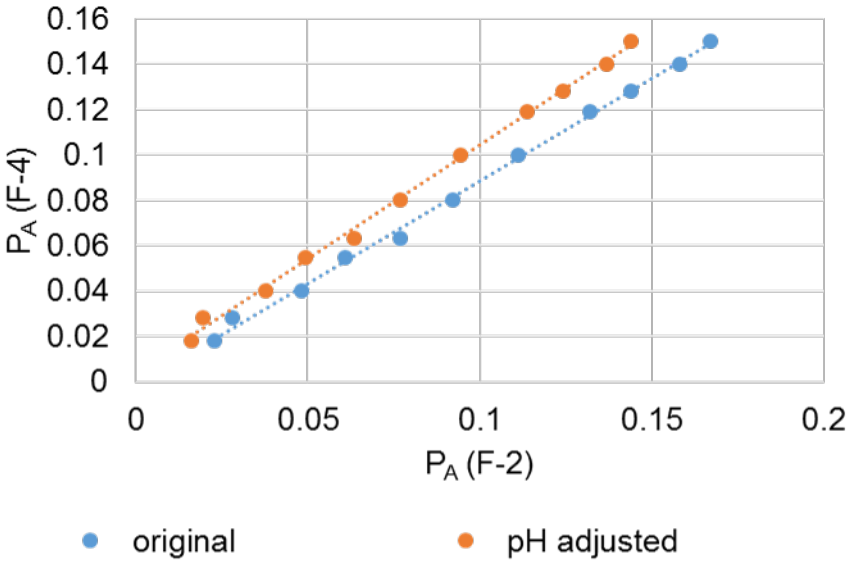

Figure 4.18: A comparison of p_A values obtained by the analysis of F-2 and F-4 of 2,4-difluorophenyl boronic acid signals during the KOH titration. Blue data points represent correlations of the original data. The orange data points represent the data for which the observed chemical shift were corrected for each titration point in a linear fashion between -23 and -7 Hz with an increment of -1.6 Hz. Note that the points with the largest p_A represents the beginning of the titration. Linear regression lines are shown to indicate the goodness of the fit. Achieving a slope of 1.0 was one of the criteria for the optimization of the correction factor, while the other was decreasing the standard deviation of k_{ex} values for the SHARPER data.

Using such adjusted p_A values in Equation 4.3, a new average rate constants, k_{ex} = 109,000 ± 5,600 s^{-1} and 111,000 ± 7,400 s^{-1} for SHARPER and 1D ^{19}F spectra, were obtained for F-2, respectively. Although these are lower than the F-4 based values, their standard deviations have halved and became similar to those of the F-4 based k_{ex} values.

Additional observations were made, which indicate that it is problematic to isolate the 2,4-

difluorophenyl boronic acid/boronate exchange contribution to the position of spectral lines: (ii) addition of a large access of KOH resulted in a 17 Hz shift of the F-4 signal, while F-2 has moved by as much as 64 Hz; (ii) at the same time the measured linewidth of both fluorine lines differ substantially between the boronic acid and the boronate (0.7 Hz for both F-2 and F-4 of **18**, while 2.5 and 4.1 Hz, respectively, for **18a**). Based on the experimental and simulated data, shifts of this magnitude are not a consequence of the equilibrium. These observations indicate a pH dependency of the fluorine chemical shifts and/or involvement of boronate in another equilibrium. The latter would account for the larger linewidths of the boronate observed for the end points of the KOH titration.

Based on the above analysis, we report the F-2 and F-4 derived average rate constant k_{ex} = 130,000 ± 20,000 s^{-1} and calculate the intermolecular rate constant for degenerate OH^- exchange between pairs of **18**/**18a** as $k_2 = k_{ex}/c_T$ = (130,000 ± 20,000)/0.1 = 1.3 ± 0.2 x $10^6 M^{-1}s^{-1}$.

The observed differences between the F-2 and F-4 based k_{ex} values therefore are not a consequence of the choice of data interpretation formalism. They arise because the observed positions of the spectra lines are affected not only by the exchange, but also by additional factors such as changing pH and possibly also the existence of an additional equilibrium.

Despite the observation that the k_{ex} values differ slightly depending on which of the two sites (F-2 versus F-4) is analysed, the rate determined for degenerate intermolecular ^-OH transfer between boronic acid/boronate (k_2 = 1.3 ± 0.2 x $10^6 M^{-1}s^{-1}$) compares well with those reported by Ishihara for boric acid / borate (k_2 = 2.6 x $10^6 M^{-1}s^{-1}$)[87] and for methylboronic acid / methylboronate (k_2 = 0.70 x $10^6 M^{-1}s^{-1}$).[88]

Oxidation of Diphenylphosphine

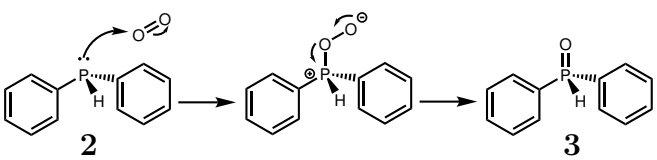

2 **3**

Figure 4.19: Oxidation of diphenylphosphine

To push SHARPER futher, studying a reaction that required bubbling, the oxidation of **2** to **3** was monitored. Air was bubbled into a solution of diphenylphosphine in toluene-d_8. This example also demonstrates the ability of SHARPER to remove large heteronunclear coupling ($^1J_{PH}$ of 215.9 Hz). Such a large coupling however, did require very short chunk times, of around 1 ms to maximise the benefits of SHARPER as shown in Figure 4.20.

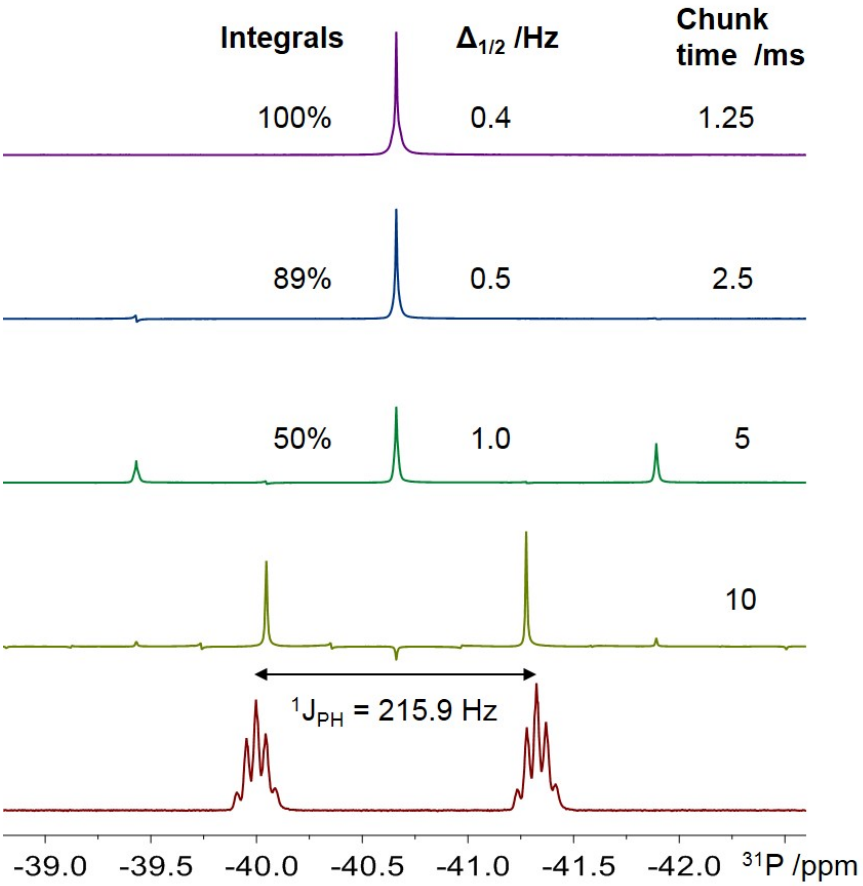

Figure 4.20: Effects of the chunk length on the ^{31}P sel-SHARPER spectra diphenylphosphine (**2**), acquired using the pulse sequence of Figure 4.4. The bottom spectrum is a reference ^{1}H coupled ^{31}P spectrum of diphenylphosphine. Note that the long-range splittings are removed for all chunk times, while a reduced one-bond splitting is present in the 10 ms chunk-time spectrum. Some irregular line-shape is notable at the foot of the SHARPER spectra. The signal narrows and becomes more intense as the chunk time is shortened.

Short chunk times are also required to minimize the effects of gas bubbles. Figure 4.20 shows integral intensities of the ^{31}P signal of **2** during the oxidation to **3**, including examples of spectra.

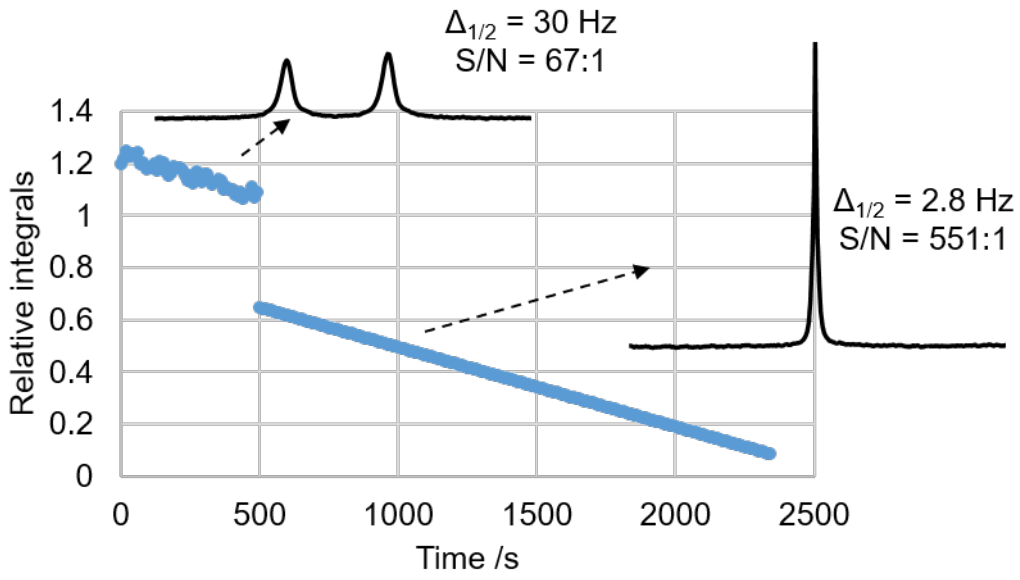

Figure 4.21: Integral intensities of ^{31}P signal of diphenylphosphine during the oxidation induced by bubbling air through the solution. The initial points correspond to 1D ^{31}P spectra, while the latter to the sel-SHARPER spectra. The spectra, plotted on the same scale, and acquired at the changeover point of the monitoring method are shown together with their attributes.

It can be seen that the SHARPER signals show smaller immediate fluctuation of integral intensities, narrow linewidths and significantly larger S/N ratio (despite the overall drop of integral intensities of ∼40% relative to the 1D spectra). These attributes of the SHARPER pulse sequence make it a useful tool for monitoring chemical reactions under challenging conditions of gas sparging. Chunk times of 0.8 ms were used. Initially, 1D ^{1}H coupled spectra were used to monitor the reaction. At about 500 s into the monitoring, the acquisition of SHARPER spectra was initiated.

4.3 Conclusions

A simple and robust pure-shift NMR method termed SHARPER (Sensitive, Homogeneous And Resolved PEaks in Real time) has been developed and its parameters analysed in detail to provide guidelines for its most effective application. SHARPER effects hetero- and homonuclear decoupling of all nuclei without the need to pulse on the X channel, yielding significant improvements in achievable S/N ratio. It is also insensitive to magnetic field inhomogeneity, either static or within certain limits also dynamic inhomogeneity, making it

a valuable tool for quantitative monitoring of chemical reactions and parameters of chemical exchange in challenging environments. These attributes were exemplified by several examples, including protodeboronation of polyfluorinated aryl boronic acids; an investigation of a very fast accompanying boronic acid/boronate equilibrium; and oxidation of diphenylphosphine in the presence of intense air bubbling.

4.4 Experimental

Spectra were acquired on a two-channel 400 MHz Bruker Avance III NMR spectrometer equipped with a Prodigy probe or on a three-channel 400 MHz Bruker Avance III NMR spectrometer equipped with a 5 mm z gradient BB TBO ^{1}H, ^{19}F probe.

The ^{19}F spectra of FB (**4**) in $CDCl_3$ presented in Figure 4.3 were acquired using SHARPER (Figure 4.2), using the following parameters: 2 dummy scans, 4 scans, 1.5 s relaxation delay, 17.4 s acquisition time, 17 μs 90° pulse, 34 μs 180° pulse, n=256, with a chunk time of 34 ms.

The ^{19}F SHARPER spectra of a mixture of 1,2,4-trifluorophenyl (**8**) and 1,2,4-trifluoro-3-deuterophenyl (**14**) in a mixture of 1:1 CD_3OD/H_2O presented in Figure 4.5. Spectra were acquired using sel-SHARPER (Figure 4.4), using the following parameters: 2 dummy scans, 4 scans, 10 s relaxation delay, 3.49 s acquisition time, 8.25 μs 90° pulse, 10 ms 180° sinc pulse during the SPFGSE, n=128, with a chunk time of 13.6 ms The spectra were processed by applying a 0.1 Hz exponential line broadening and a forward complex linear prediction (the stated signals half-height linewidths quote values without this additional line broadening).

The ^{19}F SHARPER spectra shown in Figure 4.6 were acquired using identical parameters as used for the spectra of Figure 4.5, but with the x, y, z, z^2, z^3, xy, xz and yz shim corrections deviating by + 500 units from their optimal values.

The ^{19}F SHARPER spectra in Figure 4.7, show the effects of magnetic field inhomogeneity. An overlay of 1D and sel-SHARPER (Figure 4.4) of 1,2,4-trifluorophenyl (**8**), produced from the KOH catalysed protodeboronation of 2,3,6-trifluorophenyl boronic acid (**7**). Panel A and B present spectra acquired using the pulse sequence of Figure 4.4, using the following parameters: 2 dummy scans, 4 scans, 5 s relaxation delay, 2.18 s acquisition time, 8.25 μs

90° pulse, 10 ms 180° Gaussian pulse during the initial SPFGSE and 250 μs 180° rectangular pulses were applied during the acquisition, n=218, with a chunk time of 5.01 ms. The degree of miss shimming of x, y, z, z^2 and Z^3 shims is indicated in the figure.

The ^{19}F SHARPER spectra of fluorobenzene (**4**) presented in Figure 4.8 were acquired using the pulse sequence of Figure 4.2. Spectra were acquired using the following parameters: 2 dummy scans, 2 scans, 3 s relaxation delay, 1.09 s acquisition time, 8.25 μs 90° pulse, 70 μs 180° Gaussian pulse during acquisition, with variable n and chunk times. The loop parameter n was set to 64, 128, 256 or 512, yielding acquisition chunks of 8.5, 4.25, 2.13 and 1.06 ms. The spectra were processed by applying a 0.5 Hz exponential line broadening (the half-height linewidths are quoted without this additional line broadening).

The integrals shown in Figure 4.9 were obtained from ^{19}F spectra of the oxidation of 4-fluorophenyl boronic acid (**15**) to **19**. The spectra were acquired using the pulse sequence of Figure 4.4 with the following parameters: 2 dummy scans for the initial scan, 4 scans, 3 s relaxation delay, 1.5 s acquisition time, 8.25 μs 90° pulse, 10 ms 180° Gaussian pulse during initial SPFGSE and acquisition, n=192, and a chunk time of 2.6 ms, with 600 spectra acquired.

The integrals shown in Figure 4.10 were obtained from ^{19}F spectra of TFE (**5**) in d_4-methanol. Spectra were acquired using the pulse program shown in Figure 4.2, with the following parameters: 2 dummy scans for the initial scan, 2 scans, 3 s relaxation delay, 1.5 s acquisition time, 8.25 μs 90° pulse, 1 ms 180° Gaussian pulse during initial SPFGSE and 16.5 μs 180° pulses during acquisition, n=130, and a chunk time of 4 ms, with 64 spectra acquired.

The ^{1}H spectra shown in Figure 4.11 are obtained using 1D ^{1}H sequence, and sel-SHARPER (Figure 4.4), with Panel A and B showing different parts of the spectra. Panel A (b) shows ^{1}H sel-SHARPER spectrum of H9, acquired using the following parameters: 2 dummy scans, 4 scans, 2 s relaxation delay, 2.72 s acquisition time, 8.4 μs 90° pulse, 10 ms 180° Gaussian pulse during SPFGSE and acquisition, n=64, with a chunk time of 21. ms. Panel B (b) shows $H6_{ax}$, acquired using the following parameters: 2 dummy scans, 4 scans, 2 s relaxation delay, 1.6 s acquisition time, 8.4 μs 90° pulse, 20 ms 180° Gaussian pulse during SPFGSE and acquisition, n=64, with a chunk time of 12.5 ms. Panel B (c) shows the spectrum of

$H5_{eq}$, acquired using the following parameters: 2 dummy scans, 4 scans, 2 s relaxation delay, 0.8 s acquisition time, 8.4 μs 90° pulse, 80 ms 180° Gaussian pulse, n=8, with a chunk time of 50 ms. Spectra within each panel are drawn using identical vertical scales. The vertical scale in Panel A was scaled down by $\frac{1}{2}$ compared to Panel B.

The ^{19}F spectra shown in Figure 4.12, of F-1 of 1,2,4-trifluorophenyl (**8**). The bottom spectrum is a reference spectrum. Spectra were acquired using the sel-SHARPER program, Figure 4.4, with the following parameters: 2 dummy scans, 4 scans, 4 s relaxation delay, 2.556 s acquisition time, 125 μs 90° pulse, 1 ms 180° Gaussian pulse during the SPFGSE and 250 μs rectangular 180° pulses during the acquisition. The length of 180° rectangular pulses was set the avoid perturbation of F-3 and F-4 spins. Four acquisition chunk lengths were used (4.992, 9.984, 19.958 and 36.668 ms) producing sidebands at ± 200.32, 100.16, 50.08 and 25.04 Hz respectively. The spectra were processed using exponential line broadening of 0.1 Hz; this value was subtracted from the reported linewidths. Data shown in Table 4.2, shows parameters of spectral lines.

The ^{19}F spectra shown in Figure 4.13, of F-1 of 1,2,4-trifluorophenyl (**8**). Spectra show the effects of the mismatch between the RF carrier and the resonance offset on SHARPER. The eleven spectra were obtained increasing the carrier offset relative to the F-1 signal chemical shift in steps of -10 Hz up to -100 Hz. All series show spectra for chunk times of 4.992, 9.984 and 19.968 ms, for a, b and c respectively, with sidebands at 200.32, 100.16 and 50.08 Hz. Spectra were obtained using sel-SHARPER, Figure 4.4, using the following parameters: 2 dummy scans, 4 scans, 5 s relaxation delay, 8.4 μs 90° pulse,initial 180° selective pulse was a 1 ms Gaussian pulse and 250 μs 180° rectangular pulses were applied during the acquisition, n=55. Dashed lines indicate the three signal in each spectrum, the integrals of which were summed up to give the integral intensities listed next to the spectra (relative to the sum for the on-resonance spectrum in each experiment). Signal in (a) with the carrier frequency miss set by -80 Hz was expanded vertically to illustrate the broadening at the foot of the signal. Note that when the carrier displacement reaches a multiple of the sideband frequency, the sideband signals move to the left by the amount of the sideband frequency (e.g. for the carrier offset of -100 Hz in (b) and -50 and -100 Hz in (c)).

The overlay of ^{19}F spectra of FB (**4**), shown in Figure 4.14 were acquired using SHARPER,

Figure 4.2, using the following parameters: 2 dummy scans, 4 scans, 2 s relaxation delay, 5.11 s acquisition time, 8.25 μs 90° pulse, 63 μs 180° pulse, n=256, with a chunk time of 10 ms. Pulses were miss set by ± (10, 20 and 30) %. The inset shows an 8-fold vertical expansion of spectra.

KOH catalyzed protodeboronation of 2,3,6-trifluorophenylboronic acid/boronate (**7**/**7a**) to 1,2,4-trifluorophenyl (**8**) in 1:1 H_2O/dioxane mixture was monitored by the acquisition of ^{19}F NMR sel-SHARPER spectra (pulse sequence of Figure 4.4) in a stop-flow experiment. The results can be seen in Figure 4.15 and Figure 4.16. Spectra shown in Figure 4.15, show the signals of the reactant **7**/**7a** (top row) and the product **8** (bottom row). Spectra were acquired using the following parameters: 2 dummy scans, 2 scans per spectrum, 1.5 s relaxation delay, 4.99 s acquisition time, 10 ms Gaussian pulses, n=128, with a chunk time of 8.5 ms. 16 spectra were acquired with the first and last time points being 13 and 208 s respectively. The top and bottom spectra were processed using an exponential function of 1 and 0.2 Hz respectively, these values have been subtracted from the linewidth given. Spectra shown in Figure 4.16 were using identical acquisition parameters.

Spectra of 2,4-difluorophenylboronic acid (**18**) in 1:1 H_2O/dioxane mixture presented in Figure 4.17 were acquired using the sel-SHARPER pulse sequence of Figure 4.4, using the following parameters: 2 dummy scans, 4 scans, 3 s relaxation delay, 1.5 s acquisition time, 93 μs 90° pulse, 1 ms 180° Gaussian pulse during the SPFGSE and 186 μs rectangular 180° pulses during the acquisition, n=64, with a chunk time of 23.4 ms. The length of 180° rectangular pulses was set to avoid perturbation of the other fluorine spins. The 1D ^{19}F spectra were acquired using 2 dummy scans, 8 scans, 3 s relaxation delay, 0.87 s acquisition time. Samples were prepared by mixing 500 μl of 0.1 M 2,4-difluorophenylboronic acid (**18**) containing 0.01M trifluoroacetic acid with increasing amounts of 0.1 M (**18**) and 0.1 M KOH. In this way the concentration of **18** was kept constant. The resulting concentrations of KOH, together with obtained linewidths and chemical shifts, are reported in Table 4.3.

The ^{31}P spectra of diphenylphosphine (**2**), shown in Figure 4.20 were acquired using the pulse program shown in Figure 4.4, with the following parameters: 2 dummy scans, 2 scans per spectrum, 3 s relaxation delay, 1.28 s acquisition time, 16.3 μs 90° pulse, 92.6 μs 180° rectangular pulses were used during the SPFGSE and acquisition, with varying chunk times

and loops. The bottom spectrum is a reference ^{1}H coupled ^{31}P spectrum.

Spectra analysed in Figure 4.21 were acquired using sel-SHARPER, Figure 4.4, using the following parameters: 2 dummy scans, 2 scans, 3 s relaxation delay, 0.64 s acquisition time, 8.6 μs 90° pulse, 92.6 μs 180° rectangular pulses, n=400, with a chunk time of 0.8 ms.

Chapter 5

Modified SHARPER

5.1 Introduction

After the success of reaction monitoring using SHARPER, some minor modifications allowed improvements/different varieties of kinetics to be studied. It is often beneficial to study both reactants and products during reactions, to confirm there are no unknown intermediates, and that kinetics are reproducible. To allow this, we developed a version of SHARPER that allows multiple signals to be followed. An up-and-coming technique, multiple receiver NMR, is a useful way to increase data density – a parallel receiver version of SHARPER has been written to give twice the data density in a given time.

The final modification of SHARPER was slice selective SHARPER – the initial reason for developing SHARPER. As discussed in Chapter 3, the frequency shifted slice selective excitation pulse sequence, has a reduced active volume and therefore S/N. The decoupling powers of SHARPER along with the slice selection allows improved S/N. Several different versions of slice selective SHARPER were designed, each appropriate for different scenarios.

5.2 Results and Discussion

5.2.1 Multi-signal SHARPER

During reaction monitoring it is beneficial to monitor both reactants and products. To achieve this, a modification of SHARPER was made to allow switching between signals, the pulse program is shown in Chapter 7. As it is required to sit on resonance for SHARPER, switching between signals is achieved via a frequency list. This frequency list changes the frequency of both the pulses and the receiver. The pulse program works through the frequency list in a loop, depicted in Figure 5.1.

This new pulse program was then used to study the protodeboronation of 2,6-difluorophenyl

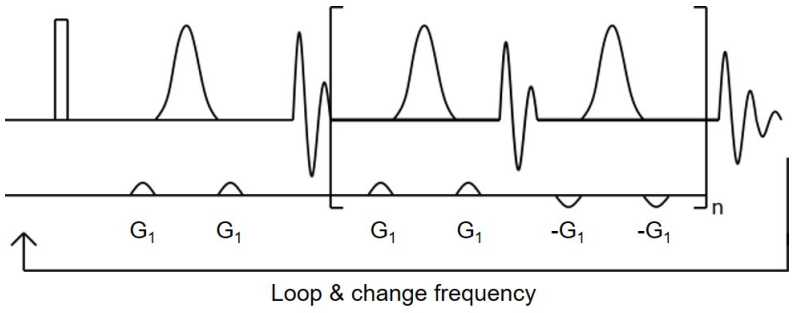

Figure 5.1: Multi-signal SHARPER pulse program, where the loop changes both the frequency of the pulse and the receiver

boronic acid (**20**). The pulse program switched between the signal of the reactant and the product utilising a frequency list of each of the signals. This then required a more involved processing, whereby every other 1D slice needs to be collated to give each signals pseudo-2D stack. The different signals both appear to be at the same frequency as both the receiver and r.f. pulse are switched, so the receiver still sees it as the set frequency. Once the alternating signals have been separated out, either manually or using any processing/coding software. The kinetics were analysed as can be seen in Figure 5.2.

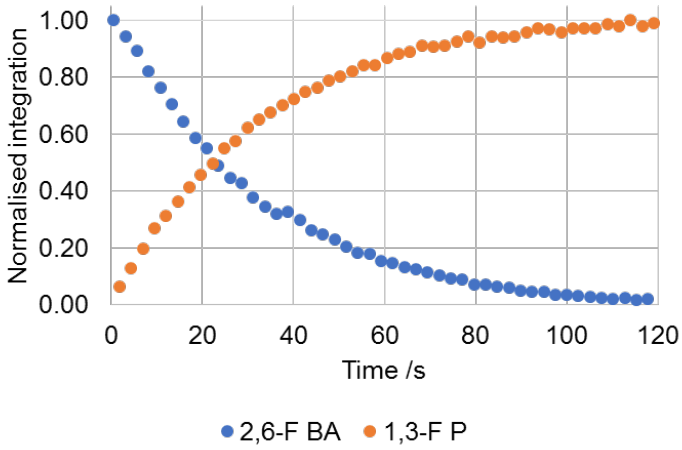

Figure 5.2: Protodeboronation kinetics of the 2,6-difluorophenyl boronic acid (**20**) with KOH in 1:1 water/dioxane at 293 K. Where 2,6-F BA is 2,6-difluorophenyl boronic acid, and 1,3-F P is 1,3-difluorophenyl.

The data of both reactant and product was analysed to give the rate $k = 0.036$ s^{-1}, which is expected. The monitored signals have the same line widths as when they were monitored individually (Chapter 4). In this example it is easy to differentiate between reactant and product as the line-widths differ, however as the chemical shift information is lost due to switching the pulse and receiver frequency concurrently, it is important to keep track of the frequency offsets being monitored.

5.2.2 Dual receiver SHARPER

Building on multiple signal SHARPER, we also modified SHARPER to be compatible with multiple receiver techniques. Multiple receiver technology is a recent development in NMR spectroscopy, it allows increased productivity/efficiency. There are different approaches to multiple receiver experiments: parallel, sequential and interleaved acquisition, as discussed in Chapter 1. Dual receiver SHARPER (DR-SHARPER) utilises parallel acquisition, whereby the two nuclei are identically manipulated in one experiment, shown in Figure 5.3. The full pulse program can be seen in Chapter 7.

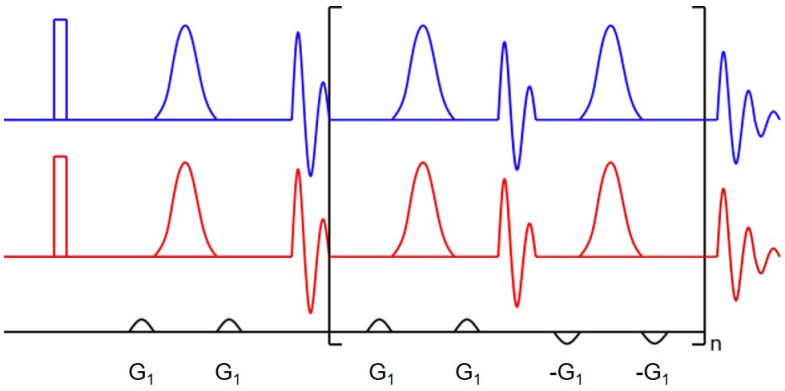

Figure 5.3: Dual receiver SHARPER pulse program. Where blue is receiver one and red is receiver two.

This allows multiple nuclei to be monitored at the same time, and the basic principle was tested using a parallel acquisition DR-SHARPER 1D sequence. 2,4-difluorophenyl boronic acid (**18**) was studied using ^{1}H and ^{19}F, δ of 6.94 and -118.83 ppm respectively.

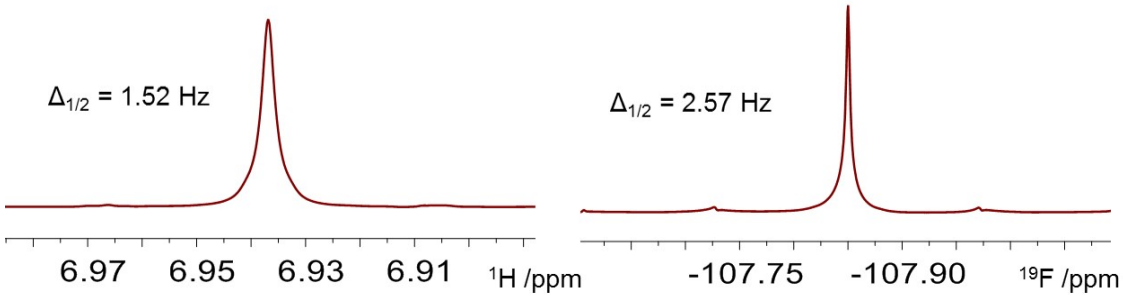

Figure 5.4: ^{1}H (H-3) and ^{19}F (F-4) dual receiver SHARPER spectra of 2,4-difluorophenyl boronic acid (**18**)

This pulse program works the exact same way as SHARPER, however, as multi-receiver

pulse programs work using the same acquisition parameters it is important to tweak these to allow optimum results for both nuclei. As can be seen in Figure 5.4 the linewidths are slightly broader than expected for SHARPER spectra, this will be due to the boronic acid-boronate exchange, described in Chapter 4. Another potential reason for this excess broadening, is due to the parameters not being optimised for both nuclei, causing slightly broader linewidths as well. The parameters are not able to be optimised for both nuclei, as during parallel multiple receiver experiments use the same delays, pulses, acquisition time.

5.2.3 Slice selective SHARPER

One of the initial reasons for developing SHARPER was the lack of sensitivity during spatially selective frequency shifted experiments. To improve this limitation several different slice selective SHARPER experiments were developed, each appropriate for a particular application. All of which will be explored in this chapter.

The most basic form of slice selective SHARPER was written to test if it was possible to combine SHARPER and slice selection. The pulse sequence starts with a slice selective excitation using a 90° selective pulse in the presence of a pulsed field gradient and is followed by modified SHARPER where PFGs are also applied during the 180° selective pulses during the acquisition chunks as shown in Figure 5.5.

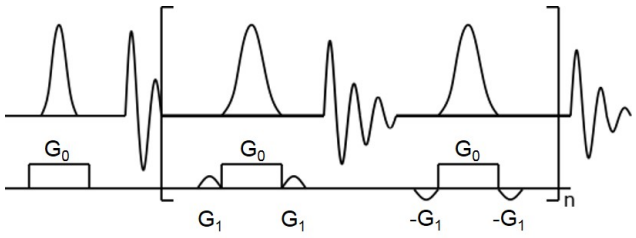

Figure 5.5: Basic slice selective SHARPER

To test the basic principles a sample of 4-fluoroacetophenone (**21**) was used. The results can be seen in Figure 5.6, which produced a series of narrow singlets, with a $\Delta_{\frac{1}{2}}$ 0.45 Hz, which is expected when utilising SHARPER .

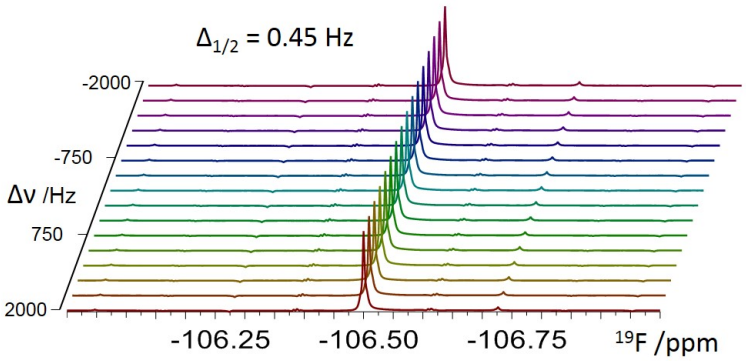

Figure 5.6: Stacked slice selective SHARPER spectra of **21** in d_8-THF

Once the fundamental principles of slice selective SHARPER were established, we needed to make modifications to develop a more generally applicable pulse sequence. The issue with the basic form of the slice selective SHARPER is that if more than one signal is present in the spectra, all will be excited at varying positions in the NMR tube. This is not compatible with SHARPER, which requires one signal to be selected. To overcome this limitations and to study more complex molecules, modifications were made, shown in Figure 5.7. The pulse program consists of a selective 90° pulse to excite the desired signal, followed by a selective 180° pulse at the same time as a rectangular gradient, with shaped flanking gradients. The acquisition follows the same basic principle as SHARPER, however simultaneously with 180° pulses, a rectangular gradient pulse was performed, to give the slice selective element. This pulse program was written to allow studying of systems with more than one signal, in much the same way as sel-SHARPER.

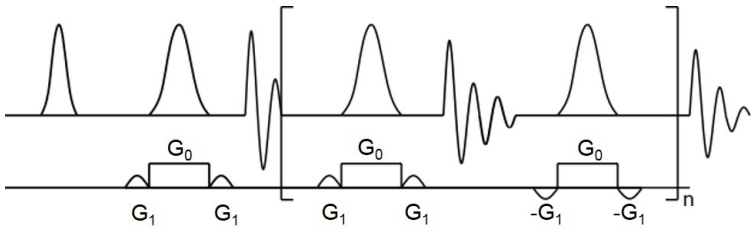

Figure 5.7: Basic slice selective sel-SHARPER

This pulse program was tested using 2,4-difluorophenyl boronic acid (**18**), to test its ability to perform slice selective SHARPER on one signal without other signals interfering. As can be seen in Figure 5.8, the pulse program produces narrow singlets as expected.

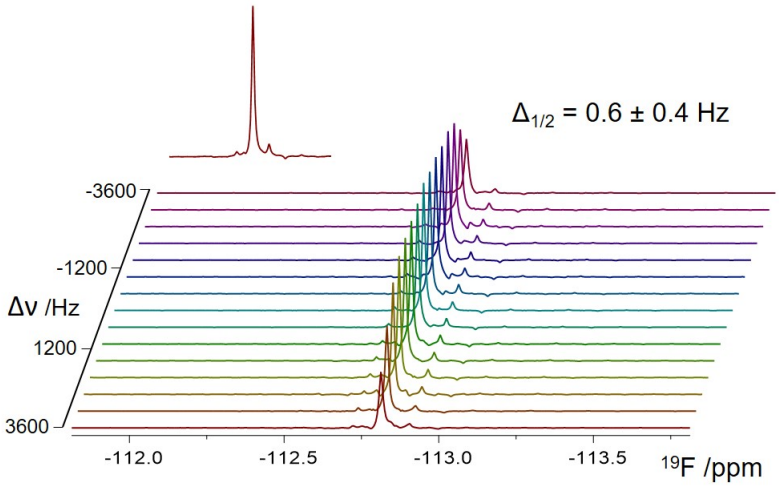

Figure 5.8: Spectra of **18** using selective slice selective SHARPER shown in Figure 5.7

Overall the sequence allowed for uniform sampling of slices within the coil, producing narrow singlets. An alternative to this sequence is to replace the initial 90° selective pulse with a SPFGSE. This pulse sequence is shown in Figure 5.9.

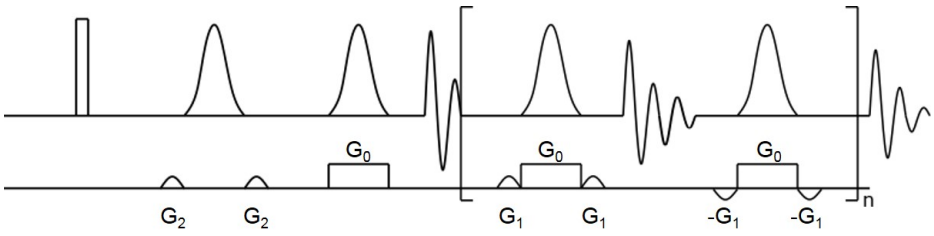

Figure 5.9: Slice selective double 180° SHARPER pulse program

Testing of the double 180° slice selective SHARPER was performed using fluorobenzene (**4**). The results of this can be seen in Figure 5.10. The resulting spectra are singlets, with line widths of 1.4 Hz, with some chunking artefacts.

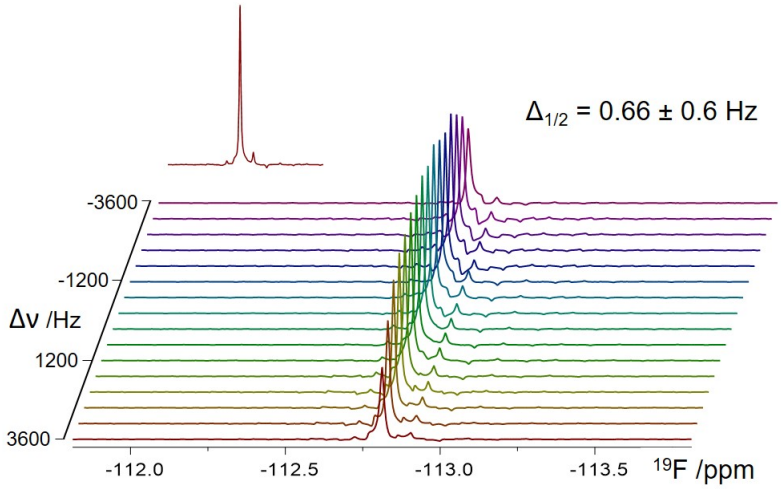

Figure 5.10: Slice selective double 180° spectrum of fluorobenzene

The initial motivation for developing slice selective SHARPER was to apply it to reaction monitoring. One of the desirable properties of slice selective NMR spectra are the rapid cycle times whereby there is no need to wait for nuclei to relax back to the z-axis, the versions of slice selective SHARPER presented so far do not allow continual acquisition. The next version of slice selective SHARPER allows for this by selectively exciting one signal by a SPFGSE and then returning the spins to the z-axis. Referred to here as z-return slice selective SHARPER. The pulse program starts with a non-selective 90° pulse, a selective 180° pulse with flanking gradients to disperse the other signals, followed by a hard 90° pulse to return the spins to the z-axis. This is then followed by a PFG to eliminate any transverse magnetisation again and selective 90° pulse with a concurrent gradient, which can be seen in Figure 5.11.

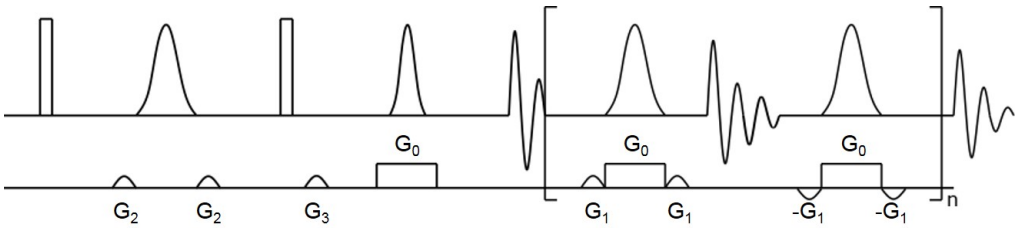

Figure 5.11: Z-return slice selective SHARPER pulse program

This was again tested on a sample of **4**, the results are shown in Figure 5.12.

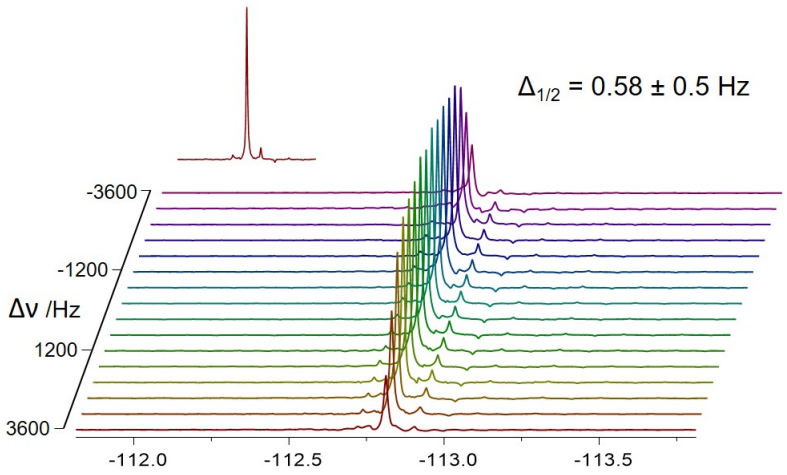

Figure 5.12: Slice selective SHARPER z-return stacked spectra of **4**

As can be seen in Figure 5.12 the resulting spectra again produce narrow line widths $\Delta_{\frac{1}{2}}$ = 0.58 Hz, and unlike the other slice selective pulse programs there needs to be no delay between scans. This allows building up data density which can be crucial in reaction monitoring by NMR.

5.3 Conclusions

Several modifications of SHARPER have been developed. The multi-signal SHARPER is highly beneficial for monitoring reactions to allow multiple signals to be studied. Dual-receiver SHARPER allows for greater data density, with all the benefits of dual receiver technology.

Several slice selective SHARPER pulse programs have been developed: basic, selective, double 180 and z-return. These pulse programs will now be utilised for reaction monitoring.

5.4 Experimental

All data, unless specified, were acquired using a two-channel 400 MHz Bruker Avance III NMR spectrometer equipped with a Prodigy probe.

The multi-signal SHARPER kinetics shown in Figure 5.2 show the protodeboronation of

2,6-difluorophenyl boronic acid. The kinetics were monitored using the SF-NMR system with 0.1M 2,6-dilfluorophenyl boronic acid (**20**) and 0.01 M TFA in syringe A; 0.2M KOH in syringe B; and pure solvent, 1:1 water/dioxane in syringe C; ratios of 0.6, 0.4, 0.0 respectively. The spectra were acquired with 2 dummy scans, 4 scans, initial 90° pulse of 8.27 μs, flanking 2% sine gradients surrounding a 14 ms Rsnob pulse, 5% sine gradients during acquisition, and a chunk time of 26 ms.

The ^{19}F and ^{1}H NMR spectra of dual-receiver SHARPER in Figure 5.4 shows two signals of 2,4-difluorophenyl boronic acid (**18**) in H_2O/dioxane (1:1). The spectra were acquired with 2 dummy scans, 2 scans, initial 15 μs 90° pulse, flanking 5% sine gradients surrounding a 10 ms 180° Gaussian pulse, 1% sine gradients during acquisition, and a chunk time of 8.7 ms. This was studied using a 500 MHz Bruker AVANCE NEO spectrometer equipped with a SmartProbe.

The ^{19}F NMR spectra of basic slice selective SHARPER in Figure 5.6 shows the slices of the 4-fluoroacetophenone (**22**) in d-DMSO. The spectra were acquired with 1 dummy scan, 4 scans, initial 15 μs 90° pulse, 17.4 μs 180° pulse, 2% sine gradients (G_1) during acquisition,1% gradient (G_0) during pulses and a chunk time of 11.7 ms. The frequency offsets used were ± 2000 Hz. Pulse program used can be seen in Figure 5.5.

The ^{19}F NMR spectra of selective slice selective SHARPER in Figure 5.6 shows the 16 slices of fluorobenzene (**4**) in d_8-Tolune. The spectra were acquired with 4 dummy scans, 2 scans, initial 8.7 μs 90° pulse, a 10 ms Rsnob pulse, 40% sine gradients (G_1) during acquisition, 2% gradient (G_0) during spatially selective pulses and chunk time of 28.3 ms. The frequency offsets used were ± 3600 Hz, in 16 steps. Pulse program used can be seen in Figure 5.7.

The ^{19}F NMR spectra using double 180° slice selective SHARPER in Figure 5.10 shows the 16 slices of fluorobenzene (**4**) in d_8-Tolune. The spectra were acquired with 4 dummy scans, 2 scans, initial 8.7 μs 90° pulse, a 10 ms Rsnob pulse with 11% flanking sine shaped gradients (G_2), 40% sine gradients (G_1) during acquisition, 2% gradient (G_0) during spatially selective pulses and a chunk time of 28.3 ms. The frequency offsets used were ± 3600 Hz, in 16 steps. Pulse program used can be seen in Figure 5.9.

The ^{19}F NMR spectra using double 180 slice selective SHARPER in Figure 5.12 shows the 16 slices of fluorobenzene (**4**) in d_8-Tolune. The spectra were acquired with 4 dummy scans,

2 scans, initial 8.7 μs 90° pulse, a 10 ms Rsnob pulse with 11% flanking sine shaped gradients (G_2), another non-selective 90° pulse followed by a 31% sine shaped purging gradient (G_3), a 10 ms Eburp pulse, 10 ms Rsnob pulses during acquisition with 40% flanking sine gradients (G_1), 2% gradient (G_0) during spatially selective pulses and a chunk time of 28.3 ms. The frequency offsets used were ± 3600 Hz, in 16 steps. Pulse program used can be seen in Figure 5.11.

Chapter 6

Conclusions

To conclude, a brand new stopped flow NMR apparatus has been developed which is compatible with any 5mm solution state NMR spectrometer. This has allowed reactions to be monitored that have not previously been possible by NMR. The stopped flow apparatus, *InsightXpress*, allows for 90 - 95% pre-magnetisation of three separate solutions, which can be rapid mixed. There is trigger functionality which allows pulse programs to be initiated once mixing has been performed. With a dead time of ¡ 180 ms this apparatus allows reactions to be monitored that have not previously been accessible by NMR.

The three separate reservoirs allow easily repeated reactions, while varying concentrations to perform kinetic analysis. The equipment greatly reduces the time taken for analysis of reaction mechanisms.

Reaction monitoring by NMR must be fast to allow rapid chemical reactions to be accessible via this technique. Poor signal-to-noise ratio (S/N) of NMR experiments is one limiting factor. Repeat scans, as means to increase the S/N take precious time. One way to help overcome this issue is to apply the concept of pure shift NMR. The collapsing of multiplets to a singlet increases S/N, decreasing the number of scans needed to be accumulated. SHARPER, an approach developed in this thesis, is a real-time selective pure shift NMR technique that addresses this issue. SHARPER produces extremely narrow singlets as it has an inherent capability to remove broadening due to magnetic field inhomogeneity. This can often be the case in reaction monitoring cause by transport of liquids, or deliberate disturbances, such as gas sparging.

SHARPER does not eliminate broadening due to chemical exchange. Broadening of SHARPER

signals therefore provides a simple means to determine the contribution of chemical exchange to the signal linewidths, and therefore use this to derive kinetic parameters of exchange equilibria. SHARPER thus provides a convenient determination of both reaction kinetics and dynamic equilibria. It has been used in this work to study protodeboronation of fluorinated aryl boronic acids, a side reaction which occurs during the Suzuki-Miyaura cross coupling reaction.

A limitation of reaction monitoring by NMR is the need to wait for re-establishing equilibrium after a rf pulse, this has been addressed previously using slice selective excitation. In this work we have improved upon this technique by address the issue of inherently low sensitivity of slice selection by incorporating SHARPER into this method. Slice-selective SHARPER enables continual acquisition, without the requirement of waiting for relaxation to occur between scans, with increased sensitivity. This allows access to fast reactions whilst building the data density possible.

Data density can also be increased by acquiring simultaneous nuclei, using multiple receivers. Dual receiver SHARPER has been implemented and tested in this thesis, obtaining both ^{1}H and ^{19}F spectra.

6.1 Future Work

There is a scope for applying SHARPER in a multitude of ways. For example the current versions require signals to be sufficiently isolated to be amenable to selective excitation. This requirement can be eliminated by a number of suitable pre-SHARPER excitation schemes, broadening the application of SHARPER considerably.

SHARPER will continue to be used for reaction monitoring in its basic and slice selective versions. Fast reactions will be monitored using the z-return SHARPER, biphasic mixture interface reactions can be studied using either the double 180 or z-return SHARPER.

There are also potential applications outside of reaction monitoring that will be explored, for example the measurement of coupling constants (SHARPER-J). Exciting opportunities lie in the implementation of SHARPER on benchtop NMR spectrometers, most of which have limited magnetic field homogeneity. In addition, there is a potential to explore SHARPER outside of solution-state NMR spectroscopy.

Bibliography

[1] J. Kind and C. M. Thiele, *Journal of Magnetic Resonance*, 2015, **260**, 109–115.

[2] A. B. Jones, G. C. Lloyd-Jones, and D. Uhrin, *Analytical Chemistry*, 2017, **89**, 10013–10021.

[3] U. Hintermair, *Catalysis Science and Technology*, 2016, **6**, 8406–8417.

[4] *Boronic Acids: Preparation and Applications in Organic Synthesis, Medicine and Materials 1&2*, ed. P. D. G. Hall, Wiley, 2011.

[5] L. S. Liebeskind and J. Srogl, *Organic Letters*, 2002, **4**, 979–981.

[6] J. S. C. Savarin and L. S. Liebeskind, *Organic Letters*, 2001, **3**, 91–93.

[7] B. I. Alo, A. Kandil, P. A. Patil, M. J. Sharp, M. A. Siddiqui, V. Snieckus and P. D. Josephy, *Journal of Organic Chemistry*, 1991, **56**, 3764–3769.

[8] N. Miyaura, *Tetrahedron Letters*, 1979, **36**, 3437–3440.

[9] A. J. J. Lennox and G. C. Lloyd-Jones, *Chemical Society Reviews*, 2014, **43**, 412–443.

[10] Y. L. G. Zhang and J. Liu, *RSC Advances*, 2017, **7**, 34959–34962.

[11] P. A. Cox, M. Reid, A. G. Leach, A. D. Campbell, E. J. King and G. C. Lloyd-Jones, *Journal of the American Chemical Society*, 2017, **139**, 13156–13165.

[12] A. D. C. P. A. Cox, A. G. Leach and G. C. Lloyd-Jones, *Journal of the American Chemical Society*, 2016, **138**, 9145–9157.

[13] C. Adamo, C. Amatore, I. Ciofini, A. Jutand and H.Lakmini, *Journal of the American Chemical Society*, 2006, **128**, 6829–6836.

[14] K. S. Webb and D. Levy, *Tetrahedron Letters*, 1995, **36**, 5117–5118.

[15] P. Hebb, *Journal of Chemical Physics*, 1937, **5**, 338–350.

[16] J. R. Z. I. I. Rabi, J. M. Kellogg, *Physical Review*, 1934, **50**, 396.

[17] J. R. Z. I. I. Rabi, J. M. Kellogg, *Physical Review*, 1934, **49**, 421–2.

[18] Y. O. J. H. Lee and S. Cavagnero, *Journal of Magnetic Resonance*, 2014, **241**, 18–31.

[19] P. J. Hore, *Nuclear Magnetic Resonance*, Oxford University Press, 2015.

[20] H. T. E. Purcell and R. Pound, *Physical Review*, 1946, **69**, 37–38.

[21] F. Bloch, W. Hanssen and M. Packard, *Physical Review*, 1946, **70**, 474 – 189.

[22] T. D. W. Claridge, *High-Resolution NMR techniques in Organic Chemistry*, Elsevier Science Ltd., 1999.

[23] J. Keeler, *Understanding NMR spectroscopy*, Wiley, 2011.

[24] G. H. Sorland, *Dynamic Pulsed-Field-Gradient NMR*, Springer-Verlag Berlin Heidelberg, 2014, vol. 110.

[25] P. Giraudeau and L. Frydman, *Annual Review of Analytical Chemistry*, 2014, **7**, 129–161.

[26] I. E. Ndukwe, A. Shchukina, K. Kazimierczuk, C. Cobas and C. P. Butts, *ChemPhysChem Communications*, 2016, **17**, 2799–2803.

[27] E. Kupce and R. Freeman, *Journal of the American Chemical Society*, 2008, **130**, 10788–10792.

[28] R. R. Ernst and W. A. Anderson, *Review of Scientific Instruments*, 1966, **37**, 93–102.

[29] G. Morris and R. Freeman, *Journal of Magnetic Resonance*, 1978, **29**, 433–462.

[30] K. Zangger and H. Sterk, *Journal of Magnetic Resonance*, 1997, **124**, 486–489.

[31] A. Tal and L. Frydman, *Progress in Nuclear Magnetic Resonance Spectroscopy*, 2010, **57**, 241–292.

[32] H. Geen and R. Freeman, *Journal of Magnetic Resonance*, 1991, **93**, 93–141.

[33] S. W. H. Geen and R. Freeman, *Journal of Magnetic Resonance*, 1989, **85**, 620–627.

[34] M. B. S. A. J. Shaka, J. Keeler and R. Freeman, *Journal of Magnetic Resonance*, 1985, **61**, 175–180.

[35] L. Castañar and T. Parella, *Magnetic Resonance Chemistry*, 2015, **53**, 399–426.

[36] H. N. Meyer and K. Zangger, *Angewandte Chemie*, 2013, **52**, 7143–7146.

[37] K. Zangger, *Progress in Nuclear Magnetic Resonance Spectroscopy*, 2015, **86-87**, 1–20.

[38] Y. C. Avram and L. Frish, *Angewandte Chemie*, 2005, **44**, 520–554.

[39] J. Allen, and K. Damodaran, *Magnetic Resonance in Chemistry*, 2015, **53**, 200–202.

[40] D. S. T. Niklas and M. John, *Chemical Communications*, 2015, **51**, 1275–7.

[41] W. B. G. E. Wagner, P. Sakhaii and K. Zangger, *Chemical Communications*, 2013, **49**, 3155–7.

[42] P. S. Z. Zhang and L. Frydman, *Journal of Chemical Physics*, 2014, **141**, 194201–194210.

[43] A. S. S. M. Mobli and J. C. Hoch, *Journal of Magnetic Resonance*, 2006, **182**, 96–105.

[44] E. Kupce, T. Nishida and R. Freeman, *Progress in Nuclear Magnetic Resonance Spectroscopy*, 2003, **42**, 95–122.

[45] P. Gierth, A. Codina, F. Schumann, H. Kovacs, Helena and E. Kupce, *Magnetic Resonance in Chemistry*, 2015, **53**, 940–944.

[46] I. E. Ndukwe, A. Shchukina, K. Kazimierczuk and C. P. Butts, *Chemical Communications*, 2016, **52**, 12769.

[47] I. E. Ndukwe, A. Shchukina, K. Kazimierczuk, V. Zorin, C. Cobas and C. P. Butts, *ChemPhysChem Communications*, 2017, **18**, 2081–2087.

[48] K. A. M. R. Powers and J. C. Copeland, *Drug Discovery Today*, 2008, **13**, 172–179.

[49] E. K. K. J. Donovan and L. Frydman, *Angewandte Chemie*, 2013, **52**, 4152–4155.

[50] Z. D. Pardo, G. L. Olsen, M. E. Fernández-Valle, L. Frydman, R. Martínez-Álvarez and A. Herrera, *Journal of the American Chemical Society*, 2012, **134**, 2706–2715.

[51] Y. Shrot and L. Frydman, *Journal of Chemical Physics*, 2006, **125**, 204507–12.

[52] K. Zangger, *Progress in Nuclear Magnetic Resonance Spectroscopy*, 2015, **86-87**, 1–20.

[53] W. P. Aue, J. Karhan, R. R. Ernst, *Journal of Chemical Physics*, 1976, **64**, 4226.

[54] J. R. Garbow, D. P. Weitekamp, and A. Pines, *Chemical Physics Letters*, 1982, **93**, 504.

[55] K. Zangger and H. Sterk, *Journal of Magnetic Resonance*, 1997, **124**, 486.

[56] L. Castanar, P. Nolis, A. Virgili, and T. Parella, *Chemistry a European Journal*, 2013, **19**, 17283.

[57] R.W. Adams, L. Byrne, P. Kiraly, M. Foroozandeh, L. Paudel, M. Nilsson, J. Clayden, and G.A. Morris, *Chemical Communications*, 2014, **50**, 2512.

[58] C. Griesinger, O. W. Sorensen, and R. R. Ernst, *Journal of the American Chemical Society*, 1985, **107**, 6394.

[59] O. W. Sorensen, C. Griesinger, and R. R. Ernst, *Journal of the American Chemical Society*, 1985, **107**, 7778.

[60] L. Kaltschnee, A. Kolmer, I. Timári, V. Schmidts, R. W. Adams, M. Nilsson, K. E. Kövér, G. A. Morris and C. M. Thiele, *Chemical Communications*, 2014, **50**, 15702–15705.

[61] E. Kupce, R. Freeman and B. K. John, *Journal of the American Chemical Society*, 2006, **128**, 9606–9607.

[62] E. Kupče, in *NMR with Multiple Receivers*, ed. H. Heise and S. Matthews, Springer Berlin Heidelberg, Berlin, Heidelberg, 2013, ch. Modern NMR Methodology, pp. 71–96.

[63] J. N. Dumez, *Progress in Nuclear Magnetic Resonance Spectroscopy*, 2018, **109**, 101–134.

[64] E. Kupce and R. Freeman, *Magnetic Resonance in Chemistry*, 2007, **45**, 2–4.

[65] M. Billeter, *Journal of Biomolecular NMR*, 2017, **68**, 65–66.

[66] L. R. B. Gouilleux and P. Giraudeau, in *Annual Reports on NMR Spectroscopy*, Elsevier, 2018, pp. 75–144.

[67] E. K. P. Schanda and B. Brutscher, *Journal of Biomolecular NMR*, 2005, **33**, 199–211.

[68] N. M. E. Bendet-Taicher and A. Jerschow, *Concepts in Magnetic Resonance Part B: Magnetic Resonance Engineering*, 2014, **44**, 1–11.

[69] A. L. D. D. A. Foley and M. T. Zell, *Magnetic Resonance in Chemistry*, 2015, **54**, 451–456.

[70] D. A. Foley, E. Bez, A. Codina, K. L. Colson, M. Fey, R. Krull, D. Piroli, M. T. Zell and B. L. Marquez, *Analytical Chemistry*, 2014, **86**, 12008–12013.

[71] A. M. R. Hall, R. Broomfield-Tagg, M. Camilleri, D. R. Carbery and A. Codina, *Chemical Communications*, 2018, **54**, 30–34.

[72] J. F. McGarrity and J. Prodolliet, *The Journal of Organic Chemistry*, 1984, 4465–4470.

[73] M. B. M. Khajeh and G. Morris, *Magnetic Resonance in Chemistry*, 2010, **48**, 516–522.

[74] A. Brächer, S. Hoch, K. Albert, H. J. Kost, B. Werner, E. Von Harbou and H. Hasse, *Journal of Magnetic Resonance*, 2014, **242**, 155–161.

[75] J. P. Y. I. J. Gruntfest and N. L. Johnson, *Journal of Applied Physics*, 1964, **35**, 18–22.

[76] G. Taylor, *Dispersion of Soluble Matter in Solvent Flowing Slowly through a Tube*, 1953.

[77] S. E. Denmark, B. J. Williams, B. M. Eklov, S. M. Pham and G. L. Beutner, *The Journal of Organic Chemistry*, 2010, **75**, 5558–5572.

[78] P. V. Yushmanov and I. Furó, *Journal of Magnetic Resonance*, 2005, **175**, 264–270.

[79] M. C. C. A. Fyfe and S. W. H. Damji, *Accounts of Chemical Research*, 1978, **11**, 277–282.

[80] J. L. D.d B. Green and R. M. Wing, *Applied Spectroscopy*, 1987, **41**, 847–850.

[81] M. D. Christianson, E. H. P. Tan and C. R. Landis, *Journal of the American Chemical Society*, 2010, **132**, 11461–11463.

[82] J. P. J. F. McGarrity and T. Smyth, *Organinc Magnetic Resonance*, 1981, **17**, 59–65.

[83] P. M. C. Ammann and A. Merbach, *Journal of Magnetic Resonance*, 1982, **46**, 319–321.

[84] Y. Mitrev, S. Simova and D. Jeannerat, *Chemical Communications*, 2016, **52**, 7–9.

[85] R. Freeman and H. D. W. Hill, *Journal of Chemical Physics*, 1971, **54**, 301.

[86] M. Gochin, D. P. Weitekemp and A. J. Pines, *Journal of Magnetic Resonance*, 1985, **63**, 431.

[87] K. Ishihara, A. Nagasawa, K. Umemoto, H. Ito and K. Saito, *Inorganic Chemistry*, 1994, **33**, 3811.

[88] Y. Kono, K. Ishihara, A. Nagasawa, K. Umemoto, and K. Saito, *Inorganica Chimica Acta*, 1997, **262**, 91.

Chapter 7

Pulse programs

7.1 Pseudo 2D standard

```
;pseudo2d.aj
;zg2d
;DELTA to allow interscan delay
;avance-version (12/01/11)
;pseudo 2D sequence

#include <Avance.incl>
#include <Delay.incl>

"DELTA=d20-((d1+aq)*(ns+ds))-30m"
"acqt0=-p1*3.1416"

1 ze
2 30m
  DELTA
3 d1
  p1 ph1
  go=2 ph31
  30m mc #0 to 2 F1QF(id0)
exit

ph1=0 2 2 0 1 3 3 1
ph31=0 2 2 0 1 3 3 1

;pl1 : f1 channel - power level for pulse (default)
;p1 : f1 channel -  90 degree high power pulse
;d1 : relaxation delay; 1-5 * T1
;d20: delay between start of different 1D spectra
;ns: 1 * n
;td1: number of experiments
```

7.2 Pseudo2D with trigger

```
;pseudo2dtrig.aj
;pseudo2d.aj
;zg2d
;pseudo 2D sequence
;DELTA to allow interscan delay
;with trigger functionality to be used with InsightXpress

#include <Avance.incl>
#include <Delay.incl>

"DELTA=d20-((d1+aq)*(ns+ds))-30m"
"acqt0=-p1*3.1416"


1 ze
  1m trigpe1
  d21
2 30m
  DELTA
3 d1
  p1 ph1
  go=2 ph31
  30m mc #0 to 2 F1QF(id0)
  lo to 3 times td1
exit

ph1=0 2 2 0 1 3 3 1
ph31=0 2 2 0 1 3 3 1


;pl1 : f1 channel - power level for pulse (default)
;p1 : f1 channel -  90 degree high power pulse
;d1 : relaxation delay; 1-5 * T1
;d20: delay between start of different 1D spectra
;d21: dead time after TTL Pulse
;ns: 1 * n
;td1: number of experiments
```

7.3 Spatially selective frequency shifted excitation

7.3.1 Using a frequency list

```
;fsss-freq.aj
;frequency selective psuedo 2D for kinetics
;using a frequency list

#include <Avance.incl>
#include <Delay.incl>
#include <Grad.incl>

"TAU=d1-5m"
"acqt0=-d16-10u"

define list<frequency> flist=<$FQ1LIST>

1 ze
2 1m flist:f1 st0
3 d1
  50u BLKGRAD
  TAU
  5m UNBLKGRAD
  1m gron0
  (p11:sp1 ph1):f1
  4u
  d16 groff
  go=3 ph31
  d12 flist.inc
  1m mc #0 to 2 F1QF(id0)
exit

ph1=0 2 2 0 1 3 3 1
ph31=0 2 2 0 1 3 3 1


;pl1 : f1 channel - power level for pulse (default)
;p1 : f1 channel -  90 degree shaped pulse
;sp1: f1 channel - shaped pulse
;NS: 1 * n, total number of scans: NS * TD0
;gpz0 : 5%
```

7.3.2 Using a shaped pulse list

```
;fsss-sp.aj
;frequency selective psuedo 2D for kinetics
;using a shaped pulse list

#include <Avance.incl>
#include <Delay.incl>
#include <Grad.incl>

"TAU=d1-5m"
"acqt0=-d16-10u"

define list<shape> SPL_90=<$VDLIST>

1 ze
2 1m
3 d1
  50u BLKGRAD
  TAU
  5m UNBLKGRAD
  1m gron0
  (p11:SPL_90 ph1):f1
  4u
  d16 groff
  go=3 ph31
  d12
  1m mc #0 to 2 F1QF(id0)
exit

ph1=0 2 2 0 1 3 3 1
ph31=0 2 2 0 1 3 3 1


;pl1 : f1 channel - power level for pulse (default)
;p1 : f1 channel -  90 degree shaped pulse
;sp1: f1 channel - shaped pulse
;NS: 1 * n, total number of scans: NS * TD0
;gpz0 : 5%
```

7.3.3 Using SPOFFS - 1D

```
;fsss-SPOFFS.aj
;frequency shifted spatially selective
;using SPOFFS to change frequency

#include <Avance.incl>
#include <Delay.incl>
#include <Grad.incl>

"TAU=d1-5m"
"acqt0=-d16-10u"

1 ze
2 1m
3 d1
  50u BLKGRAD
  TAU
  5m UNBLKGRAD
  1m gron0
  (p11:sp1 ph1):f1
  4u
  d16 groff
  go=3 ph31
  1m mc #0 to 2 0(zd)
exit

ph1=0 2 2 0 1 3 3 1
ph31=0 2 2 0 1 3 3 1


;pl1 : f1 channel - power level for pulse (default)
;p1 : f1 channel -  90 degree shaped pulse
;sp1: f1 channel - shaped pulse
;NS: 1 * n, total number of scans: NS * TD0
;gpz0 : 5-10%
```

7.4 SHARPER

```
;sharper.aj
;1D sequence
;A magnetic field inhomogeniety compensating pure-shift method delivering X-d
;A.B.Jones, G.C.Lloyd-Jones, D. Uhrin, J.Am.Chem.Soc.2017

#include <Avance.incl>
#include <Grad.incl>
#include <Delay.incl>
#include <De.incl>

"p2=p1*2"
"d11=30m"
"p29=300u"
"d62=aq/(l0*2)"
"d63=d62/2"
"d12=20u"
"d11=30m"
"DELTA=d1-d11"

"COUNTER=(trunc((cnst31/100)*l0))+1"
"l31=l0+COUNTER"
"acqt0=-p1*2/PI"
dwellmode explicit

1 ze
2 d11

# ifdef PURGE
  d12 pl10:f1
  p17 ph4
  p17*1.4 ph5
# endif

  4u BLKGRAD
  DELTA
  50u UNBLKGRAD

  d12 pl1:f1
  (p1 ph1):f1

# ifdef SPFGSE
  d12 pl0:f1
  p16:gp2
  d16
  5u
  (p48:sp36 ph6):f1
  5u
  p16:gp2
```

```
   d16
   d12  pl1:f1
# endif

   ACQ_START(ph30,ph31)
   0.1u  START_NEXT_SCAN

# ifdef HALFCHUNK
   0.1u  REC_UNBLK
   0.05u  DWELL_CLK_ON

   d63

   0.05u  DWELL_CLK_OFF
   0.1u  REC_BLK
# endif

# ifdef HARD
4  p29:gp1
   d16  pl1:f1
   (p2  ph2):f1
   p29:gp1
   d16

   0.1u  REC_UNBLK
   0.05u  DWELL_CLK_ON

   d62

   0.05u  DWL_CLK_OFF
   0.1u  REC_BLK

   p29:gp1*-1
   d16  pl1:f1
   (p2  ph3):f1
   p29:gp1*-1
   d16

   0.1u  REC_UNBLK
   0.05u  DWELL_CLK_ON

   d62

   0.05u  DWL_CLK_OFF
   0.1u  REC_BLK

   lo  to  4  times  l31

   d63
```

```
# else

4 p29:gp1
  d16
  5u
  (p48:sp36 ph2):f1
  5u
  p29:gp1
  d16

  0.1u REC_UNBLK
  0.05u DWELL_CLK_ON

  d62

  0.05u DWELL_CLK_OFF
  0.1u REC_BLK

  p29:gp1*-1
  d16
  5u
  (p48:sp36 ph3):f1
  5u
  p29:gp1*-1
  d16

  0.1u REC_UNBLK
  0.05u DWELL_CLK_ON

  d62

  0.05u DWELL_CLK_OFF
  0.1u REC_BLK

  lo to 4 times l31

  d63
# endif
  rcyc=2
  30m mc #0 to 2 F0(zd)
exit

# ifdef SPFGSE

ph1=0 0 0 0 2 2 2 2 1 1 1 1 3 3 3 3
ph2=1 3 1 3 1 3 1 3 0 2 0 2 0 2 0 2
ph3=3 1 3 1 3 1 3 1 2 0 2 0 2 0 2 0
ph4=0
ph5=1
ph6=1 1 0 0 3 3 2 2 2 2 1 1 0 0 3 3
```

```
ph29=0
ph30=0
ph31=0 0 2 2 2 2 0 0 1 1 3 3 3 3 1 1

#else

ph1=0 0 2 2 1 1 3 3
ph2=1 3 1 3 0 2 0 2
ph3=3 1 3 1 2 0 2 0
ph4=0
ph5=1
ph29=0
ph30=0
ph31=0 0 2 2 1 1 3 3

# endif

;pl1 : f1 channel - power level for pulse (default)
;sp36: f1 channel - shaped pulse 180 degree during inital SPFGSE and AQ
;p1 : f1 channel -  high power pulse
;p2 : f1 channel - 180 degree high power pulse
;p29: gradient pulse 3                                    [300 usec]
;p48: f1 channel - 180 degree shaped pulse during inital SPFGSE and AQ
[1-80ms]
;d1 : relaxation delay; 1-5 * T1
;d11: delay for disk I/O                                   [30 msec]
;d16: delay for homospoil/gradient recovery
;d62: length of block between decoupling pulses : = aq/l0 [< 20-25 msec]
;d63: = d62/2
;l0 : number of blocks during acquisition time
;        adjust to get d62 as required
;ns: 2 * n, total number of scans: NS * TD0
;ds: 4

;for z-only gradients:
;gpz1: 40%
;gpz2: 11%
```

7.4.1 Multi-signal SHARPER

```
;sharper_p2d_flp.aj
;sharper.aj
;pseudo2D sequence
;frequency list for pulsing different signals
;A.B.Jones, G.C.Lloyd-Jones, D. Uhrin, J.Am.Chem.Soc.2017

#include <Avance.incl>
#include <Grad.incl>
#include <Delay.incl>
#include <De.incl>

"p2=p1*2"
"d11=30m"
"p29=300u"
"d62=aq/(l0*2)"
"d63=d62/2"
"d12=20u"
"d11=30m"
"DELTA=d1-d11"
"COUNTER=(trunc((cnst31/100)*l0))+1"
"l31=l0+COUNTER"
"acqt0=-p1*2/PI"


define list<frequency> flist=<$FQ1LIST>

dwellmode explicit

1 ze
2 d11
  "flist.idx=l11"

  1m flist:f1
  1m flist(receive):f1

# ifdef PURGE
3 d12 pl10:f1
p17 ph4
p17*1.4 ph5
# endif

4u BLKGRAD
DELTA
50u UNBLKGRAD
d12 pl1:f1
(p1 ph1):f1

# ifdef SPFGSE
```

```
3 d12 pl0:f1
p16:gp2
d16
5u
(p46:sp35 ph6):f1
5u
p16:gp2
d16
d12 pl1:f1
# endif

ACQ_START(ph30,ph31)

# ifdef HALFCHUNK
0.1u REC_UNBLK
0.05u DWL_CLK_ON
d63
0.05u DWL_CLK_OFF
0.1u REC_BLK
# endif

# ifdef HARD
4 p29:gp1
d16 pl1:f1
(p2 ph2):f1
p29:gp1
d16
0.1u REC_UNBLK
0.05u DWL_CLK_ON
d62
0.05u DWL_CLK_OFF
0.1u REC_BLK
p29:gp1*-1
d16 pl1:f1
(p2 ph3):f1
p29:gp1*-1
d16
0.1u REC_UNBLK
0.05u DWL_CLK_ON
d62
0.05u DWL_CLK_OFF
0.1u REC_BLK
lo to 4 times l31
d63

# else
4 p29:gp1
d16
5u
```

```
(p47:sp36 ph2):f1
5u
p29:gp1
d16
0.1u REC_UNBLK
0.05u DWL_CLK_ON
d62
0.05u DWL_CLK_OFF
0.1u REC_BLK
p29:gp1*-1
d16
5u
(p47:sp36 ph3):f1
5u
p29:gp1*-1
d16
0.1u REC_UNBLK
0.05u DWL_CLK_ON
d62
0.05u DWL_CLK_OFF
0.1u REC_BLK
lo to 4 times l31
d63
# endif
rcyc=2
  1m mc #0 to 2
     F1QF(calclc(l11, 1))
exit

# ifdef SPFGSE
ph1=0 0 0 0 2 2 2 2 1 1 1 1 3 3 3 3
ph2=1 3 1 3 1 3 1 3 0 2 0 2 0 2 0 2
ph3=3 1 3 1 3 1 3 1 2 0 2 0 2 0 2 0
ph4=0
ph5=1
ph6=1 1 0 0 3 3 2 2 2 2 1 1 0 0 3 3
ph29=0
ph30=0
ph31=0 0 2 2 2 2 0 0 1 1 3 3 3 3 1 1

#else
ph1=0 0 2 2 1 1 3 3
ph2=1 3 1 3 0 2 0 2
ph3=3 1 3 1 2 0 2 0
ph4=0
ph5=1
ph29=0
ph30=0
ph31=0 0 2 2 1 1 3 3
# endif
```

```
;pl1 : f1 channel - power level for pulse (default)
;sp35: f1 channel - shaped pulse 180 degree inital SPFGSE
;sp36: f1 channel - shaped pulse 180 degree during AQ
;p1 : f1 channel - high power pulse
;p2 : f1 channel - 180 degree high power pulse
;p29: gradient pulse 3 [300 usec]
;p46: f1 channel - 180 degree shaped pulse inital SPFGSE [1-80ms]
;p47: f1 channel - 180 degree shaped pulse during AQ [1-80ms]
;d1 : relaxation delay; 1-5 * T1
;d11: delay for disk I/O [30 msec]
;d16: delay for homospoil/gradient recovery
;d62: length of block between decoupling pulses : = aq/l0 [< 20-25msec]
;d63: = d62/2
;l0 : number of blocks during acquisition time
; adjust to get d62 as required
;ns: 2 * n, total number of scans: NS * TD0
;ds: 4

;for z-only gradients:
;gpz1: 40%
;gpz2: 11%
```

7.4.2 Dual receiver SHARPER

```
;dr_sharper.aj
;dual receiver SHARPER
;A.B.Jones, G.C.Lloyd-Jones, D. Uhrin, J.Am.Chem.Soc.2017

#include <Avance.incl>
#include <Grad.incl>
#include <Delay.incl>
#include <De.incl>

"p2=p1*2"
"p29=300u"
"d11=30m"
"d12=20u"
"d62=aq/(l0*2)"
"d63=d62/2"
"DELTA=d1-d11"
"COUNTER=(trunc((cnst31/100)*l0))+1"
"l31=l0+COUNTER"
"acqt0=-p1*2/PI"

dwellmode explicit

1 ze
2 d11

# ifdef PURGE
  d12 pl10:f1
  p17 ph4
  p17*1.4 ph5
# endif

  4u BLKGRAD
  DELTA
  50u UNBLKGRAD

  d12 pl1:f1
  d12 pl2:f2
  (p1 ph1):f1
  (p3 ph1):f2

# ifdef SPFGSE
  d12 pl0:f1
  d12 pl2:f2
  p16:gp2
  d16
  5u
  (p46:sp35 ph6):f1
  (p46:sp36 ph6):f2
```

```
   5u
   p16:gp2
   d16
   d12  pl1:f1
   d12  pl2:f2
# endif

   ACQ_START1(ph31,ph30)
   ACQ_START2(ph31,ph30)

# ifdef HALFCHUNK
   0.1u REC_UNBLK1
   0.1u REC_UNBLK2
   0.05u DWL_CLK_ON1
   0.05u DWL_CLK_ON2

   d62

   0.05u DWL_CLK_OFF1
   0.05u DWL_CLK_OFF1
   0.1u REC_BLK1
   0.1u REC_BLK2
# endif

# ifdef HARD
4  p29:gp1
   d16  pl1:f1
   (p2  ph2):f1
    d16  pl1:f2
   (p2  ph2):f2
   p29:gp1
   d16

   0.1u REC_UNBLK1
   0.1u REC_UNBLK2
   0.05u DWL_CLK_ON1
   0.05u DWL_CLK_ON2

   d62

   0.05u DWL_CLK_OFF1
   0.05u DWL_CLK_OFF2
   0.1u REC_BLK1
   0.1u REC_BLK2

   p29:gp1*-1
   d16  pl1:f1
   (p2  ph3):f1
    d16  pl1:f2
   (p2  ph3):f2
```

```
  p29:gp1*-1
  d16

  0.1u REC_UNBLK1
  0.1u REC_UNBLK2
  0.05u DWL_CLK_ON1
  0.05u DWL_CLK_ON2

  d62

  0.05u DWL_CLK_OFF1
  0.05u DWL_CLK_OFF2
  0.1u REC_BLK1
  0.1u REC_BLK2

  lo to 4 times l31

  d63

# else

4 p29:gp1
  d16
  5u
  (p47:sp36 ph2):f1
  (p47:sp36 ph2):f2
  5u
  p29:gp1
  d16

  0.1u REC_UNBLK1
  0.1u REC_UNBLK2
  0.05u DWL_CLK_ON1
  0.05u DWL_CLK_ON2

  d62

 0.05u DWL_CLK_OFF1
  0.05u DWL_CLK_OFF2
  0.1u REC_BLK1
  0.1u REC_BLK2

  p29:gp1*-1
  d16
  5u
  (p47:sp36 ph3):f1
  (p47:sp36 ph3):f2
  5u
  p29:gp1*-1
  d16
```

```
   0.1u REC_UNBLK1
   0.1u REC_UNBLK2
   0.05u DWL_CLK_ON1
   0.05u DWL_CLK_ON2

   d62

  0.05u DWL_CLK_OFF1
   0.05u DWL_CLK_OFF2
   0.1u REC_BLK1
   0.1u REC_BLK2

   lo to 4 times l31

   d63

# endif
        (aq1)  (aq2)
        eoscnp2
   30m wr1 #0 if1 #0 ze1
   30m wr2 #1 if2 #1 ze2
   lo to 2 times td1
exit


# ifdef SPFGSE

ph1=0 0 0 0 2 2 2 2 1 1 1 1 3 3 3 3
ph2=1 3 1 3 1 3 1 3 0 2 0 2 0 2 0 2
ph3=3 1 3 1 3 1 3 1 2 0 2 0 2 0 2 0
ph4=0
ph5=1
ph6=1 1 0 0 3 3 2 2 2 2 1 1 0 0 3 3
ph29=0
ph30=0
ph31=0 0 2 2 2 2 0 0 1 1 3 3 3 3 1 1

#else

ph1=0 0 2 2 1 1 3 3
ph2=1 3 1 3 0 2 0 2
ph3=3 1 3 1 2 0 2 0
ph4=0
ph5=1
ph6=1 1 0 0 3 3 2 2 2 2 1 1 0 0 3 3
ph29=0
ph30=0
ph31=0 0 2 2 1 1 3 3
```

```
# endif

;pl1 : f1 channel - power level for pulse (default)
;sp35: f1 channel - shaped pulse 180 degree inital S(D)PFGSE
;sp36: f1 channel - shaped pulse 180 degree during AQ
;p1 : f1 channel -  high power pulse
;p2 : f1 channel - 180 degree high power pulse
;p29: gradient pulse 3                                          [300 usec]
;p46: f1 channel - 180 degree shaped pulse inital S(D)PFGSE [20-80ms]
;p47: f1 channel - 180 degree shaped pulse during AQ       [20-80ms]
;d1 : relaxation delay; 1-5 * T1
;d11: delay for disk I/O                                        [30 msec]
;d16: delay for homospoil/gradient recovery
;d62: length of block between decoupling pulses : = aq/l0 [< 20-25 msec]
;d63: = d62/2
;cnst31: = v9, random variation of +/- v9 %
;l0 : number of blocks during acquisition time
;        adjust to get d62 as required
;ns: 4 * n, total number of scans: NS * TD0
;ds: 4

;for z-only gradients:
;gpz1: 40%
;gpz2: 11%
```

7.4.3 Slice selective SHARPER

Basic SHARPER

```
;sharperpseudo2d_slice.aj.TS3
;slice selective pseudo 2D sequence
;A.B.Jones, G.C.Lloyd-Jones, D. Uhrin, J.Am.Chem.Soc.2017

#include <Avance.incl>
#include <Grad.incl>
#include <Delay.incl>
#include <De.incl>

"p2=p1*2"
"d11=30m"
"p29=300u"
"d62=aq/(l0*2)"
"d63=d62/2"
"d12=20u"
"d11=30m"
"DELTA=d1-d11"

"COUNTER=(trunc((cnst31/100)*l0))+1"
"l31=l0+COUNTER"
"acqt0=-p1*2/PI"

dwellmode explicit

1 ze
2 d11

  4u BLKGRAD
  DELTA
  50u UNBLKGRAD

  d12 pl1:f1
      1m gron0
  (p1 ph1):f1
      4u
      d16 groff

  ACQ_START(ph30,ph31)
  0.1u
# ifdef HALFCHUNK
  0.1u REC_UNBLK
  0.05u DWL_CLK_ON

  d63

  0.05u DWL_CLK_OFF
  0.1u REC_BLK
```

```
# endif

# ifdef HARD
4 p29:gp1
  d16 pl1:f1
      4u gron0
  (p2 ph2):f1
      4u groff
  p29:gp1
  d16

  0.1u REC_UNBLK
  0.05u DWL_CLK_ON

  d62

  0.05u REC_BLK
  0.1u DWL_CLK_OFF

  p29:gp1*-1
  d16 pl1:f1
      4u gron0
  (p2 ph3):f1
      4u groff
  p29:gp1*-1
  d16

  0.1u REC_UNBLK
  0.05u DWL_CLK_ON

  d62

  0.05u REC_BLK
  0.1u DWL_CLK_OFF

  lo to 4 times l31

  d63

# else

4 p29:gp1
  d16
  5u
  d16 gron0
  (p48:sp36 ph2):f1
  5u
  d16 groff
  p29:gp1
  d16
```

```
  0.1u REC_UNBLK
  0.05u DWL_CLK_ON

  d62

  0.05u DWL_CLK_OFF
  0.1u REC_BLK

  p29:gp1*-1
  d16
  5u
  d16 gron0
  (p48:sp36 ph3):f1
  5u
  d16 groff
  p29:gp1*-1
  d16

  0.1u REC_UNBLK
  0.05u DWL_CLK_ON

  d62

  0.05u DWL_CLK_OFF
  0.1u REC_BLK

  lo to 4 times l31

  d63
# endif
  rcyc=2
  30m mc #0 to 2
     F1QF(calclc(l11, 1))
exit

# ifdef SPFGSE

ph1=0 0 0 0 2 2 2 2 1 1 1 1 3 3 3 3
ph2=1 3 1 3 1 3 1 3 0 2 0 2 0 2 0 2
ph3=3 1 3 1 3 1 3 1 2 0 2 0 2 0 2 0
ph4=0
ph5=1
ph6=1 1 0 0 3 3 2 2 2 2 1 1 0 0 3 3
ph29=0
ph30=0
ph31=0 0 2 2 2 2 0 0 1 1 3 3 3 3 1 1

#else
```

```
ph1=0 0 2 2 1 1 3 3
ph2=1 3 1 3 0 2 0 2
ph3=3 1 3 1 2 0 2 0
ph4=0
ph5=1
ph29=0
ph30=0
ph31=0 0 2 2 1 1 3 3

# endif


;pl1 : f1 channel - power level for pulse (default)
;sp36: f1 channel - shaped pulse 180 degree during inital SPFGSE and AQ
;p1 : f1 channel -  high power pulse
;p2 : f1 channel - 180 degree high power pulse
;p29: gradient pulse 3                                    [300 usec]
;p48: f1 channel - 180 degree shaped pulse during inital SPFGSE and AQ
[1-80ms]
;d1 : relaxation delay; 1-5 * T1
;d11: delay for disk I/O                                  [30 msec]
;d16: delay for homospoil/gradient recovery
;d62: length of block between decoupling pulses : = aq/l0 [< 20-25 msec]
;d63: = d62/2
;l0 : number of blocks during acquisition time
;        adjust to get d62 as required
;ns: 2 * n, total number of scans: NS * TD0
;ds: 4

;for z-only gradients:
;gpz1: 40%
;gpz2: 11%
```

Basic sel-SHARPER

```
;sharperpseudo2D_slice4_SPL.aj
;slice selective pseudo 2D sequence with a selective pulse
;A.B.Jones, G.C.Lloyd-Jones, D. Uhrin, J.Am.Chem.Soc.2017

#include <Avance.incl>
#include <Grad.incl>
#include <Delay.incl>
#include <De.incl>

define list<shape> SPL_180=<$VPLIST>

"p2=p1*2"
"p29=300u"
"d11=3m"
"d12=20u"
"d62=aq/(l0*2)"
"d63=d62/2"
"DELTA=d1-d11"
"l11=0"
"TAU=d16+p1*2/PI-de"
"acqt0=0"
baseopt_echo

dwellmode explicit

1 ze
2 d11

  4u BLKGRAD
  DELTA
  50u UNBLKGRAD

  d12 pl1:f1
  (p1 ph4):f1
  d12 pl0:f1

  "SPL_180.idx=l11"

  p16:gp2
  d16 pl0:f1
  5u gron0
  (p46:SPL_180 ph6):f1
  5u
  d16 groff
  p16:gp2
  TAU

  ACQ_START(ph30,ph31)
```

```
# ifdef HALFCHUNK
  0.1u REC_UNBLK
  0.05u DWL_CLK_ON

  d63

  0.05u DWL_CLK_OFF
  0.1u REC_BLK
# endif

4 p29:gp1
  d16
  d16
  5u gron0
  (p47:SPL_180 ph2):f1
  5u
  d16 groff
  p29:gp1
  d16

  0.1u REC_UNBLK
  0.05u DWL_CLK_ON

  d62

  0.05u DWL_CLK_OFF
  0.1u REC_BLK

  p29:gp1*-1
  d16
  d16
  5u gron0
  (p47:SPL_180 ph3):f1
  5u
  d16 groff
  p29:gp1*-1
  d16

  0.1u REC_UNBLK
  0.05u DWL_CLK_ON

  d62

  0.05u DWL_CLK_OFF
  0.1u REC_BLK

  lo to 4 times l0

  d63
```

```
  rcyc=2
  3m mc #0 to 2
     F1QF(calclc(l11, 1))
exit

ph1=0 0 0 0 2 2 2 2 1 1 1 1 3 3 3 3
ph2=3 1 3 1 3 1 3 0 2 0 2 0 2 0 2
ph3=1 3 1 3 1 3 1 2 0 2 0 2 0 2 0
ph4=0
ph5=1
ph6=1 1 0 0 3 3 2 2 2 2 1 1 0 0 3 3
ph7=2
ph29=0
ph30=0
ph31=0 0 2 2 2 2 0 0 1 1 3 3 3 3 1 1

;pl1 : f1 channel - power level for pulse (default)
;sp35: f1 channel - shaped pulse 180 degree inital S(D)PFGSE
;sp36: f1 channel - shaped pulse 180 degree during AQ
;p1 : f1 channel -  high power pulse
;p2 : f1 channel - 180 degree high power pulse
;p29: gradient pulse 3                                          [300 usec]
;p46: f1 channel - 180 degree shaped pulse inital S(D)PFGSE [20-80ms]
;p47: f1 channel - 180 degree shaped pulse during AQ       [20-80ms]
;d1 : relaxation delay; 1-5 * T1
;d11: delay for disk I/O                                        [30 msec]
;d16: delay for homospoil/gradient recovery
;d62: length of block between decoupling pulses : = aq/l0 [< 20-25 msec]
;d63: = d62/2
;l0 : number of blocks during acquisition time
;        adjust to get d62 as required
;ns: 4 * n, total number of scans: NS * TD0
;ds: 4

;for z-only gradients:
;gpz1: 40%
;gpz2: 11%
```

Double 180° SHARPER

```
;sharperpseudo2D_d180.aj
;slice selective pseudo 2D sequence with two 180 selective pulses
;A.B.Jones, G.C.Lloyd-Jones, D. Uhrin, J.Am.Chem.Soc.2017

#include <Avance.incl>
#include <Grad.incl>
#include <Delay.incl>
#include <De.incl>

define list<shape> SPL_180=<$VPLIST>

"p2=p1*2"
"p29=300u"
"d11=3m"
"d12=20u"
"d62=aq/(l0*2)"
"d63=d62/2"
"DELTA=d1-d11"
"l11=0"
"TAU=d16+p1*2/PI-de"
"acqt0=0"
baseopt_echo

dwellmode explicit

1 ze
2 3m

  4u BLKGRAD
  DELTA
  50u UNBLKGRAD

   d12 pl1:f1
  (p1 ph4):f1
  d12 pl0:f1

  p16:gp2
  5u
  (p45:sp34 ph5):f1
  5u
  p16:gp2


  "SPL_180.idx=l11"


  d16 pl1:f1
  5u gron0
```

```
  (p47:SPL_180 ph2):f1
  5u
  d16 groff pl0:f1

  TAU

  ACQ_START(ph30,ph31)

  0.1u REC_UNBLK
  0.05u DWL_CLK_ON
  d63
  0.05u DWL_CLK_OFF
  0.1u REC_BLK

4 p29:gp1
  d16
  5u gron0
  (p47:SPL_180 ph2):f1
  5u
  d16 groff
  p29:gp1

  0.1u REC_UNBLK
  0.05u DWL_CLK_ON

  d62

  0.05u DWL_CLK_OFF
  0.1u REC_BLK

  p29:gp1*-1
  d16
  5u gron0
  (p47:sp32 ph3):f1
  5u
  d16 groff
  p29:gp1*-1


  0.1u REC_UNBLK
  0.05u DWL_CLK_ON

  d62

  0.05u DWL_CLK_OFF
  0.1u REC_BLK

  lo to 4 times l0

  d63
```

```
  rcyc=2
  3m mc #0 to 2
     F1QF(calclc(l11, 1))
exit


ph1=0 0 0 0 2 2 2 2 1 1 1 1 3 3 3 3
ph2=3 1 3 1 3 1 3 0 2 0 2 0 2 0 2
ph3=1 3 1 3 1 3 1 2 0 2 0 2 0 2 0
ph4=0
ph5=1
ph6=1 1 0 0 3 3 2 2 2 2 1 1 0 0 3 3
ph7=2
ph29=0
ph30=0
ph31=0 0 2 2 2 2 0 0 1 1 3 3 3 3 1 1


;pl1 : f1 channel - power level for pulse (default)
;sp35: f1 channel - shaped pulse 180 degree inital S(D)PFGSE
;sp36: f1 channel - shaped pulse 180 degree during AQ
;p1 : f1 channel -  high power pulse
;p2 : f1 channel - 180 degree high power pulse
;p29: gradient pulse 3                                          [300 usec]
;p46: f1 channel - 180 degree shaped pulse inital S(D)PFGSE [20-80ms]
;p47: f1 channel - 180 degree shaped pulse during AQ       [20-80ms]
;d1 : relaxation delay; 1-5 * T1
;d11: delay for disk I/O                                        [30 msec]
;d16: delay for homospoil/gradient recovery
;d62: length of block between decoupling pulses : = aq/l0 [< 20-25 msec]
;d63: = d62/2
;l0 : number of blocks during acquisition time
;        adjust to get d62 as required
;ns: 4 * n, total number of scans: NS * TD0
;ds: 4

;for z-only gradients:
;gpz0: 2%
;gpz1: 40%
;gpz2: 11%
```

Z return SHARPER

```
;sharperpseudo2D_zreturn_SPL.aj
;Slice selective SHARPER
;returns spins to z-axis before slice selective refocusing
;A.B.Jones, G.C.Lloyd-Jones, D. Uhrin, J.Am.Chem.Soc.2017


#include <Avance.incl>
#include <Grad.incl>
#include <Delay.incl>
#include <De.incl>

define list<shape> SPL_180=<$VPLIST>
define list<shape> SPL_90=<$VDLIST>

"p2=p1*2"
"p29=300u"
"d11=3m"
"d12=20u"
"d62=aq/(l0*2)"
"d63=d62/2"
"DELTA=d1-d11"
"l11=0"
"TAU=d16+p1*2/PI-de"
"acqt0=-d16-de"

dwellmode explicit

1 ze
2 d11

  4u BLKGRAD
  DELTA
  50u UNBLKGRAD

  d12 pl1:f1
  (p1 ph4):f1

  d12 pl0:f1
  p16:gp2
  d16
  5u
  (p45:sp34 ph5):f1
  5u
  p16:gp2
  d16 pl1:f1
  d12
  (p1 ph7):f1
```

```
  d12
  "SPL_180.idx=l11"
  "SPL_90.idx=l11"

  p16:gp3
  d16 pl0:f1

  5u gron0
  (p44:SPL_90 ph1):f1
  d16 groff

  ACQ_START(ph30,ph31)

# ifdef HALFCHUNK
  0.1u REC_UNBLK
  0.05u DWL_CLK_ON

  d63

  0.05u DWL_CLK_OFF
  0.1u REC_BLK
# endif

4 p29:gp1
  d16
  d16
  5u gron0
  (p47:SPL_180 ph2):f1
  5u
  d16 groff
  p29:gp1
  d16

  0.1u REC_UNBLK
  0.05u DWL_CLK_ON

  d62

  0.05u DWL_CLK_OFF
  0.1u REC_BLK

  p29:gp1*-1
  d16
  d16
  5u gron0
  (p47:SPL_180 ph3):f1
  5u
  d16 groff
  p29:gp1*-1
```

```
  d16

  0.1u REC_UNBLK
  0.05u DWL_CLK_ON

  d62

  0.05u DWL_CLK_OFF
  0.1u REC_BLK

  lo to 4 times l0

  d63
  rcyc=2
  3m mc #0 to 2
     F1QF(calclc(l11, 1))
exit

ph1=0 0 2 2 1 1 3 3
ph2=3 1 3 0 2 0 2
ph3=1 3 1 2 0 2 0
ph4=0
ph5=1
ph7=2
ph29=0
ph30=0
ph31=0 0 2 2 1 1 3 3

;pl1 : f1 channel - power level for pulse (default)
;sp35: f1 channel - shaped pulse 180 degree inital S(D)PFGSE
;sp36: f1 channel - shaped pulse 180 degree during AQ
;p1 : f1 channel -  high power pulse
;p2 : f1 channel - 180 degree high power pulse
;p29: gradient pulse 3                                    [300 usec]
;p46: f1 channel - 180 degree shaped pulse inital S(D)PFGSE [20-80ms]
;p47: f1 channel - 180 degree shaped pulse during AQ      [20-80ms]
;d1 : relaxation delay; 1-5 * T1
;d11: delay for disk I/O                                  [30 msec]
;d16: delay for homospoil/gradient recovery
;d62: length of block between decoupling pulses : = aq/l0 [< 20-25 msec]
;d63: = d62/2
;l0 : number of blocks during acquisition time
;        adjust to get d62 as required
;ns: 4 * n, total number of scans: NS * TD0
;ds: 4


;for z-only gradients:
;gpz0: 2%
;gpz1: 40%
```

; gpz2 : 11%
; gpz3 : 31%